

VISCOELASTIC PHENOMENA IN ROLL-TO-ROLL
MANUFACTURING

TWO CASE STUDIES OF INDUSTRIAL RELEVANCE

By

MANOGNA JAMBHAPURAM

Bachelor of Technology in Mechanical Engineering
Jawaherlal Nehru Technological University
Andhra Pradesh, India
2014

Master of Design in Mechanical Systems
Indian Institute of Information Technology
Tamil Nadu, India
2017

Submitted to the Faculty of the
Graduate College of the
Oklahoma State University
in partial fulfillment of
the requirements for
the Degree of
DOCTOR OF PHILOSOPHY
December, 2020

VISCOELASTIC PHENOMENA IN ROLL-TO-ROLL
MANUFACTURING
TWO CASE STUDIES OF INDUSTRIAL RELEVANCE

Dissertation Approved:

Dr. Azoug, Aurelie

Dissertation Advisor

Dr. Good, J. Keith

Dr. Wang, Shuodao

Dr. Ley, M. Tyler

ACKNOWLEDGMENTS

First of all, I express sincere thanks and appreciation to my mentors Dr. Good and Dr. Azoug. Their guidance and assistance have always inspired me and led me to the accomplishments presented here. They granted me a comfortable amount of freedom and their measured criticism has always been invaluable in my research endeavors.

Secondly, I would like to thank my dissertation committee for their suggestions and help. I would like to thank each committee member for their time, effort, and patience required to conduct each of the three exams required for this degree.

Thirdly, I would like to extend my special appreciation to Mr. Ron Markum for his help during experimental studies. I also thank my team-mates and colleagues from WHRC for their friendship and for all the great discussions we have had. The support from sponsors of WHRC for their funding and help is greatly appreciated.

Finally, I would express my profound gratitude to my family and friends who supported me throughout my years of study. I am also deeply grateful to my fiancé, Dheeraj, for his support in pursuing my dreams.

Acknowledgments reflect the views of the author and are not endorsed by committee members or Oklahoma State University.

Name: MANOGNA JAMBHAPURAM

Date of Degree: DECEMBER, 2020

Title of Study: VISCOELASTIC PHENOMENA IN ROLL-TO-ROLL MANUFACTURING - *TWO CASE STUDIES OF INDUSTRIAL RELEVANCE*

Major Field: MECHANICAL AND AEROSPACE ENGINEERING

Abstract: In the current manufacturing industry, Roll-to-Roll (R2R) manufacturing is in high demand because of its high productivity and low cost. Many materials used for R2R manufacturing are considered viscoelastic on some time scale and they evolve with time under pressure. It is important to study their viscoelastic phenomena to understand the behavior during and after it undergoes R2R processing. In the present research, we focus on lamination and nanoimprint lithography processes. In the lamination process, two or more webs pass through the roller set where they are laminated. Once the laminated webs are set free from the laminating machine, curl can be witnessed due to the mismatch in the induced web strain. The viscoelastic nature of the laminate adhesive affects the shear deformation during and after lamination which results in mismatched strain conditions. These curls are considered defects and have always been a problem of interest. The goal is to study the parameters that affect the curl of the laminated web by developing lamination models. The optimal lamination operating parameters that would produce a curl-free laminated web for the given web and laminate adhesive are estimated.

In nanoimprint lithography, once the webs are imprinted with the nanopatterns, they are stored in the form of wound rolls until they are needed in a subsequent R2R process. Due to the viscoelastic nature of the UV curable resin, the imprints experience creep when subjected to the wound roll pressure, which affects the performance of the product. The goal is to study the effect of wound roll pressures on the nanoimprinted web. With obtained viscoelastic material properties for the resin, the deformation of the nanopatterns are calculated through the time when subjected to wound roll pressures (computed using a winding model). This will help in establishing how the imprinted materials should be wound and how long they can be subjected to pressure in the wound roll before they should be unwound to limit the deformation of the nano-imprinted features.

TABLE OF CONTENTS

Chapter	Page
I. GENERAL INTRODUCTION	1
1.1 Web handling definitions and case studies	1
1.1. 1 Case Study-1: Lamination process	2
1.1. 2 Case study-2: Nanoimprint lithography process	3
1.2 Motivation	5
<u>CASE STUDY 1: DEVELOPMENT OF LAMINATION MODELS IN R2R MANUFACTURING</u>	7
II. INTRODUCTION TO LAMINATION PROCESS	8
III. LITERATURE REVIEW	12
3.1 Review on nip mechanics in Winding and Calendering models	12
3.2 Review on nip contact analysis	21
3.3 Review of MD curl due to winding single webs	28
3.4 Review on lamination of the webs	30
IV. RESEARCH OBJECTIVE FOR R2R LAMINATION	38
V. NUMERICAL ANALYSIS OF LAMINATION MODELS	40
5.1 Development of lamination model	40
5.1. 1 Model Setup	40
5.1. 2 Boundary Conditions, Loadings and Interactions	44
5.1. 3 Mesh and Elements	47

Chapter	Page
5.1. 4	49
5.2	50
5.2. 1	50
5.2. 2	52
5.2. 3	54
VI. MODEL OF LAMINATION WITH ADHESIVES	57
6.1	57
6.2	65
6.3	66
6.3. 1	68
6.3. 1.1	69
6.3. 1.2	71
6.3. 2	72
6.4	78
VII. FINDINGS AND CONCLUSIONS FOR THE LAMINATION MODEL RESEARCH	81
CASE STUDY 2: WINDING OF ULTRAVIOLET NANOIMPRESSION LITHOGRAPHY'S NANO-IMPRINTED WEBS	84
VIII. INTRODUCTION TO UV-NIL PROCESS	85
IX. LITERATURE REVIEW	89
9.1	89

Chapter	Page
9.2 Review on Winding Models	98
9.2. 1 Elastic Winding Models	98
9.2. 2 Visco-elastic Winding Models	105
X. RESEARCH OBJECTIVE FOR ROLL-TO-ROLL UV-NIL . . .	110
XI. CHARACTERIZATION OF VISCOELASTIC ULTRAVIOLET CURABLE RESIN	112
11.1 Viscoelastic rheological model	112
11.2 Dark curing	113
11.3 Characterization in stress relaxation	114
11.4 Dynamic mechanical analysis characterization considering dark curing period	119
XII. EQUIVALENT MATERIAL PROPERTIES FOR THE IMPRINTED WEB	124
12.1 The pressure-dependent radial modulus	124
12.2 Analytical determination of the equivalent radial modulus for nano-imprinted web	125
12.3 Numerical determination of the equivalent radial modulus for a nano-imprinted web	127
12.4 Equivalent radial viscoelastic functions for a nano imprinted web . .	130
XIII. ESTIMATING THE PRESSURE AND DEFORMATION OF THE NANOIMPRINT IN THE WOUND ROLL	134
13.1 Radial pressure in the wound roll	134
13.2 Deformation of the nanoimprints in the wound roll	135
XIV. VALIDATION TEST	137
14.1 Validation test at the nanometer scale	137
14.2 Validation test at the millimeter scale	138

Chapter	Page
14.2. 1 Theoretical equivalence of conversion degrees	138
14.2. 2 Validation test setup	145
14.2. 3 Comparison with numerical model	146
XV.FINDINGS AND CONCLUSIONS FOR UV-NIL NANOIMPRINTS SUBJECTED TO WINDING	150
XVI.FUTURE WORK	153
16.1 Validation of the lamination model	153
16.2 Characterization of the viscoelastic UV-15 resin considering dark curing period	154
16.3 Validation of the wound nanoimprinted web model at the nanometer scale	154
REFERENCES	166
APPENDICES	167

LIST OF TABLES

Table		Page
5.1	Geometry of the model	41
5.2	Mesh Element Size	48
5.3	T_1 and T_2 values for Model-I results	51
5.4	MD Curl radius for different T_{diff}	53
5.5	MD Curl radius for different Nip loads	54
6.1	Prony Series for the Model	64
6.2	Material properties of Adhesive as input for Abaqus	65
6.3	Loading conditions for Model-IV	66
6.4	MD Curl radius for different τ_1 values	69
6.5	Loading conditions	72
6.6	MD Curl Radius for different angular velocities	72
6.7	Torque levels at which MD curl vanished for different web tension inputs	75
6.8	Loading conditions	79
11.1	Coefficients of the Prony Series representing the relaxation modulus	119
12.1	Material Properties	129
12.2	Radial Modulus for different Cases	129
12.3	Prony Series representing the creep viscoelastic behavior	132
13.1	Input Parameters for the winding model	135

Table		Page
14.1	Geometry and Curing condition of the tests	139
14.2	Dark cure time for the creep test (case-C) specimen	144
14.3	Cases considered for performing creep test for validation	148

LIST OF FIGURES

Figure		Page
1.1	Example of Roll-to-Roll Manufacturing Process	2
1.2	Lamination Process	3
1.3	UV-NIL Process	4
2.1	A Laminator	9
3.1	Winding model (a) Center winding; (b) Surface winding	13
3.2	The Finite Element Model for a stationary web with moving Hertzian parabolic pressure [1]	15
3.3	(a) Surface winding; (b) Center winding [2]	17
3.4	Geometry of the problem [3]	19
3.5	Schematic of 3-D nip mechanics problem [4]	20
3.6	System to be studied [5]	21
3.7	Nip configuration (a) Thomas and Hoersch’s work; (b) Hannah’s work [6]	23
3.8	(a) design (or input); (b) response (or output) variables of roller configuration [7]	25
3.9	Roller configuration considered for analysis [8, 9]	26
3.10	(a) actual geometry with two elastomeric transport rollers; (b) Symmetry condition used for analysis [10]	27
3.11	Basic Strip Configurations [11]	28

Figure		Page
3.12	(a) Speed regulated hard roll drive; (b) Load share torque soft roll drive [12]	31
3.13	Basic Strip Configurations [13]	32
3.14	Lamination of two webs [13]	33
3.15	Layer thickness nomenclature [14]	35
3.16	Kappa gauge [15]	36
3.17	Curl gauge [16]	36
5.1	Model setup in Abaqus (a) Model-I, (b) Model-II, (c) Model-III .	41
5.2	Comparison of Explicit and implicit Schemes	43
5.3	Model with loading and boundary conditions	44
5.4	Amplitude graph for loads and boundary conditions for every step	46
5.5	Coulomb's Friction Model	47
5.6	Mesh for the lamination model (a) For rubber covered roller; (b) For the webs	48
5.7	Pictorial representation of the laminated web	49
5.8	Sign for MD curl radius, (a) Positive Curl; (b) Negative Curl . . .	50
5.9	MD Curl radius for Model-I	51
5.10	MD Curl radius for case(a) $T_{diff}=2.07$ MPa; (b) $T_{diff}=-2.07$ MPa	52
5.11	Tension applied on webs for Model-II	53
5.12	MD Curl Radius for Case-2	54
5.13	MD Curl Radius for Case-3	54
5.14	Defining wrap angle, θ for model-III	55
5.15	Cases with two different web tensions, For (a) $T_{diff} = 3.45$ MPa; (b) $T_{diff} = 0.69$ MPa	55
5.16	Cases with two different web tensions, T_{diff}	56

Figure		Page
6.1	(a) Specimen subjected to loading; (b) Applied strain Vs. time . . .	58
6.2	Effect of Stress relaxation test i.e. resulting stress Vs. time	58
6.3	Stress Relaxation Test on RSA-G2 machine	59
6.4	Geometry of the Double lap Adhesive joint	60
6.5	Force balance for the specimen used in Stress relaxation test . . .	60
6.6	Relaxation Modulus as a function of time	61
6.7	Relaxation modulus as a function of time	62
6.8	Generalized Maxwell Model	62
6.9	Curve fitting for Relaxation Shear modulus, $G(t)$	64
6.10	Model setup in Abaqus for Model-IV	66
6.11	MD curl in the laminated web for (a) Model-II; (b) Model-IV . . .	67
6.12	Shear Strain in the Adhesive Layer at Nip Contact Zone	67
6.13	Contact Status at Nip Contact Zone for (a) Bottom Web; (b) Top Web	68
6.14	Final MD curl Radius of laminated web for (a) Case-i; (b) Case-ii; (c) Case-iii	69
6.15	Shear strain of the adhesive layer for (a) Case-i;(b) Case-iii	70
6.16	MD curl in the laminated web for (a)case-I; (b)case-II	71
6.17	Pictorial representation representing notations for equilibrium equa- tion	73
6.18	Final MD curl Radius of laminated web for different Torque inputs	73
6.19	MD Curl Radius Vs. Torque input	74
6.20	MD Curl Radius vs. Torque input for (a) Case-1; (b) Case-3	75
6.21	Shear Strain of Adhesive layer in Nip contact zone for $R_\tau=3$ lb.-in	76
6.22	Shear Strain of Adhesive layer in Nip contact zone for different R_τ levels	77

Figure		Page
6.23	Contact status of the bottom web for different R_τ levels	77
6.24	Contact status of the top web for different R_τ levels	78
6.25	Model setup in Abaqus for model-V	78
6.26	Shear Strain of Adhesive layer in Nip Contact Zone	79
6.27	Curl free laminated web for (a) Wrap angle 90^0 ; (b) wrap angle 45^0	80
7.1	(a) Laminator operating chart, (b) Laminator operating chart for the developed model	83
8.1	Schematic diagram of Thermal-NIL and UV-NIL Process	85
8.2	Schematic diagram of R2R UV-NIL Process	87
9.1	Scanning electron microscope image of dot patterns imprinted on PMMA [17]	89
9.2	Schematic of thermal nanoimprint lithography process [17]	90
9.3	Schematic of UV nanoimprint lithography process [18]	91
9.4	Roller nanoimprint lithography (a) cycle mold method; (b) flat mold method [19]	92
9.5	Schematic diagram of continuous UV-NIL process (a) for a rigid substrate; (b) for a flexible substrate [20]	94
9.6	Replication results (a) SEM and FIB images; (b) SEM and AFM images [20]	95
9.7	(a)Schematic of R2RNIL Process; (b)The coating unit; (c)Imprint unit [21]	96
9.8	(a)Photograph of imprinted PET web with thermal R2RNIL pro- cess; (b,e)SEM micrograph of the replicated grating structure; (c,d)Photograph of imprinted PET web with UV R2RNIL process [21]	96

Figure	Page
9.9	(a) Schematic of nanopattern fabrication producing line for R2R UV NIL (b) Schematic of R2R UV NIL and nip mechanics in nip contact zone [22] 97
9.10	Schematic Diagram of four parameter model [23] 105
11.1	Representation of Generalized Maxwell model 112
11.2	(a) Specimen subjected to loading; (b) Cause of Stress relaxation test i.e. applied strain Vs. time 115
11.3	Effect of Stress relaxation test i.e. resulting stress Vs. time . . . 116
11.4	(a) UV light setup with mold on which UV light is exposed; (b) Geometry of the mold; (c) The specimen 117
11.5	(a) Setup of stress relaxation test on Instron tensile machine; (b) Close view of specimen that is subjected to testing 117
11.6	Relaxation modulus, $E(t)$ as a function of time 118
11.7	Relaxation modulus and Prony series fitted on the data 118
11.8	Evolution of the norm of the complex modulus and loss factor of the resin during dark curing with frequency as X-axis at temperature (a) 23°C (b) 30°C (c) 40°C 121
11.9	(a) Evolution of the norm of the complex modulus of the resin during dark curing for all the temperatures (a) 23°C (b) Master curve 122
12.1	Pictorial representation of a nano-imprinted web 126
12.2	Imprint geometry cases 1,2,3, and 4 128
12.3	Nano-imprinted web model and boundary conditions. 128
12.4	Stress-strain curve of the imprinted web in response to a uni-axial pressure. 130

Figure	Page
12.5	Dimensions and boundary conditions of the numerical creep model. 131
12.6	Creep compliance of the imprinted web. 132
13.1	Radial stress profile according to time 135
13.2	Pressure-induced displacement of the nano-imprints 136
14.1	Conversion versus thickness for two UV intensities (17 mW/cm^2 , 50 mW/cm^2) and exposure time 100 sec, 200 sec and 300 sec. [24] 140
14.2	μ and β parameters versus (a) intensity; (b) exposure time 141
14.3	Conversion versus thickness for intensity 97 and 185 mW/cm^2 . . 141
14.4	Stress versus strain for tensile tests at different dark cure times t_{DC} using (a) Rubber mold; (b) Teflon mold 142
14.5	Dark curing conversion versus time 143
14.6	(a) UV light setup with mold on which UV light is exposed; (b) Geometry of the mold; (c) The specimen 144
14.7	Setup of creep test on Instron tensile machine 145
14.8	Strain of the resin through time for specimens with different dark cure times, t_{DC} 146
14.9	Geometry and boundary conditions of the numerical creep model 147
14.10	Comparison of creep test with computational model with strain of the resin through time 148
A.1	Circle with three points 167

NOMENCLATURE

VARIABLES	UNITS	DESCRIPTION
N	N/mm	Nip Load
E	MPa	Young's Modulus
E_0	MPa	Equilibrium Modulus
$E(t)$	MPa	Relaxation Modulus
$J(t)$	1/MPa	Creep compliance
E'	MPa	Storage Modulus
E''	MPa	Loss Modulus
E_r	MPa	Radial Modulus
E_θ	MPa	Circumferential Modulus
P	MPa	Pressure
K_1, K_2	MPa, –	Function Coefficients
$G(t)$	MPa	Shear Modulus
K	MPa	Bulk Modulus
A	mm ²	Cross sectional area
R	mm	Radius of roller
b_I	mm	Width of nano-imprint's bottom side
b_h	mm	Width of nano-imprint's top side
b_v	mm	distance between two nano-imprints
h	mm	Thickness of nano-imprint
h_0	mm	Thickness of nano-imprint base

h_1	mm	Thickness of web
K_n	N/mm	Spring stiffness of nanoimprint
K_b	N/mm	Spring stiffness of nanoimprint base
K_w	N/mm	Spring stiffness of web
U	mm	Displacement of nanoimprint
T_1, T_2	MPa	Tension applied on the right side of web
T_3, T_4	MPa	Tension applied on the left side of web
T_{diff}	MPa	Tension difference between top and bottom web
R_τ	N – mm	Torque input to rubber covered roller
I	mm ⁴	Moment of inertia
M	N – mm	Bending moment

GREEK SYMBOLS	UNITS	DESCRIPTION
θ	degrees	Wrap angle
ν	–	Poisson's ratio
ρ	N/mm ³	Poisson's ratio
ω	rad/sec	Angular velocity
τ_{crit}	MPa	Critical shear stress
τ_k	sec	Relaxation time of the adhesive
τ_i	sec	Relaxation time of UV-15 Resin
μ	–	Coefficient of friction
ρ	mm	Radius of curvature
σ	MPa	Tensile stress on the specimen
$\sigma(t)$	MPa	Resulting stress as a function of time, t
ϵ	–	Membrane strain
ϵ_0	–	Constant strain applied for stress relaxation test

CHAPTER I

GENERAL INTRODUCTION

1.1 Web handling definitions and case studies

A web is a thin material that is manufactured and processed in a continuous, flexible strip form. Webs have very small thickness and width (lateral direction) compared to their length (longitudinal direction). Web materials cover a broad spectrum, from metals to paper to non-woven. Web processing, which is also known as Roll-to-Roll (R2R) processing, is commonplace in the current manufacturing industries because it allows the manufacturing of a rich variety of products from continuous strips of material in mass quantity (i.e. continuous production). The current research is focused on R2R manufacturing, where webs are processed through sets of rollers (Figure 1.1) to convert them to the required product, which can either be the final product or can be used for subsequent R2R processing. Web/R2R processes constitute a large sector of all manufacturing conducted today and include calendaring, casting, coating, cooling, dyeing, embossing, folding, heating, laminating, moisturizing, printing, slitting, etc. Products that involve web/R2R processing can be found in the fields of aircrafts, automobiles, bags, books, boxes, clothing, floor covering, furniture, newspapers, photography, plastic sheeting, electronics, etc.

Web handling knowledge is required to control the processing of webs with minimal defects for high precision applications. Web handling involves the physical me-

chanics related to the running and control of webs through processes and machines without incurring defects and losses.

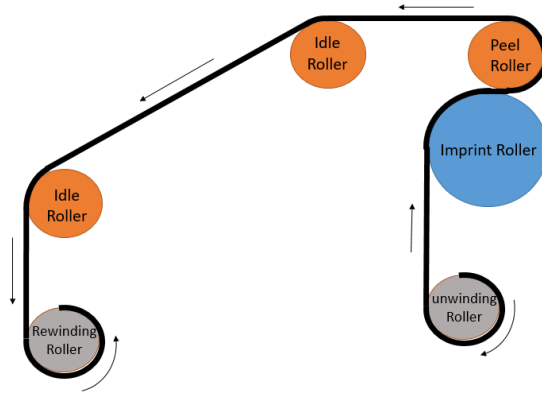


Figure 1.1: Example of Roll-to-Roll Manufacturing Process

The current research focuses on two specific R2R manufacturing processes: lamination and nanoimprint lithography.

1.1. 1 Case Study-1: Lamination process

In the lamination process, two or more webs are combined in the nip contact zone of the rollers (Figure 1.2). The lamination process can be used for different purposes including [25]:

- **Mechanical:** The web layers are combined to improve their mechanical properties; for example, laminated webs often exhibit increased tensile strength.
- **Chemical:** Chemical properties of a web are improved through lamination; for example, laminated webs have reduced vapor, gas, or moisture transmission rates.
- **Decorative:** The layers are combined to improve the appearance of a web; for example, adding a printed film to the web.

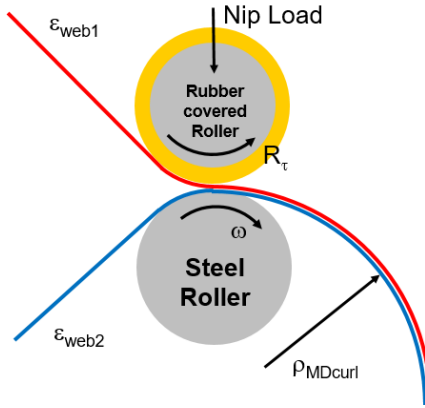


Figure 1.2: Lamination Process

It is important to control the parameters that influence the lamination process to ensure the high quality of the final laminated product. There are certain defects commonly occurring in lamination such as bubbles, wrinkling, orange peeling, waving, and curl. When two webs are laminated at different strain levels, a defect known as curl is witnessed in the laminated web (Figure 1.2). In the first part of the presented research work, we focus on controlling the occurrence of curl in the laminated web. This will help in optimizing the set of parameters that produces curl free laminated webs, replacing the trial and error procedure followed by many operators working at laminating machines in industry.

1.1. 2 Case study-2: Nanoimprint lithography process

Imprinting of different nano-sized patterns on a web surface is known as nanoimprint lithography (NIL) and can be used to fabricate electrical, optical, photonic, and biological devices.

Scaling NIL from discrete stamping to R2R manufacturing can overcome challenges such as slow processing and increase productivity. In this process, webs are precisely imprinted with a nano pattern using UV curable resin (Figure 1.3). The

period, height, and duty cycle of the nano-features are dictated by the application requirements. After imprinting, the resin is cured with UV rays to form a solid polymer. Anything deforming these features either permanently or temporarily would affect the performance of the product. The nanoimprinted features are made of a soft polymer and are viscoelastic on a time scale that needs to be determined.

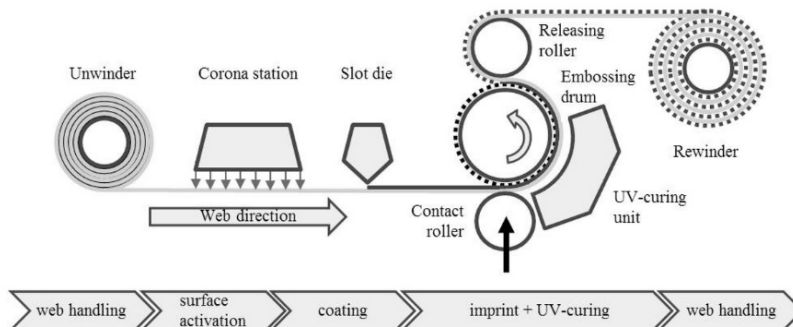


Figure 1.3: UV-NIL Process

Once the webs are imprinted in R2R UV-NIL process, they are stored in wound roll form. The process of converting flat webs to a wound roll form around a core is known as winding. During the winding process, some defects, such as roll telescoping, roll blocking, buckling, and bulk loss, are inevitable and affect the web quality. Most of these defects are caused by the residual stresses resulting from winding. The magnitude of the residual stresses depends on the winding equipment, the operating conditions such as web tension, and the web and core properties. Winding models have been developed by web handling researchers to predict the residual stresses in the wound roll and understand winding defects. If the stresses are too low, the roll may not withstand handling loads without deforming. Telescoping or flat tire defects are some of the examples resulting from low pressure. Conversely if stresses are too high, the material may be damaged. Blocking of layers on sticky products and bulk reduction on tender products such as nonwovens are related to high stresses. Consequently, the web needs to be under tension for proper winding and handling, which can affect the nanoimprints.

The goal of the second part of the presented research is to predict the pressures in the wound roll and how the nanoimprinted features will be distorted through time while subject to those pressures. This will help in establishing how the imprinted materials should be wound and how long they can be subjected to pressure in the wound roll before they should be unwound to limit the deformation of the nanoimprinted features.

1.2 Motivation

For the lamination case study, the presented research can be applied to a process line for Roll-to-Roll lamination manufacturing. Ideally webs that are to be laminated are strain matched prior to lamination. If the laminator was able to induce no shear and MD strains in the laminae, this would result in a laminate with no MD curl. The reality is that shear and MD strains are induced by nip mechanics in the laminator. In some cases, it is not possible to match the MD strains in the webs to be laminated due to web transport issues upstream of the laminator. In such cases, the operator in the manufacturing industry uses a trial and error procedure to adjust the torque input to one of the laminator rolls, which affects the shear and MD strains in the nip zone, to produce laminates free of MD curl. In the present research work, a modeling tool, i.e. a lamination model, is developed to replace or augment the trial and error procedure to produce laminates free of MD curl. This modeling tool can include multiple laminator and web configurations, including the presence of a rubber cover on one of the rollers and the use of adhesive between web layers. For given webs being laminated, the lamination model produces machine operating charts that could forecast the level of MD curl produced for a given laminator. These charts will be functions of incoming strain ratio, wrap angle, torque magnitude and direction supplied to the rubber covered roller, and potentially the nip load.

For the nanoimprint lithography case study, the presented research focuses on the packing and storage phase of Roll-to-Roll Nanoimprint Lithography. Once the webs are imprinted with nanoscale features, the only convenient means of packing this continuous material is by winding it into wound rolls. Winding implies increased pressure on the nanoimprints, which may not be fully cured at the winding stage. Subsequent deformation of the features is expected but its level remains unknown. The imprints will undergo creep when subjected to constant wound roll pressure due to the resin viscoelastic nature. We developed a method to estimate the deformation of nanoimprint features according to time in the wound roll, which can then be used to tune process parameters, such as the winding tension, the maximum allowable laps of wound in one wound roll, the maximum storage time period, and the necessary storage conditions before unwinding to limit the deformation of the nano-imprinted features. For example, the model can determine how long before the actual process should the nanoimprinted web be unwound so that the creep relaxes. Given the viscoelasticity of the imprint resin, the storage temperature will influence the amount of creep and we can estimate a critical temperature at which the deformation is limited or frozen. This helps industries understand the winding mechanics of the imprinted web and what measures need to be taken to avoid excessive deformation of the nanoimprinted surfaces, which would affect the functionality of the end product.

**CASE STUDY 1: DEVELOPMENT OF LAMINATION MODELS IN
R2R MANUFACTURING**

CHAPTER II

INTRODUCTION TO LAMINATION PROCESS

In many web handling industries, lamination processes are common. Lamination is the technique of manufacturing a material in multiple layers to achieve improved strength, stability, appearance etc.

In R2R manufacturing, a roller set, *i.e.* one high stiffness, metal shell roller and one rubber-covered rigid roller, is commonly used to laminate the webs. In all the laminating processes, webs are combined or laminated in the nip contact zone. It is important to control the parameters that influence lamination to enhance the quality of the laminated web. Generally, webs are stored and transported in the form of wound rolls. Winders are used to convert straight webs to roll form. Nip rollers at the surface of a winding roll are common to reduce entrained air. From the winding research, it is shown that the nip induces contact shears called Nip Induced Tension (NIT) which is considered as an important parameter for winding. In the lamination process, similar interlayer shears are induced by the nip roller pair but the nip pressure is required to ensure the lamination adhesives attach the webs together.

The majority of laminations used in industry require the application of a bonding agent to join the webs together. These bonding agents can be glues, adhesives, hot melts, thermoplastic waxes, or extruded plastics. There are five basic types of lamination processes used in industries *i.e.* wet, dry, thermoplastic, pressure and extrusion laminating [26]. The categorization of all these laminating processes are

based on the bonding agent. In wet lamination, a water based glue made from starches, caseins, or synthetic materials is required. In dry bonding, a coating of a solvent-based or solid state adhesive is required. Waxes and paraffins are used as bonding agents in the thermoplastic lamination process. Some materials and coatings have the inherent ability to laminate themselves under combined heat and pressure. In extrusion lamination, molten plastics such as polyethylene are extruded onto one substrate to act as the bonding agent for laminate material. With inappropriate tension input, moisture, humidity etc., several issues such as bubbles, wrinkling, orange peeling, waving and curls are inevitable [27]. This research focuses on “curl” defects. In many manufacturing processes such as printed electronic circuits or baby diapers, the laminated material needs to remain flat and free of curl to ensure better quality and satisfy the customer needs.

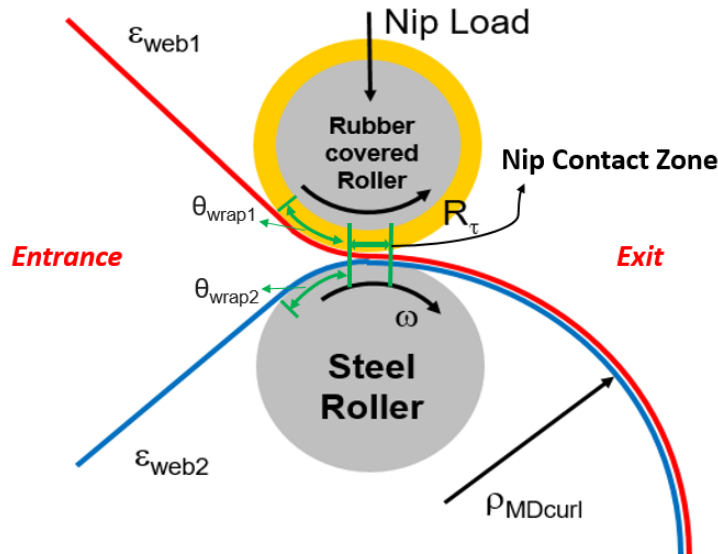


Figure 2.1: A Laminator

An embodiment of a generic web laminator is shown in Figure 2.1. Pretension-ed webs enter the nip roller and are laminated in the nip contact zone forming a multi-layered single web. After lamination, a curl can be witnessed. Some of the laminator

parameters that can affect curl are: incoming web membrane strains or tensions, incoming web wrap angles, bending and nip induced shears in the nip contact zone (which are affected by roller diameters, nip load, and rubber cover character), rigid roller angular velocity, rubber roller torque, exit wrap of laminated web, and the temperature of web membranes. Frictional characteristics between the webs and rollers at contact, web and adhesive material characterization can also affect the curl. Webs can be characterized as either elastic or viscoelastic depending on the creep time constants and the residence time in the nip contact zone. The adhesive can be modelled as a viscous layer between the web layers, which produces shear distortion. In roll-to-roll manufacturing, the curl of the laminated web at the exit can be predicted by the Machine Direction (MD) strains in the entering webs for the case when the two rigid rollers in the laminator are equal in diameter and friction coefficient and no slip is allowed between the two web layers in the nip contact zone. The MD strain (ϵ_{MDi}) can be predicted from the web incoming tension (T_i), cross section of the web on which tension is applied (A_i) and Young's modulus of the web laminae (E_i) as shown in Equation (2.1). Here, the subscript "i" denotes the corresponding laminae. For known E_i and A_i , by controlling the web incoming tension, T_i , the two webs can have equal or "Matched" strains induced to eliminate the curl tendency.

$$\epsilon_{MDi} = \frac{T_i}{A_i E_i} \quad (2.1)$$

In most cases, lamination nip rollers are required, one of which will be rubber covered. The rubber cover helps produce a wide nip contact zone to create pressure across the web width to set the adhesive. In that case, shear and MD strain induced by nip mechanics will influence the curl. Predicting the curl becomes more complex. Also, bending at the laminating nip zone due to entering and existing wrap angle and rubber cover deformation will influence the curl after lamination. The wrap angles

are the angles at which the web wraps the rollers prior to and after nip contact. More wrap angle means more contact with the roller.

From above, it is clear that parameters that potentially need to be controlled to minimize the curl after lamination are incoming web tensions, nip loading, torque to the rubber covered roller, nip roll diameters, rubber properties, incoming and exiting wraps angles and possibly existing tension on the laminated webs. In industries, the operators use trial and error procedures to adjust the torque input to one of the laminator rolls to produce laminates free of curl. The WHRC sponsors requested the development of a modeling tool to replace or augment the trial and error procedure to produce curl free laminates. The goal of this research is to develop a lamination model to predict the curl after lamination. Different cases will be simulated to develop specific input parameters for unique webs and adhesives that minimize MD curl.

CHAPTER III

LITERATURE REVIEW

3.1 Review on nip mechanics in Winding and Calendering models

An understanding of nip mechanics in R2R manufacturing is important. This will help to understand how shear strains in the nip rollers, nip induced tension etc., affect the machine direction (MD) curl of the laminated web. Some of the literature on winding and calendering models are discussed in this section. The winding models discussed in this section are center winding and surface winding. Winding is accomplished by providing a torque to the core shaft in center winding or to the nip roller in case of surface winding as shown in Figure 3.1. In winding models, it is important to determine the internal stresses to provide a valuable tool for optimal selection of winding control parameters. This wound roll internal stress profile is determined by wound-on-tension (WOT). The WOT is the tension in the outermost layer of a winding roll that is created due to the incoming web tension and the tension induced by the nip roller called Nip-induced-Tension (NIT). If the WOT and elastic moduli of web are known, the internal stress of the wound roll can be calculated. Many works have been done starting in the late 1960's to determine the WOT for different winding models and the effect of nip roller either experimentally or numerically.

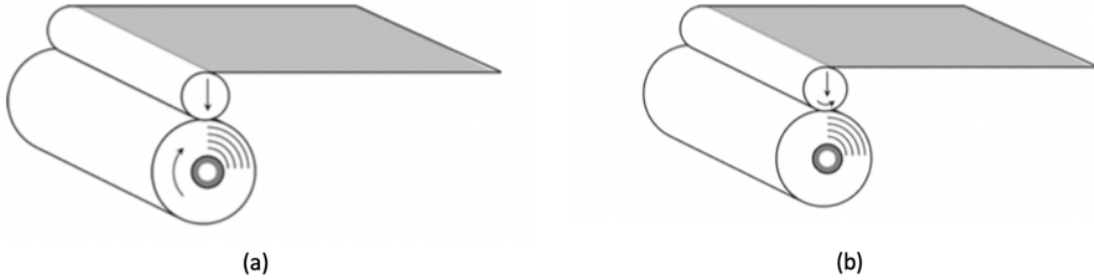


Figure 3.1: Winding model (a) Center winding; (b) Surface winding

The study of wound roll structures by measuring WOT started with Pfeiffer [28,29]. He observed that the rolls wound in either center or surface winding with an impinging nip roller produced harder rolls, as compared to those wound without any nip loading. He used a flat bed rolling nip test bed to understand the nip mechanics in the winding process. The tester consists of a rigid base on top of which a stack of sheets clamped to a load cell at one end were placed. A rigid nip roller traversed these sheets inducing additional tension in the web. The tension on the exit side of the top sheet increases as the nip starts rolling and saturates to a final value commonly referred to as the NIT. The first quantitative data [28] was presented which showed the effects of nip load, nip diameter, and the number of sheets in the stack upon the nip induced tensions in the stack sheets. Later, this flat bed experimental results combined with finite element simulations by Good [1,30].

In late 90's, a good amount of work was done by Good [1,30,31,32,33] on windings. Experimental and numerical analysis on the center winding process was performed [31] to calculate internal stresses within wound roll and the mechanism by which nip roller increases the WOT in the outermost layer of the web was also explained. A modified boundary condition which relies principally on the coefficient of friction and nip loading as shown in Equation (3.1) is applied on outer layer of web as circumferential stress in finite element analysis which is found to be performing

very well compare to experimental data.

$$\sigma_r|_{r=s} = \left[T_w|_{r=s} + \frac{\mu N}{h} \right] \frac{h}{s} \quad (3.1)$$

Here, N is the nip load, μ is the coefficient of friction, h is the web thickness, T_w is the input web tension and s is the radial location of outermost layer in the roll. The results showed that the mechanism responsible for inducing nip induced tension is an elongating machine direction strain which exists in the nip contact zone on the lower side of the web which is in intimate contact with the wound roll. This elongating strain is due to the compressive Hertzian-like contact stresses which exist through the depth of the web beneath the nip roller. Here, Hertzian contact stresses are defined as the localized stresses that are developed as two curved surfaces come in contact and deform slightly under the imposed loads. As this elongating strain advances with the moving nip roll, web attempts to advance in front of the nip and contract in towards the nip in back of the rolling nip. If the web in back of the nip is constrained, a net increase in tension will result due to the nip. The NIT is calculated as kinetic coefficient of traction between the outer wrap and the wrap beneath it multiplied by the nip loading and the saturated value of nip induced tension can be obtained by adding web line tension to the NIT. Later, Good [1] conducted both numerical and experimental studies on a center winder with an impinging nip roller to understand the nip-induced tension mechanism further in detail. The relation for web Stress in machine direction (MD) was developed from experiments as shown in Equation (3.2). Here, C_1 , C_2 represents the saturation value, growth rate of the nip-induced stress respectively and C_3 represents web pretension prior to nip rolling. A model for a stationary web with moving Hertzian parabolic pressure through time applied on the top layer as shown in Figure 3.2 was developed for finite element analysis. The strain in the web was calculated using Equation (3.3). The elongating MD strain of the

web (on lower side) beneath the nip roll location was proved to be responsible for the nip-induced tension in wound rolls. Later on, a new boundary condition similar to [31] for wound roll stress models i.e. the outer wrap was set equal to the sum of the incoming web stress and the saturated value of the nip induced tension was introduced in finite element analysis which compared quite well with the experimental results. The models reported in this work [30] can be used for center winding with an undriven nip or surface winding. It is seen that the saturated value of nip induced tension occurs after short nip rolling distance.

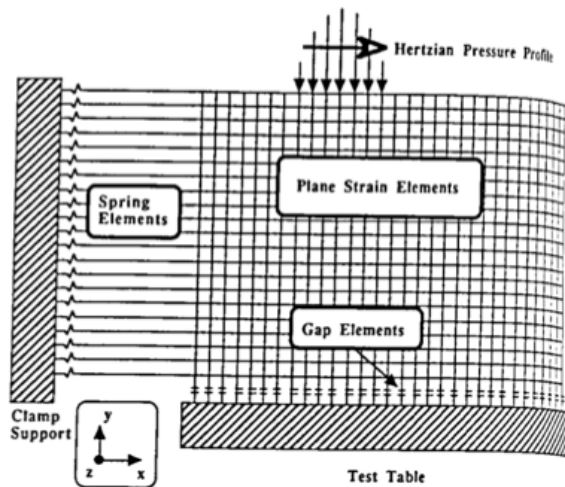


Figure 3.2: The Finite Element Model for a stationary web with moving Hertzian parabolic pressure [1]

$$\sigma_x = C_1 [1 - e^{-C_2 x}] + C_3 \quad (3.2)$$

$$\epsilon_{web} = \frac{6.823 \times 10^{-5} \times N.R.D}{L_i + N.R.D} \quad (3.3)$$

In 1999, Good [32] conducted an experimental analysis to compare Center and surface winding by calculating Wound-On-Tension (WOT) using measuring technique defined by Pfeiffer [28]. The outer layer of web was pulled away from a winding roll and a measure of the web tension was made prior to returning the web to the surface

of the winding roll. This way WOT is studied as a function of winder type and as a function of winder and web line operating parameters. For different web tensions and nip loads, the experiments were conducted on both center and surface winding with 180 degrees wrap on the nip roller to measure the WOT. In case of center winding, WOT was found to be dependent on web tension whereas nip load effected the WOT for surface winding. WOT is calculated by Equations (3.4) and (3.5).

$$WOT_{centerwinding} = T_w + NIT \quad (3.4)$$

$$WOT_{surfacewinding} = \begin{cases} NIT & 0 \leq \text{Nip Load} \leq 17.5 \text{ N/Cm} \\ NIT + \frac{T_w}{e^{\mu_{wn}\beta}} \frac{N}{58.3} & 17.5 \leq \text{Nip Load} \leq 58.3 \text{ N/Cm} \end{cases} \quad (3.5)$$

Here, T_w is the input web tension, N is the nip load, β is the angle of wrap of the web around nip roll i.e. 180 degrees, μ_{wn} is the kinetic coefficient of friction between the web and nip roller i.e. 0.2. A working model to predict WOT was proposed by Good [33] for center and surface winding using newspaper print and polyester web materials. This working model was found to be well consistent with the experimental results. The WOT for center and surface winding was calculated using the Equations (3.6) and (3.7).

$$WOT_{centerwinding} = T_w + \mu_k P \quad (3.6)$$

$$WOT_{surfacewinding} = \mu_k P \quad (3.7)$$

Here, T_w is the web line tension load per unit width, μ_k is the kinetic coefficient of friction between the web layers, P is the nip load per unit width. For center winding, WOT was found to be dependent on web tension and NIT satisfying Equation (3.6). The WOT for surface winding was dependent on the NIT for low nip loads satisfying Equation (3.7) whereas for high nip loads, WOT depends on both web tension and NIT. To understand the contact mechanics in nip contact zone, the slippage (frictional

forces) between the nip roller and webs, web and web were determined by calculating the pressure in contact zone. It was found that the slippage between the nip roller and web was less compared to the slippage between the web to web and so the friction forces between the nip roller and web had little effect on NIT when the incoming web did not wrap the nip roller.

Using the explicit finite element method, WOT for both center and surface winding process was developed by Kandadai [2] as shown in Figure 3.3. WOT is calculated as sum of the incoming web tension and the integrated value of the net traction which was calculated as the sum of the top and bottom surface tractions in the contact zone as shown in Equation (3.8).

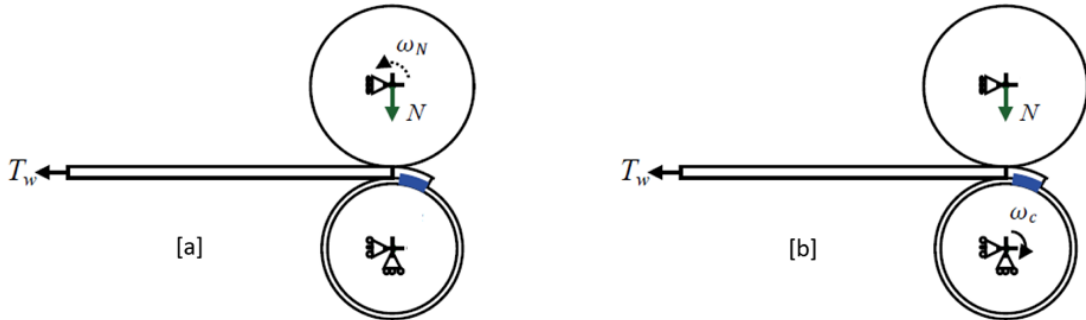


Figure 3.3: (a) Surface winding; (b) Center winding [2]

$$T_{out} = T_{in} + \int_{-a}^a [q_{top}(x) + q_{bot}(x)] dx \quad (3.8)$$

Where, $Q = \int_{-a}^a [q_{net}(x)] dx$ and $q_{net}(x) = q_{top}(x) + q_{bot}(x)$

Here, T_{in} the income web tension, T_{out} is the total web tension on outer layer i.e. WOT, Q is the total traction and q_{net} is the net traction i.e. sum of top and bottom surface traction acting across the web layer (q_{top} and q_{bottom}). The results showed that the surface traction in the nip contact zone governs the WOT development. In the nip contact zone, the top surface traction of topmost layer exhibits three distinct regions:

Slip at both ends of contact and a large stick zone in the middle. This indicates that the surface that is under slip moves faster than the velocity of roller and the surface that is under stick moves equal to the velocity of the roller. Whereas the bottom surface is under micro-slip and exhibits five distinct regions: The surface is under slip at the edges of contact (the bottom surface of the web moves slower than the top surface of second layer in these zones), another slip zone exists in the middle of contact (surface moves faster than the top surface of second layer in this zone) and two intermediate stick zones exists between these slip zones wherein the surface velocities are equal. This micro-slip behavior in the bottom surface dictated the amount of NIT developed during winding process. For all the nip load levels, the difference between WOT in center and surface winding is equal to web tension. The numerical results showed that the NIT is approximately equal to ' $\mu_{web/web}N$ '. Here, $\mu_{web/web}$ is coefficient of friction between the webs and N is the nip load. For the same models used in the previous analysis, experimental studies were conducted by Kandadai [34] to verify the numerical results. WOT in the winding process is measured by load cell method. In the load cell method, the incoming web layer is pulled away from the winding roll prior to entering the winding roll, passed through an idler mounted on a load cell and then returned back to the winding roll such that the load cell measures the tension in the outermost layer. The measured tension is equivalent to WOT. This load cell method is also known as Wound-in-Tension measurement defined by Pfeiffer [28]. The measured WOT values compared well with numerical model results. Strain in the nip contact zone measured using contact strain gauges and is compared well with the numerical model results.

Calendering is generally used in many web handling industries such as paper, polymer, leather, printing and textile. It is a final stage of process where the material is pressed between two or more rollers to improve the surface quality by removing irregularities in the sheet formation. It is very important to study nip mechanics for

designing calendars and so many models were developed related to the calendaring by Diehl [4], Neel [3] etc.. The basic model for nip contact was first developed by Hertz [35] considering contact between two homogeneous rollers. A generalized model was developed by Neel [3] for designing soft calendaring as shown in Figure 3.4 to produce the required quality paper. This model overcame the difficulties of Hertz [35], Meijer [36] and Deshpande [37] models. Modifying Meijer's equation, an empirical relation for calculating nip width was developed as shown in Equation (3.9) which was found to be the deciding factor for quality of the paper. It was shown that the nip width is dependent on the equivalent elastic modulus, cover thickness, line load and diameter of the roller.

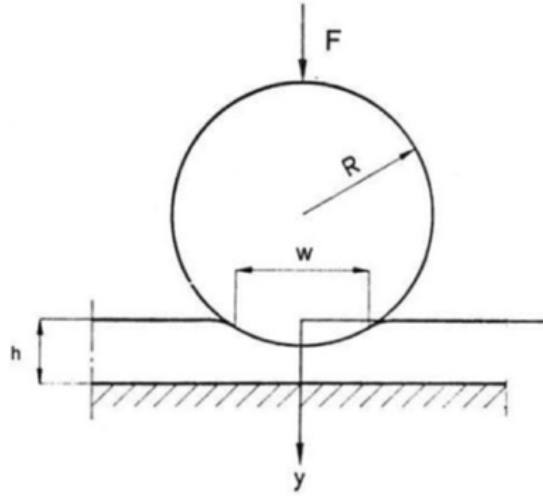


Figure 3.4: Geometry of the problem [3]

$$E^* = 2.1401 \frac{F D_E}{w^2} \left[1 + 0.2070 \left(\frac{w}{h} \right)^4 \right]^{-1} \quad (3.9)$$

Where, $\frac{1}{E^*} = \frac{1-\nu_1^2}{E_1} + \frac{1-\nu_2^2}{E_2}$; $\frac{1}{D_E} = \frac{1}{D_1} + \frac{1}{D_2}$

Here, E_1, E_2 and ν_1, ν_2 are the elastic modulus and Poisson's ratio of the rollers in contact; D_1, D_2 are the diameters of two rollers in contact; D_E is the equivalent diameter; w is the nip width and F is the nip load. Axial variation in nip parameters

such as contact pressure and contact area for two commonly used nip designs was studied by Diehl [4]. One is identical-hollow drum design that consists of two hollow drums of the same geometry both covered in elastomers and the other one is classic calendaring design where only one of the hollow drums is covered in elastomers as shown in Figure 3.5. A 3-D computation model was developed for the two models mentioned by assigning appropriate boundary conditions. The axial variation of nip parameters can cause web wrinkling, uneven material transfer, poor product quality and customer dissatisfaction. It was shown that the axial variation in the drum's deflection is the primary cause of axial variation of nip parameters.

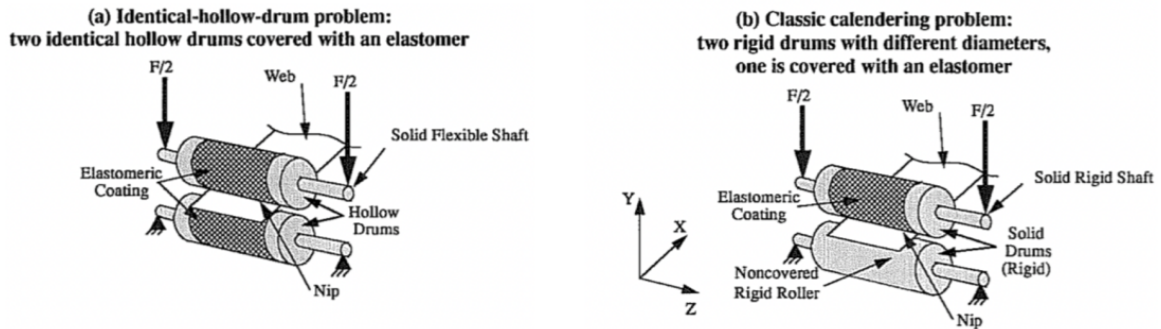


Figure 3.5: Schematic of 3-D nip mechanics problem [4]

From this section, it is clear that both nip and contact mechanics in nip contact zone are two important parameters for designing both winding and Calendaring models.

- From nip mechanics, it is shown that the elongating machine direction strain which exists in the nip contact zone on the lower side of the web which is in intimate contact with the wound roll is responsible for nip induced tension in the web.
- From contact mechanics, it is shown that the bottom surface of web that is in

contact with the roller will experience micro-slip which dictates the amount of NIT developed during winding process.

3.2 Review on nip contact analysis

This sections reviews literature on nip contact analysis to understand how the rubber covered roller effects the nip parameters. An extensive research can be found on nip contact analysis where nip consists of rigid and rubber-covered rollers with or without any material interposed between the rollers. Batra [5] was the first author to study cylinder contact with finite elements without any material interposed between the rollers as shown in Figure 3.6.

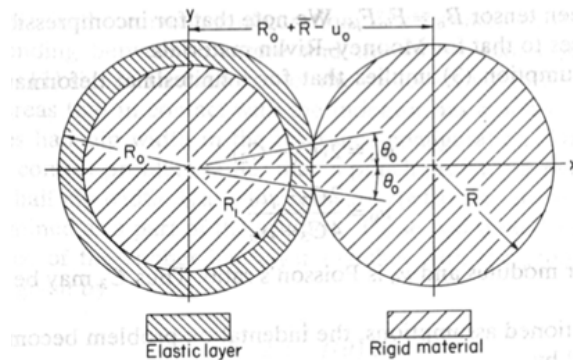


Figure 3.6: System to be studied [5]

The accuracy of the finite element code used for the analysis was established by comparing the computed results with the analytical solution for pressure vessel problem. The results showed that the compressibility of rubber had more effect on the pressure at the contact surface. Similar analysis was done later by Hahn [8] where they showed that the compressibility of the material had a noticeable effect on the pressure distribution at the contact surface and the stress distribution at the bond surface.

The stress distribution between the homogeneous elastic rollers as shown in Figure 3.7(a) was studied by Thomas [38] for plane strain conditions. Relations for the pressure distribution through the contact and width of contact were developed which were later used by many researchers for analyzing the nip with an elastic layer roller. Both numerical and computational analysis were conducted by Hannah [6] on the nip as shown in Figure 3.7(b) to determine contact stress and deformation in the elastic cover that is on the one of the nip rollers. There was no web material interposed between the rollers. Nip width, h_o and pressure distribution through nip, $P(x)$ were considered as the important factors of a nip in calculating contact pressure and deformation of the elastic cover. Plane stress conditions were assumed considered in this analysis. For homogeneous material, h_o and $P(x)$ are calculated using Equation (3.10) & (3.11) (developed by [38]).

$$h_o^2 = \frac{2WD}{\pi E} \quad (3.10)$$

Where, $\frac{1}{D} = \frac{1}{D_1} + \frac{1}{D_2}$

Here, $2h_o$ is the nip width; W is the applied load per unit length of the rollers, E is the Young's modulus of the elastic roller; D_1 and D_2 are roller diameters.

$$P(x) = P_m \left[1 - \frac{x^2}{h_o^2} \right]^{1/2} \quad (3.11)$$

Here, x represents distance measured from the center line of the nip ($-h_o \leq x \leq h_o$); P_m is the maximum value of the pressure at $x = 0$.

The soft roller was treated as a thin elastic cover on a hard-supporting core instead of treating it as homogeneous in this work and so nip width & pressure distribution through nip depends on the additional parameter known as cover thickness, b .

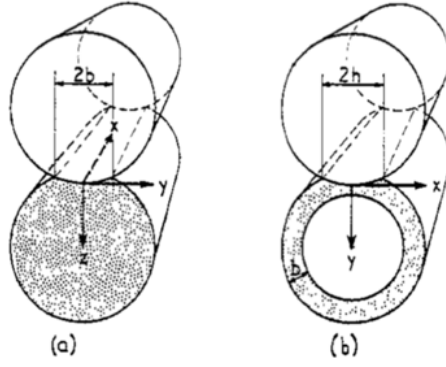


Figure 3.7: Nip configuration (a) Thomas and Hoersch's work; (b) Hannah's work [6]

Since the soft roller is not homogeneous, change in the nip width is given by the ratio h/h_0 , where $2h$ is the nip width for the layer thickness, b and change in pressure distribution is given by the ratio P_m/\bar{P} . It was shown that those two factors, h/h_0 and P_m/\bar{P} (i.e. peak pressure/mean pressure), depend only on the factor, K (K is the ratio nip width/cover thickness, $2h/b$). It was shown that after Roller Diameter (D) & Elastic modulus (E), the layer thickness, b is the most important in determining the relation between loading and deformation for this type of nip.

Considering the work of Hannah [6], similar research was conducted by Parish [39] both experimentally and computationally for plane strain condition. Elastic constants were modified form of the Hannah's solution for plane strain condition with Poisson's ration set to 0.5 (Equation (3.12)). The experiments showed that the properties of the nip were governed primarily by the properties of soft roller. Nip width, h_0 and pressure distribution through nip, $P(x)$ were considered as the important features of a nip which are calculated using Equation (3.12) and (3.13) respectively.

$$h_0^2 = \frac{2WD(1 - \nu^2)}{\pi E} \quad (3.12)$$

Where, $\frac{1}{D} = \frac{1}{D_1} + \frac{1}{D_2}$; $\frac{1}{\nu} = \frac{1}{\nu_1} + \frac{1}{\nu_2}$ and $\frac{1}{E} = \frac{1}{E_1} + \frac{1}{E_2}$

$$P(x) = P_m \left[1 - \frac{x^2}{h_0^2} \right]^{1/2} \quad (3.13)$$

Experimental work was continued by Parish [40] to study the rolling creep in case of rubber covered roller. Rolling creep is the phenomenon where bodies in rolling contact have different peripheral speeds. It was found that the rubber covered roller always had a lower peripheral speed than a rigid roller, whether the covered roller is driving or driven. The rolling creep was observed to be mainly due to the extension of covered surface which has two components: one is due to the normal loading and the other is forces necessary for torque transmission through the nip. The rolling creep was found to increase with load and decrease with rolling speed. The extension of surface due to normal loading was found from distribution of strain component of the nip, which is dependent on the parameter $K = h/2b$. Here, $2h$ is the nip width and b is the thickness of the rubber cover. Parish [41] extended his work for non-uniform loading conditions and the nips with two identical/dissimilar rubber covered rollers. For non-uniform loading, an additional relation to find the deflection of roller was established to calculate nip width and pressure distribution through the nip. In case of identical rubber-covered rollers, calculations to find nip width and pressure distribution through nip for both uniform and non-uniform loading conditions were similar to Parish [39] & [41] respectively except the diameter, D in Equation (3.12) was set equal to the diameter of rubber covered roller ($1/D_2 = 0$). With the help of Hannah [6] and Parish [39,40,41] works, many researches have been done later by Bettina [42,43], Joonas [44], Miller [45], Austrell [7,46]. Analytical expressions for nip maximum pressure (P_{max}), the nip width (b), the surface strain in the center of the nip (ϵ_t) and indentation (u) as represented in Figure 3.8 were developed by Austrell [7] as shown in Equations (3.14) to (3.17) which were validated by finite element analysis. The constant terms in the equations $C_1 - C_{18}$ were determined by least square fitting from FE results. It was clear from the relations that the nip parameters depend only

on the properties of rubber cover.

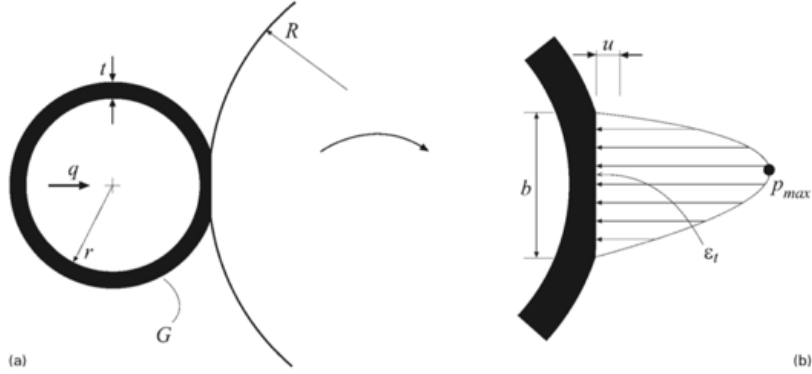


Figure 3.8: (a) design (or input); (b) response (or output) variables of roller configuration [7]

$$P_{max} = \frac{q}{b} f_p(X, Y) \quad (3.14)$$

$$b = b_0 f_b(X, Y) \quad (3.15)$$

$$\epsilon_t = \frac{t}{D} f_\epsilon(X, Y) \quad (3.16)$$

$$u = \frac{t^2}{D} f_u(X, Y) \quad (3.17)$$

Where; $X = \frac{b_0}{t}$, $Y = \frac{G}{G_0}$, $f_p = C_{11} + C_{12}e^{-\frac{X}{10}}$, $f_b = \frac{C_1 + C_2 Y^{1/2}}{(C_3 + C_4 Y^{1/2} + X)^{1/2}}$,
 $f_\epsilon = 1 - e^{X(C_{17} + C_{18} Y^{-1/100})}$, $f_u = (C_5 + C_6 Y + C_7 Y^2)[1 - e^{C_8 X Y^{3/10}}] X^{C_9 + C_{10} Y^{1/10}}$

In Miller [45] work, it was shown that the rolling creep depends on cover indentation, thickness and material used. Unlike Parish [40], his experiment results showed a case with a covered roll having higher peripheral speed than a rigid roller due to compressibility between cover materials. The effect of indentation depth was found to be dependent on the cover material. This indentation issues were later addressed by Meijers [47], Bentall [11] and Alblas [48] to evaluate the effect of compressibility on nip. They showed that the rolling creep depends on the compressibility and cover thickness.

Up to now research on the nips without any material imposed between the rollers have been reviewed to understand the effect of rubber cover on the nip system. Numerous works have been done on the nips with an elastic strip imposed between the roller by Soong [49,9,50], Johnson [35], Diehl [51,52], Stack [53], Bental [11] etc... Rolling contact problems with an elastic-layer cylinders imposing a sheet between the cylinders were studied numerically by Soong [49,9,50]. In his first work [49], a numerical procedure was developed to solve an elastic plate with initial curvature compressed between two cylinders, one is hard and the other has a soft layer on a hard core using stress functions developed by Hahn [8] as shown in Figure 3.9(a). Later contact analysis was studied on a flat elastic plate that is compressed between the cylinders [9], both have an elastic layer on the hard core as shown in Figure 3.9(b) based on small deflection elasticity theory. Stress distribution, deformation and surface speed for the cylinders and the sheet were calculated. It was found that the significant slip was not produced to affect the speed ratios with no net traction on sheet and coefficient of friction < 0.3 .

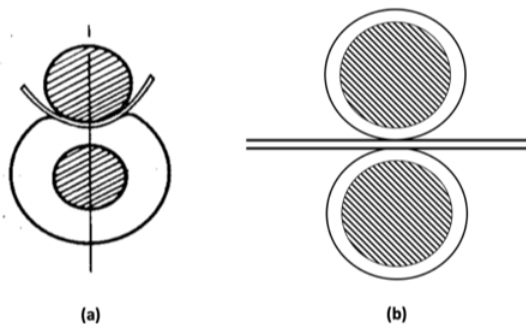


Figure 3.9: Roller configuration considered for analysis [8, 9]

For different nip materials, the mechanics of web transport through a set of rollers was explained by stack [10] using speed ratio. Speed ratio is the ratio of web transport speed to the nominal surface speed of roller. Nonlinear finite element simulation of a web transported through a set of rollers is conducted using symmetry condition as shown in Figure 3.10. Depending upon the strain in the nip, speed ratio can be

less (underdrive) or more (overdrive) than 1. The hoop strain (circumferential strain) of the nip roller will define how fast a particle on the outside of roller can move. Poisson ratio of the material is shown to be driving factor behind how a particular nip material behaves. For soft nip materials, web tension is shown to affect the web speed significantly. It is shown that the rubber and polyurethanes have tendency to overdrive i.e. web transport speed is greater than the speed of a roller. In present research, nip roller of rubber material is used and so web travelling at speed greater than roller input velocity can be seen.

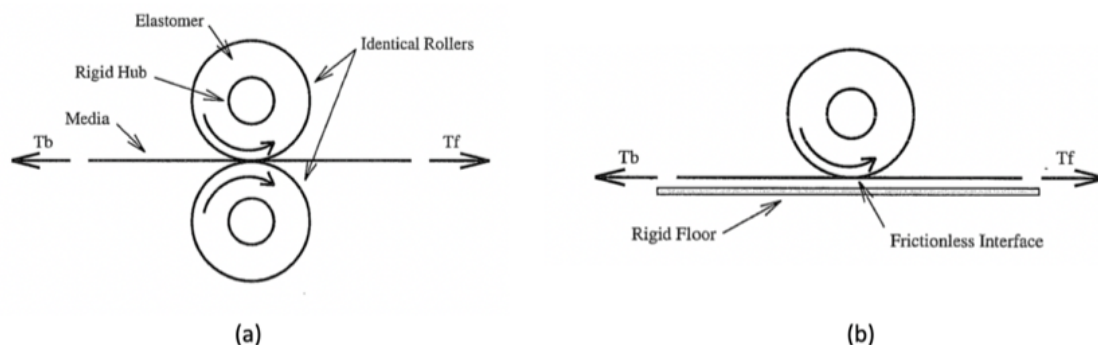


Figure 3.10: (a) actual geometry with two elastomeric transport rollers; (b) Symmetry condition used for analysis [10]

Two cases i.e. an elastic strip passing between the two elastic rollers and the elastic strip covered on to the one of the rollers in the nip as shown in Figure 3.11 were analyzed by Bental [11] using a modified Hertzian solution. It was shown that the surface shear affects the stresses within the strip and the rate at which the strip feeds through rollers i.e. “Creep”. For the case nip with different materials for roller and strip, slip was observed at the edge of contact. With this slip and creep conditions, strip’s underdrive and overdrive behaviour were computed.

From reviewed literature, it was clearly understood that the properties of rubber/soft cover play a significant role in nip mechanics with or without any material imposed between the rollers. For the lamination process, curl in the laminated web occurs due to the web tension. From this section, the parameters that influences the

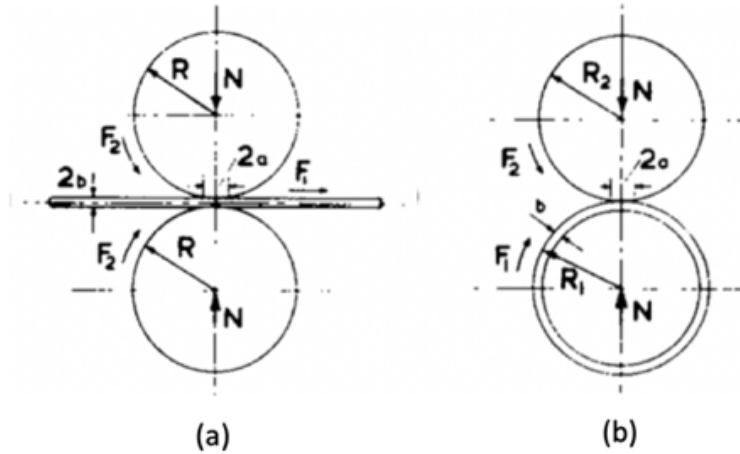


Figure 3.11: Basic Strip Configurations [11]

tension in the web are reviewed.

For the case of nips without any material interposed between rollers,

- Pressure distribution at the contact surface is dependent on few parameters such as compressibility and material properties of rubber cover, layer thickness
- "Rolling Creep" is observed mainly due to the extension of rubber covered surface.

For the case of nips with a material strip interposed between rollers,

- Surface shear are shown to effect the stresses within the strip that is passed between the rollers and the rate at which strip feeds. This feed i.e. speed ratio depends on the strain in the nip.

3.3 Review of MD curl due to winding single webs

In the research conducted by Sheng Pan [54], MD curl was analyzed for viscoelastic single layer web that is subjected to winding. Bending recovery theory was introduced

in the winding code to predict the curl for hundreds or thousands of layers winding at a certain radius. Bending recovery (BR) is defined to represent the recovery of the curvature i.e. $\frac{R}{\rho}$. Here, R is the radius of the core or position in the roll where the web is wound, and ρ is the radius of curvature of the web. If the web is flat, BR should be 0 while BR is equal to 1 if the web is totally viscoelastic. Depending on the relaxation of stresses, BR can be calculated using Equations-(3.18) & (3.19). When the compressive stresses relax substantially slower than tensile stresses i.e. $E_{com}(t_r) = E_0$, Equation (3.18) was used to calculate the Bending recovery (BR_1). Whereas for the relaxation of the stresses independent of the sign of the stress i.e. $E_{com}(t_r) = E_{ten}(t_r)$, Equation (3.19) was used to calculate the Bending recovery(BR_2).

$$BR_1 = \frac{1}{2} \left[1 - \frac{E_{ten}(t_r)}{E_0} \right] \quad (3.18)$$

$$BR_2 = \left[1 - \frac{E_{ten}(t_r)}{E_0} \right] \quad (3.19)$$

For the viscoelastic web, different relaxation effect for tensile state and compression state was pointed out in his work. For one or two laps of winding, Finite Element model was developed for a single layer web to analyse the MD curl after certain storage time. Further, experiments were conducted where online measurement method was developed to quantify the relationship between MD curl and CMD curl. Here, a Kappa gauge [16] was used to measure the radius of curvature form harvested specimen.

Bending recovery for the laminate viscoelastic winding model was discussed by considering equivalent elastic modulus and creep function of the laminated web. It was mentioned that this could be used for the laminated web curl analysis. Here, the adhesive between the laminae were neglected. also, the curl analysis was considering during winding (not during the lamination process). Therefore, the present research

topic focuses on the curl analysis of laminated web after the lamination process.

3.4 Review on lamination of the webs

Very few research works can be found for the modeling of lamination process. Curl of the laminate is the driving influence for modeling the laminated webs. The laminating parameters that effect the development of Machine Direction (MD) Curl was first reviewed by Werner [12] and presented soft roll drive configuration & an empirical procedures to provide effective influence in correcting for MD curl. In laminator section where multiple webs are laminated, the balance of the tensions in and out of laminator is supported by the roller surface forces (Equation (3.20)). Here, T_1 and T_2 are web tension in the upstream region, T_3 is the tension on the laminated web as shown in Figure 3.12, $R_{(SR)}$ and $R_{(HR)}$ are the radius of hard and soft roller and $NPLSS_{(SR)}$ is the soft roll nip loss i.e. force required to work (or extrude) the surface cover of soft roll.

$$F_{s(SR)} + F_{s(HR)} = [T_1 + T_2] - [T_3] + NPLSS_{(SR)} \quad (3.20)$$

Where; $F_{s(SR)} = \frac{Trq_{SR}}{R_{(SR)}}$ and $F_{s(HR)} = \frac{Trq_{HR}}{R_{(HR)}}$

By controlling surface-to-surface laminator roller forces through the laminate strips using adjustable torque controllers, MD curls are minimized or eliminated using soft roll drive configuration. In this study, two types of configurations are developed; Load shared torque controlled soft roll drive configuration and Independent torque profiling soft roll drive. The first type configuration as shown in Figure 3.12(a) is used when it is desired to have the load/torque of the soft roll drive at a particular percentage of the hard roll drive. So, the soft roller torque, $Trq_{(SR)}$ and total torque, $Trq_{(total)}$ can be calculated using the Equations (3.21) and (3.22) respectively. Here,

LS is load share factor and $Trq_{(HR)}$ is hard roller torque. This method of control is moderately successful when the desired relative load of the Soft Roll is not particularly high compared to the Hard Roll Drive.

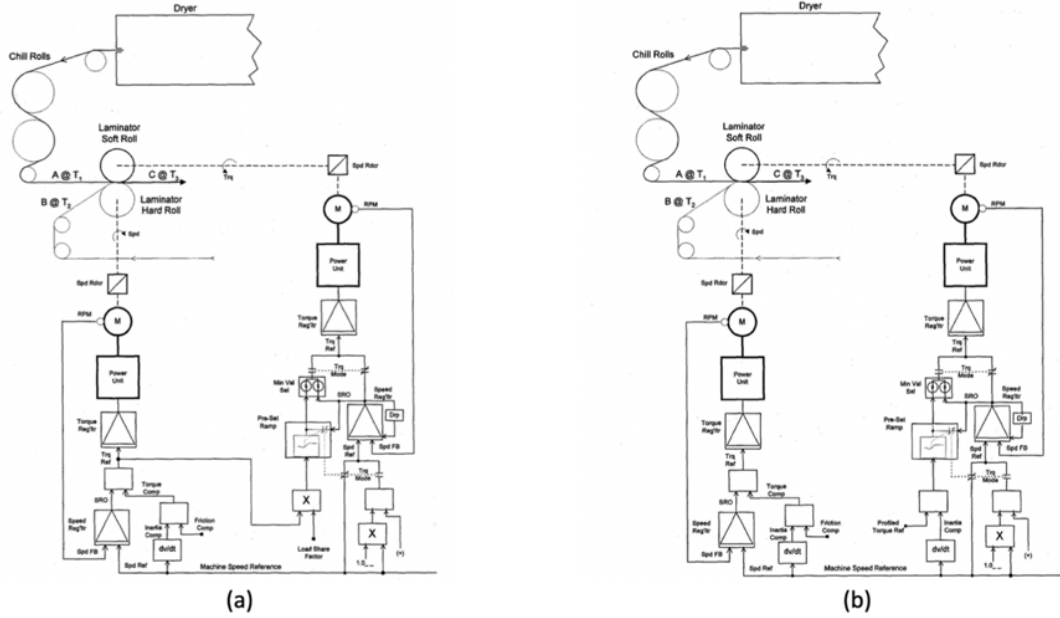


Figure 3.12: (a) Speed regulated hard roll drive; (b) Load share torque soft roll drive [12]

$$Trq_{(SR)} = LS + Trq_{HR} \quad (3.21)$$

$$Trq_{(total)} = (1 + LS)Trq_{HR} \quad (3.22)$$

In the later configuration i.e. Independent torque profiling soft roll drive, torque reference for the soft roll drive is independently profiled so that it gives optimum control of the Laminating Nip surface-to-surface forces that influence MD Curl. The largest portion of the surface force related torque required for the laminator section is to support the soft roll nip losses ($NPL_{SS(SR)}$).

In lamination process, multiple layers of web are transported into a loaded nip

roller system to form a single cohesive laminated web. The lamination process involves one of the webs being heated or cooled using hot or chilled roller before laminating. So, thermal effects from heated rolls & ambient air and hygral effects; heat transfer in the nip and free web span was considered by Pagilla [13] to model dynamics of the longitudinal behavior of a laminated web. First, the dynamic model for web strain is developed and then relation between strain and tension is obtained using constitutive relation to determine the tension dynamics. For single span web as shown in Figure 3.13, the strain dynamics is developed considering thermal and hygral effects using Equation (3.23). Here, the total strain, $\epsilon_i(x, t)$, is composed of three terms: Tension dependent, ϵ_{ti} ; temperature dependent, $\epsilon_{\theta i}$ and moisture-dependent, ϵ_{hi} . To determine thermal strains, the web temperature at the end of the free web span will be computed based on the heat transfer in the region of wrap on the previous roller and the free web section. Hygral strain is determined based on the average moisture content in the web using Fickian diffusion.

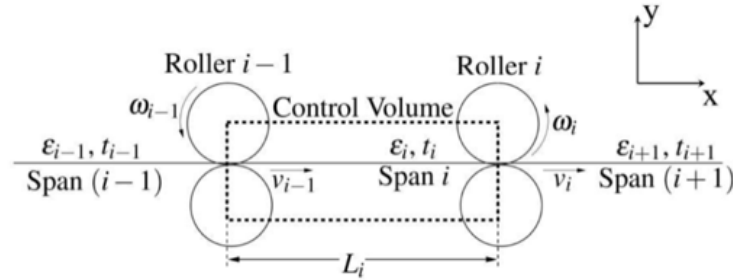


Figure 3.13: Basic Strip Configurations [13]

$$\frac{d}{dt} \left[\int_0^{L,i} \frac{dx}{1 + \epsilon_i(x, t)} \right] = \frac{v_{i-1}}{1 + \epsilon_{i-1}(t)} - \frac{v_i}{1 + \epsilon_i(t)} \quad (3.23)$$

Once the strain dynamics is calculated, tension dynamics is obtained by developing a model that gives relation between tension and strain. Here, web is assumed to be either elastic or viscoelastic. For elastic webs, the model is obtained using linear

constitutive relation. For viscoelastic webs, a simple model that consists of Maxwell model and a linear spring, also known as Generalized Maxwell model. Using the rule of mixtures on the mechanical and physical properties of the individual webs, properties of the laminated web as show in Figure 3.14 are derived using Equations (3.24) – (3.28).

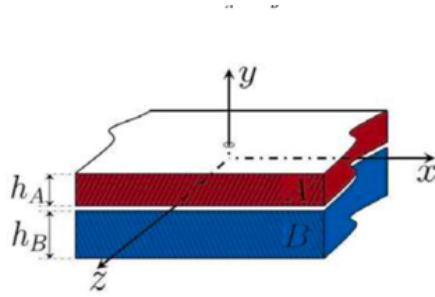


Figure 3.14: Lamination of two webs [13]

$$E_{cx} = \frac{E_A h_A + E_B h_B}{h_A + h_B} \quad (3.24)$$

$$E_{cy} = \frac{E_A E_B (h_A + h_B)}{E_A h_A + E_B h_B} \quad (3.25)$$

$$\rho_c = \frac{\rho_A h_A + \rho_B h_B}{h_A + h_B} \quad (3.26)$$

$$\alpha_{cx} = \frac{E_A \alpha_A h_A + E_B \alpha_B h_B}{E_A h_A + E_B h_B} \quad (3.27)$$

$$\alpha_{cy} = \alpha_A \nu_A (1 + \nu_A) + \alpha_B \nu_B (1 + \nu_B) - \alpha_v (\nu_A^2 + \nu_B^2) \quad (3.28)$$

Here, E_{cx} , E_{cy} are Youngs Modulus of laminated web in X and Y direction respectively, ρ_c is the density of laminated web, α_{cx} and α_{cy} are coefficient of thermal expansion for laminated web in X and Y direction respectively. Based on the mathematical model for single webs and composite properties of the laminated web, a dynamic model for web tension in the laminated web span is derived.

A two-dimensional curl prediction tool was developed by Kidane [14] based on

Laminate Theory which were validated by both Finite Element Analysis and Experimentation. A glimpse of the model developed in this paper is shown in the equations below (Equations (3.29) – (3.32)). In the equations, L , T represents Longitudinal and Transverse direction respectively.

$$\begin{bmatrix} \sigma_L \\ \sigma_T \\ \tau_{LT} \end{bmatrix} = \begin{bmatrix} Q_{11} & Q_{12} & 0 \\ Q_{12} & Q_{22} & 0 \\ 0 & 0 & Q_{66} \end{bmatrix} \begin{bmatrix} \epsilon_L \\ \epsilon_T \\ \gamma_{LT} \end{bmatrix} \quad (3.29)$$

Where; $Q_{11} = \frac{E_L}{(1-\nu_{LT}\nu_{TL})}$; $Q_{22} = \frac{E_T}{(1-\nu_{LT}\nu_{TL})}$; $Q_{12} = \frac{\nu_{LT}E_T}{(1-\nu_{LT}\nu_{TL})} = \frac{\nu_{TL}E_L}{(1-\nu_{LT}\nu_{TL})}$
and $Q_{66} = G_{LT}$

$$\begin{bmatrix} N_{3 \times 1} \\ M_{3 \times 1} \end{bmatrix} = \begin{bmatrix} A_{3 \times 3} & B_{3 \times 3} \\ B_{3 \times 3} & C_{3 \times 3} \end{bmatrix} \begin{bmatrix} \epsilon_{3 \times 1}^0 \\ k_{3 \times 1} \end{bmatrix} = [K] \begin{bmatrix} \epsilon_{3 \times 1}^0 \\ k_{3 \times 1} \end{bmatrix} \quad (3.30)$$

Where; $A_{ij} = \sum_{k=1}^n (Q_{ij})_k (h_k - h_{k-1})$, $B_{ij} = \frac{1}{2} \sum_{k=1}^n (Q_{ij})_k (h_k^2 - h_{k-1}^2)$,
 $D_{ij} = \frac{1}{3} \sum_{k=1}^n (Q_{ij})_k (h_k^3 - h_{k-1}^3)$

The quantities Q_{ij} in the matrix are called stiffness matrix elements which can be calculated from engineering constants. Equation (3.29) shows the relation for single laminae. For laminates made of n orthotropic layers, the relationship between the mid plane strains and curvatures (ϵ^0 and k) and per unit applied forces and moments (N and M) is given by Equation (3.30). Using Equation (3.31) & (3.32), applied load and moments can be calculated. The values of layer thickness from mid plane i.e. h_n can be calculated with the help of Figure 3.15. There are many factors that

are responsible for curl in laminated webs and the factors considered in this study are curls due to hygro-thermal expansion, strain mismatch (considered $\Delta T = 1$ for Equations (3.31) & (3.32)) and coating shrinkage. Stiffness matrix for each lamina is calculated (Equation (3.29)) and they are combined using Equation (3.30) to form Global stiffness matrix $[K]$. The inverse of $[K]$ matrix is multiplied with the applied forces and moments matrix to find mid plane strains and radius of curvature also called “Curl” in both machine and cross-machine directions. Curls for the cascaded lamination process can also be calculated by using the principle of superposition of the model. Results from Finite element analysis using ANSYS and experimental matched quite well with the model. Even though the simulations agreed with the test data, they did not account for the rolling contact of a laminator which the present research focuses on.

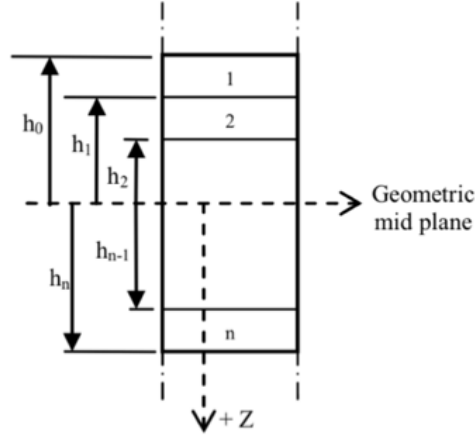


Figure 3.15: Layer thickness nomenclature [14]

$$N_{3 \times 3} = \Delta T \sum_{k=1}^n \begin{bmatrix} Q_{11} & Q_{12} & 0 \\ Q_{12} & Q_{22} & 0 \\ 0 & 0 & Q_{66} \end{bmatrix} \begin{bmatrix} \alpha_L \\ \alpha_T \\ 0 \end{bmatrix} (h_k - h_{k-1}) \quad (3.31)$$

$$M_{3 \times 3} = \frac{\Delta T}{2} \sum_{k=1}^n \begin{bmatrix} Q_{11} & Q_{12} & 0 \\ Q_{12} & Q_{22} & 0 \\ 0 & 0 & Q_{66} \end{bmatrix} \begin{bmatrix} \alpha_L \\ \alpha_T \\ 0 \end{bmatrix} (h_k^2 - h_{k-1}^2) \quad (3.32)$$

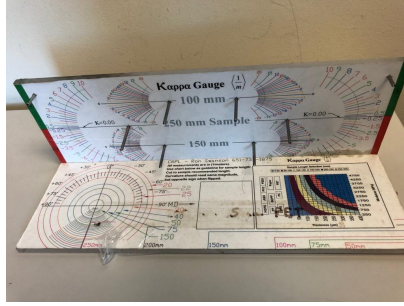
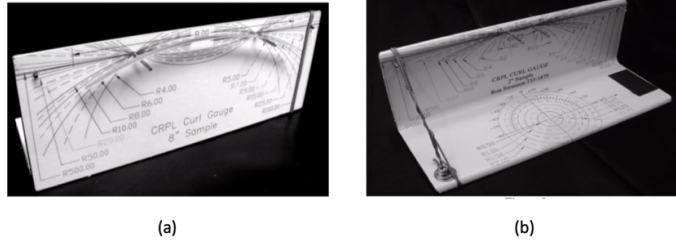


Figure 3.16: Kappa gauge [15]



(a) (b)
Figure 3.17: Curl gauge [16]

There are three basic measurement techniques for curl measurement used as currently accepted standards: Corner lift [55, 56, 57, 58], hanging strip test [59] and vertical axis test [60]. However, there were problems with these standards such as lack of useful units, static electricity, cupping, anticlastic bending, gravity, sample stiffness weight and twisting. A new curl measuring method called “CURL GAUGE” was presented by Swanson [16] as shown in Figure 3.17. It measures web curvature simply and quickly minimizing or eliminating the difficulties mentioned earlier. This method consists of placing a strip sample on two strategically spaced pins and reading curl radius on the background circular arc template. The tube radius can also be measured from bottom surface of the curl gauge as shown in the Figure 3.17 (b).

Making further improvement to Curl gauge, another device called “Kappa Gauge” was introduced by Swanson [15] at IWEB conference as shown in Figure 3.16.

CHAPTER IV

RESEARCH OBJECTIVE FOR R2R LAMINATION

MD curls were studied by considering parameters like surface-to-surface laminator roller forces [12], thermal and hygral effects from heated rolls & ambient air [13], and strains in the laminae [14]. In these studies, lamination model was considered for the rigid rollers with an elastic laminated web. To mimic the actual lamination process, the model becomes complex by introducing adhesive layer and rubber cover to one of the nip rollers.

From the literature review, it is clear that lamination modeling that encompasses the factors described in the Introduction is a topic unique to the literature.

The complexities of the problem involve:

- Bending and membrane strains at the point where the webs first contact.
- The interlayer shearing strain in the Nip Contact Zone and in the exit region where the laminate may wrap either the steel or rubber covered roller.
- The adhesive in shear and potential inelastic/viscoelastic behavior.

Dynamic simulations can be used to model the contact mechanics of this problem and is capable of resolving the complexities described. The research objective will be to estimate the MD curl produced by given parameters for the webs, adhesive and laminator using dynamic simulations.

CHAPTER V

NUMERICAL ANALYSIS OF LAMINATION MODELS

5.1 Development of lamination model

5.1.1 Model Setup

After the lamination of two or more webs, the MD curls are observed when the laminated web is set free from the machine processing. MD curls can be observed either bending towards the bottom roller or top roller depending on the strain in each web at which they got laminated. The mission is to build a robust lamination model in Abaqus to observe this MD curl. A 2-D finite element model is developed in this section to demonstrate the lamination process and study the MD curls at the end of lamination. In most of the lamination processes in the industries, pretensioned webs enter the nip rollers at a wrap angle, θ as shown in Figure 5.1(c) and leave the rollers as a laminated web. Nip load, N is applied on the rubber covered roller and angular velocity, ω is inputted to the rigid roller/rollers during the lamination. Tension in the laminated webs are removed at the end of lamination step to observe the MD curl.

Three different models are considered for the study in this section as shown in Figure 5.1. In model-III, the webs are entering the nip rollers at a wrap angle, θ . Idle rollers of 25.4 mm radius are used to make the webs enter at the defined wrap angle. Simulations are run for different wrap angles and web tensions to study their effect on MD curl. Whereas in model-II, straight webs that are separated by a rigid frictionless

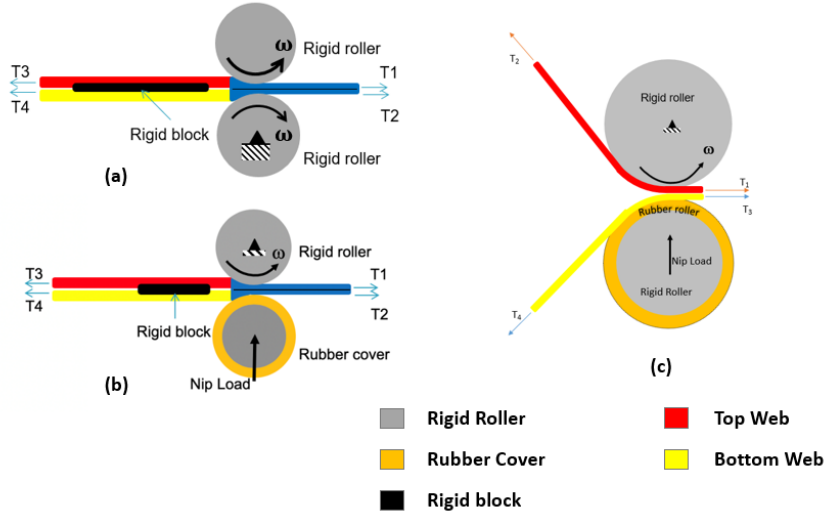


Figure 5.1: Model setup in Abaqus (a) Model-I, (b) Model-II, (c) Model-III

block before entering the nip rollers are laminated for different web tensions and nip loads. To study the effect of web tensions alone on the MD curls, webs are laminated in the nip rollers without rubber cover on one of the rollers as shown in Model-I. The geometry of the models is given in Table 11.1.

Table 5.1: Geometry of the model

Rigid Roller Radius, r	50.8 mm
Rigid Roller+Rubber Cover Radius, R	63.5 mm
Thickness of rubber cover, $t = R - r$	12.7 mm
Web length, L_w	431.8 mm
Web thickness, t_w	0.0254 mm
Rigid block length, L_b	381 mm
Rigid block thickness, t_b	0.0254 mm

An elastic web is considered in this study with mechanical properties: $E = 4136.85$ MPa, $\nu = 0.3$ and $\rho = 2.77E-8$ Kg/mm^3 . Material properties for rubber cover used in modeling are: $E = 4.26$ MPa, $\nu = 0.458$ and $\rho = 2.77E-8$ Kg/mm^3 . Since the rigid roller and rigid block are far stiffer than the web material, they are simplified with a rigid analytical surface in Abaqus.

The finite element method (FEM) is a numerical technique to find the appropriate solutions to boundary value problems. The partial differential equations need to be solved by the numerical methods. Appropriate numerical algorithms should be chosen for the finite element (FE) software to obtain the final results with accuracy and economy. The Abaqus solver is broadly classified into two types: Abaqus/Standard and Abaqus/Explicit for different types of analyses. Abaqus/Standard is based on the implicit scheme, specifically Newton-Rapson or Quasi-Newton method. Static and dynamic problems for both linear and nonlinear are solved by this scheme. For static problems, the discretized equilibrium equation as shown in Equation (5.1) is solved using Newton's method in implicit scheme as shown in the Equation (5.3) assuming the estimate of solution at iteration (i), $u_{(i)}^N$, is known. Here, P^N is the external force vector, I^N is the internal force vector created by stresses in the elements which can be calculated using Equation (5.2), V is the current volume of the model, $\sigma(x)$ is the stress at a point located at x position, β^N is the strain rate-displacement rate transformation defined from the interpolation. $M^{NM}\ddot{u}^M$ is the force vector due to material inertia also known as d'Alembert forces which can be solved by dynamic equilibrium. The Equation (5.3) can be written as Equation (5.4) where KNM is the system's tangent stiffness/Jacobian matrix. The incremental displacements are updated by Equation (5.5). Iterations in each increment are repeated until the convergence is achieved i.e. at every node; force and moment equilibrium are obtained, contact conditions are satisfied and displacement corrections are small compared to incremental displacements. The benefit of implicit scheme is that it is unconditionally stable providing accurate solutions.

$$P^N - I^N = M^{NM}\ddot{u}^M \quad (5.1)$$

$$I^N = \int_V \beta^N : \sigma dV \quad (5.2)$$

Where; $\beta^N = \frac{[c]}{[u]^N}$

$$P^N - I^N + \left[\frac{\partial P^N}{\partial u^M} - \frac{\partial I^N}{\partial u^M} \right] C^M + \dots = 0 \quad (5.3)$$

$$P^N - I^N = K^{NM} c^M \quad (5.4)$$

Where; $K^{NM} = \frac{\partial P^N}{\partial u^M} - \frac{\partial I^N}{\partial u^M}$

$$\Delta u_{(i+1)}^N = \Delta u_{(i)}^N + \Delta t_{(i+1)} \Delta u_{(i+1)}^N \quad (5.5)$$

The solution cost for explicit scheme is approximately proportional to the model size whereas implicit scheme's solution cost increases steeply with the model size as shown in Figure 5.2. There are various factors that need to be considered before choosing solver for a given problem. If the priority is given to the computational time and storage space, explicit scheme seems to be the attractive choice. If obtaining accurate solution is important, Implicit scheme is chosen over the explicit scheme.

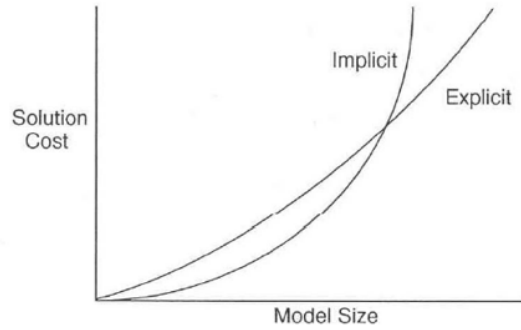


Figure 5.2: Comparison of Explicit and implicit Schemes

Based on the traits of two solution schemes, the implicit scheme seems more matched to the characteristics of the problem. For the present study, implicit dynamic method with Quasi-static option is used in 2-D lamination models (shown in Figure 5.1).

5.1. 2 Boundary Conditions, Loadings and Interactions

In reality, lamination process starts first by applying tension in each web before passing through the rollers which is also called as pretension. Nip rollers are brought close enough to contact one web with the other for lamination and then nip load is applied gradually as the webs are laminated in the nip contact zone. Then the rigid roller begin to rotate at an angular velocity, ω . After lamination process, web tension, roller angular velocity and nip load are brought to zero to observe the MD curl of the laminated web. To mimic the actual lamination condition, loading procedure is divided into six steps and appropriate boundary conditions and interaction properties are assigned in these steps. The six steps defined in the model are: Pretension, NipOn-Dummy, NiploadOn, TensionOnWebLeft, Webmove and ReleaseLoads. In boundary conditions, U_1 , U_2 and U_3 are defined as the degree of freedom in X-direction, Y-direction and Z-direction respectively; UR_1 , UR_2 and UR_3 are defined as rotational degree of freedom in X-direction, Y-direction and Z-direction respectively. Boundary conditions are assigned on the web right and left end surfaces, reference point of top roller, bottom roller and rigid block as shown in Figure 5.3. Loading conditions as well are shown in the Figure 5.3.

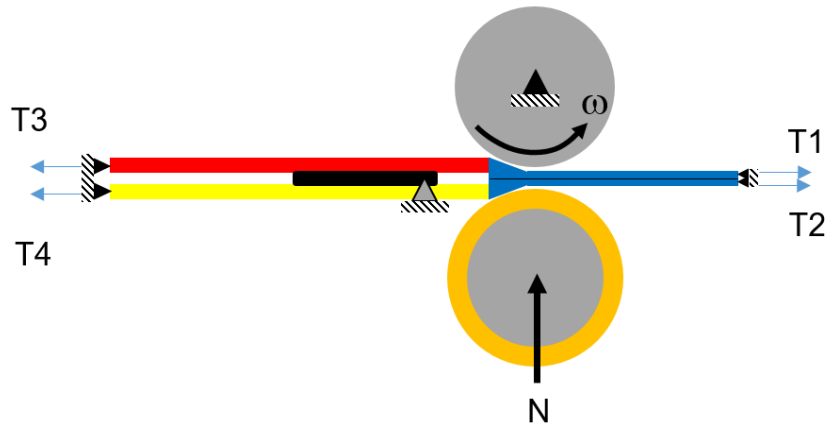


Figure 5.3: Model with loading and boundary conditions

The six steps are explained in details with corresponding boundary and loading

conditions as shown below:

- **Step-1-Pretension:** Webs on the right side of the nip set is subjected to tension.
 - **Boundary conditions:** U_2 of the web right surface is set free.
 - **Loading conditions:** Tension, T_1 and T_2 are applied.

- **Step-2-NipOnDummy:** The nip rollers are brought close such that there is no gap between the webs.
 - **Boundary conditions:** Set $U_2 = -0.127$ mm and $+0.127$ mm for the top roller and bottom roller respectively.
 - **Loading conditions:** No load is applied in this step.

- **Step-3-NiploadOn:** Load is applied on the rubber covered roller which acts as pressure for laminating webs.
 - **Boundary conditions:** U_2 of the bottom roller is set free.
 - **Loading conditions:** Force of magnitude N is applied on the rubber covered roller.

- **Step-4-TensionOnWebLeft:** Tension is applied on the left surface of the web.
 - **Boundary conditions:** U_2 of the web left surface is set free.
 - **Loading conditions:** Tension, T_3 and T_4 are applied.

- **Step-5-Webmove:** Web starts moving forward by rotating the rigid roller. At the end of the step, roller velocity is brought to zero.
 - **Boundary conditions:** Set UR_3 of the rigid roller free.
 - **Loading conditions:** Angular velocity, VR_3 is applied.

■ **Step-6-ReleaseLoads:** All the loads are released to access the MD curl of the laminated web. These loads are brought to zero smoothly step-by-step to avoid any dynamic instability.

□ **Boundary conditions:** No change from previous step.

□ **Loading conditions:** $N = 0$; $T_1 = T_2 = T_3 = T_4 = 0$.

The amplitude graph for loading and boundary conditions in each step is shown in Figure 5.4 briefly. Top graph represents the amplitude for boundary condition and bottom one represents the amplitude for loading.

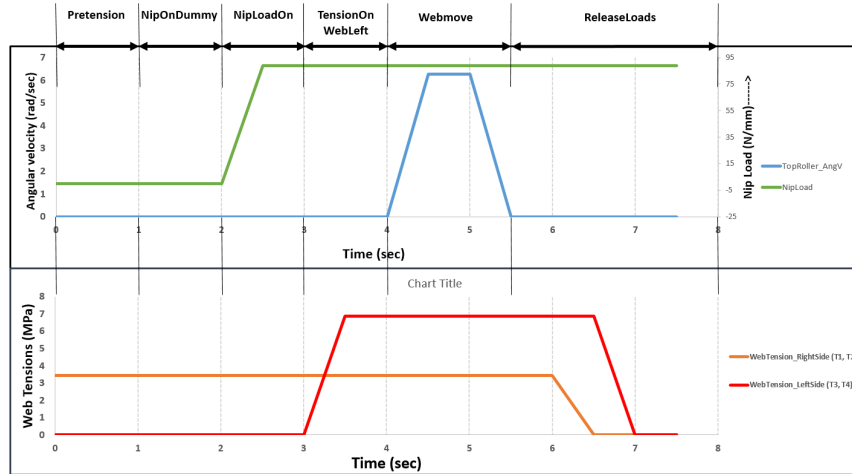


Figure 5.4: Amplitude graph for loads and boundary conditions for every step

The contacts in the model are defined based on the material involved in a contact. The contact between the top/bottom rollers with the corresponding web in contact is modeled by a penalty contact pair algorithm assigning a coefficient of friction value. In case of model-I&II, the contact between the rigid block and webs is defined by frictionless formulation and allowing separation after contact whereas in model-III, the same algorithm is applied for the contact of webs with idle rollers. Frictionless formulation and no separation after contact algorithm is defined for the web-to-web interaction. A Coulomb friction model is employed that relates the maximum al-

lowable frictional (shear) stress across an interface to the contact pressure between the contacting bodies. In basic Coulomb friction model, two contacting surfaces can reach shear stresses up to a certain magnitude across their interface prior to slipping relative to one another, in a state known as stick. The coulomb friction model defines this critical shear stress (τ_{crit}) as the stress at which sliding of the surfaces starts as a fraction of the contact pressure ($p(x)$) between the surfaces as shown in Equation (5.6).

$$\begin{aligned} \tau_{crit} &= \mu P(x) \rightarrow Slip \\ \tau_{crit} &< \mu P(x) \rightarrow Stick \end{aligned} \tag{5.6}$$

The stick/slip calculation determines when a point in contact region moves from stick to slip or slip to stick. This friction law is basic and is sometimes criticized due to the critical shear stress being independent of the magnitude of the slip velocity as shown in Figure 5.5. This friction model is used in these simulations more often.

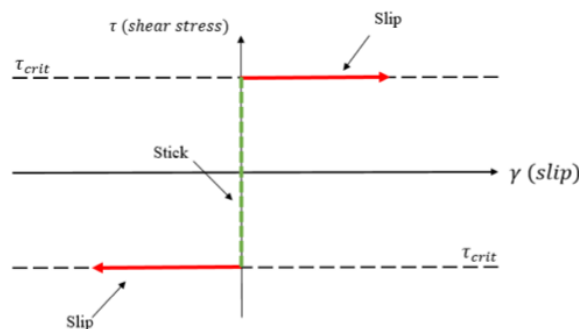


Figure 5.5: Coulomb's Friction Model

5.1. 3 Mesh and Elements

Abaqus has a family of quadrilateral elements for modeling plane problems. Four-node isoparametric elements are used. A numerical deficiency called “shear locking” occurs if quadrilateral elements are used which fully integrate for stiffness. This

Table 5.2: Mesh Element Size

Mesh Part	Element Size (mm)
Rubber Cover	0.508×0.508
Web	0.508×0.00635

causes elements to be very stiff if subjected to bending and thus affects the accuracy. Therefore, quadrilateral elements using first order reduced integration are used since it eliminates the shear locking effect. However, these elements may introduce another deficiency called “the hourglass mode” where the elements are free to deform without consuming any energy. This deformation pattern may easily propagate through the whole mesh region and can have large effects on the accuracy. So, finer mesh and multiple elements through thickness need to be used to solve this problem. In this work, CPE4R plain strain elements are used. The mesh size as shown in Table 5.2 is used in these simulations.

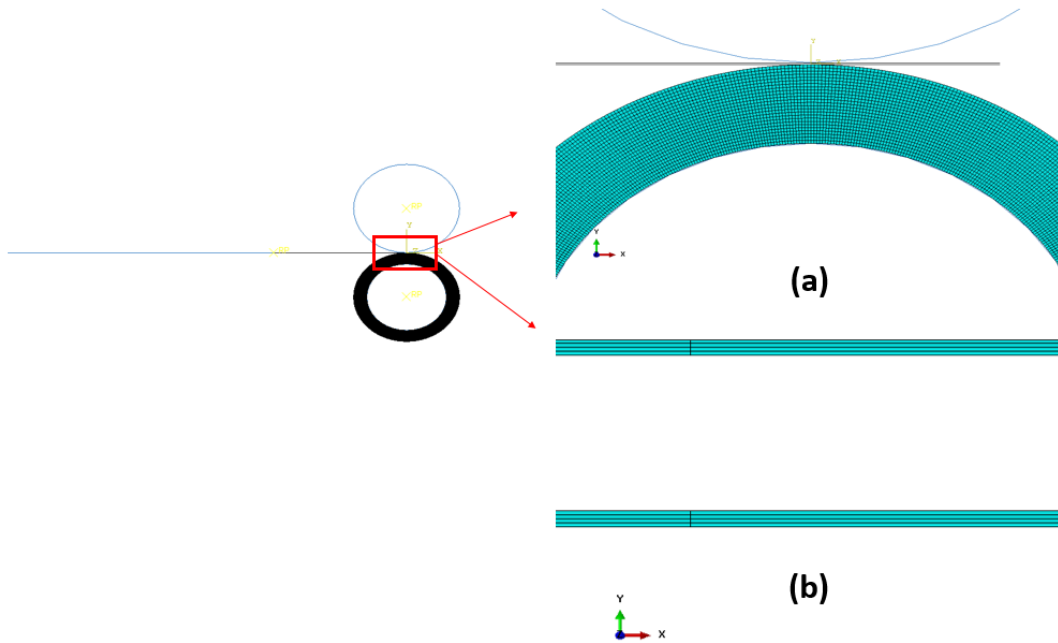


Figure 5.6: Mesh for the lamination model (a) For rubber covered roller; (b) For the webs

5.1. 4 Theoretical MD curl radius calculation for model-I and defining the curl directions

In model-I (Figure 5.1(a)), there is no nip load and rubber covered roller and so MD curl is expected to be dependent on the strains in the webs just before entering the nip set. Here, the strain is calculated from the applied tensions on the webs and so it can be said that the MD curls depend on tensions in each web just before lamination. Since there is no nip load applied on the rollers, “NipLoadOn” step is removed in the Finite Element simulations. Theoretically, MD curls can be calculated based on laminate theory explained by Kidane [41] or using bending beam theory (as shown in Equation (5.7)). A pictorial representation of laminated web considered for calculation of MD curl based on bending beam theory is shown in Figure 5.7.

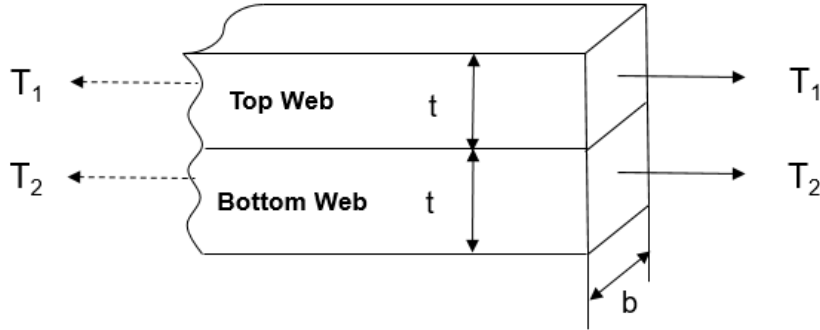


Figure 5.7: Pictorial representation of the laminated web

$$\rho = \frac{EI}{M} \quad (5.7)$$

Where; $I = \frac{bt^3}{12}$ and $M = (T_1 - T_2) \times t \times \frac{t}{2}$

Here, E is the Young’s modulus of the web; I is the moment of inertia; b and t are width and thickness of the webs and M is the bending moment. For different web tensions, Finite Element simulations were conducted. Web that is laminated during “web move” step is considered for calculation of MD curl radius. Using MATLAB

code, the MD curl radius is calculated using the concept of obtaining radius of circle from given three points (Please look into Appendix A for further details). For all the laminated models, the MD curls can be found bending towards either bottom roller or top roller depending on the tension in the web and so they are differentiated by sign as shown in Figure 5.8. The curl that is bending towards bottom roller is considered as "Positive curl radius" and the curl that is bending towards top roller is considered as "negative curl radius".

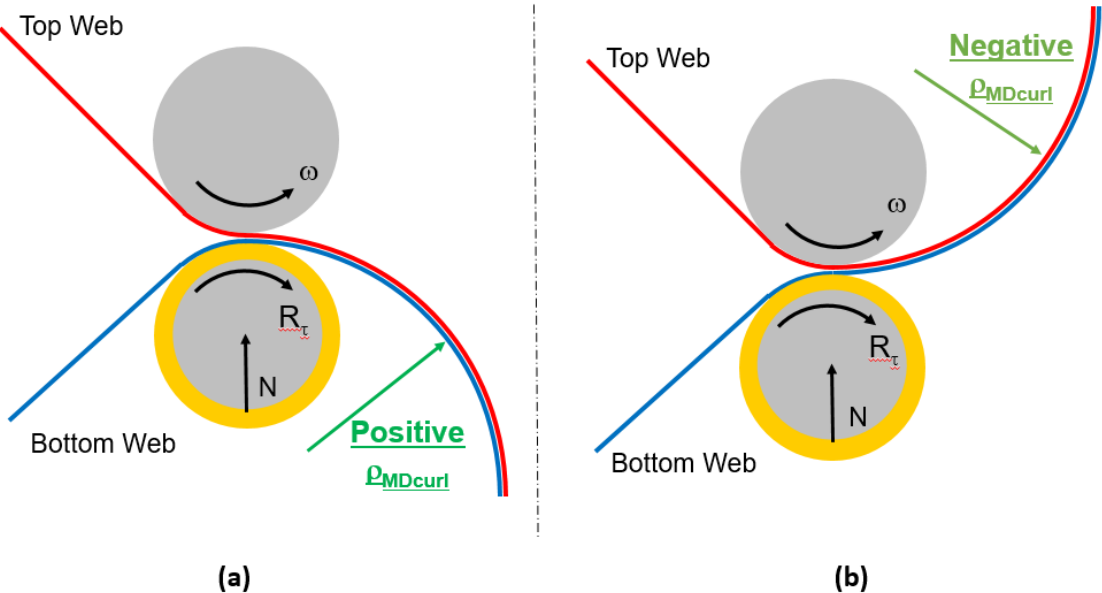


Figure 5.8: Sign for MD curl radius, (a) Positive Curl; (b) Negative Curl

5.2 Results and Discussions

5.2.1 Results for the lamination between two rigid rollers with webs entering straight (Model-I)

For model-I lamination model, simulation were performed for different web tension inputs to access their MD curl radius. For the same web inputs, the MD curl radius

was theoretically calculated using Equation (5.7). Figure 5.9 represents the MD curl radius for model-I obtained from both Finite Element simulations and calculated results. In the graph, the T_{diff} in the X-axis is $T_1 - T_2$ (T_1 and T_2 are defined in Figure 5.7). The values of T_1 and T_2 that produces T_{diff} in the Figure 5.9 is shown in Table 5.3. From the Figure 5.9, it is clear that the simulated results are well matched with the calculated values.

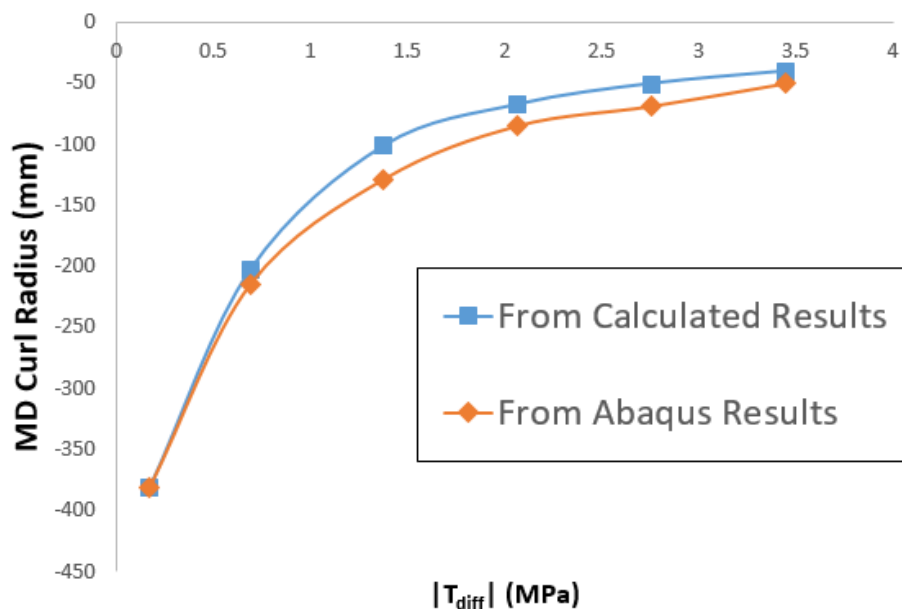


Figure 5.9: MD Curl radius for Model-I

Table 5.3: T_1 and T_2 values for Model-I results

T_1 (MPa)	T_2 (MPa)	T_{diff} (MPa)
3.45	3.45	0
4.14	3.45	0.69
4.83	3.45	1.38
5.52	3.45	2.07
6.21	3.45	2.76
6.89	3.45	3.45

Two cases were considered where T_{diff} is 2.07 MPa and -2.07 MPa as shown

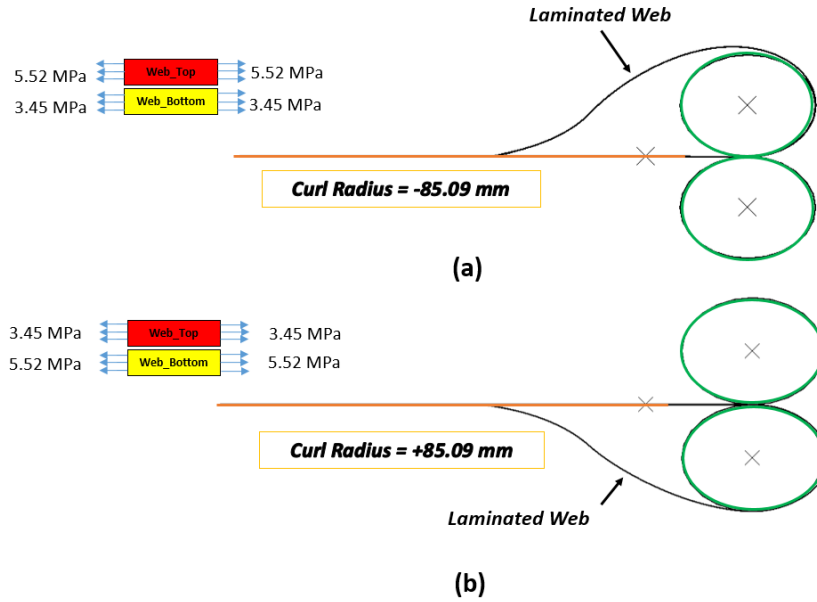


Figure 5.10: MD Curl radius for case(a) $T_{diff}=2.07$ MPa; (b) $T_{diff}=-2.07$ MPa

in Figure 5.10. The MD curl radius value remains to be constant since they have same values of T_{diff} but the curl is bent towards top roller for the case $T_{diff}=2.07$ MPa (Figure 5.10(a)) and towards bottom roller for the case $T_{diff}=-2.07$ MPa (Figure 5.10(b)). It is clear that the curl direction depends on the tension in the webs just before lamination.

With the obtained results in this section, it can be said that the developed lamination model shows the promising results in accessing the curl.

5.2. 2 Results for the lamination between a rigid and rubber covered roller with webs entering straight (model-II)

The Rubber cover is introduced on the lower of the nip rollers in the model-II (Figure 5.1(b)) with a nip load applied on it. In addition to web tensions, additional parameters that are affected by rubber cover can impact the MD curl radius. Finite Element Simulations were performed for different nip loads and web tensions. For model-II,

the tensions are applied on the web as shown in the Figure 5.11. Here, T_{diff} is $T_1 - T_2$. Table 5.4 & 5.5 shows the MD curl radius for different T_{diff} and Nip loads, N.

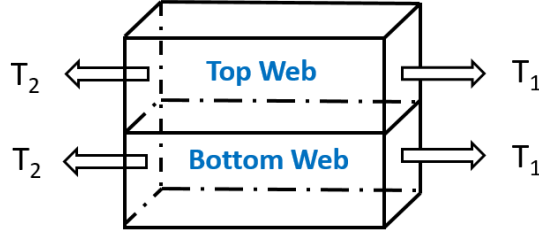


Figure 5.11: Tension applied on webs for Model-II

From Table 5.4, the MD curl radius for case-1 & 2 has closely same values. For both cases, the tension difference between top and bottom web is zero and so the curls with almost same radius are seen. For case-3 & 4, the Tension difference between top and bottom web is 2.76 MPa & -2.76 MPa respectively and so it's curl radius value is changed from the previous cases. Compared with the other cases, the direction of curl is changed for Case-3. From case-3 and case-4, it is clear that the direction of curl depends on the tension in the individual web just before lamination and also on web which is closest to the rubber covered roller at a given tension. Figure 5.12 & 5.13 shows the MD curl of laminated web for cases-2 & 3 respectively.

Table 5.4: MD Curl radius for different T_{diff}

Case	Web Tensions, T_{diff} (MPa)	MD Curl Radius (mm)
Case-1	$3.45 \leftarrow$ Top_Web $\rightarrow 3.45$ $3.45 \leftarrow$ Bottom_Web $\rightarrow 3.45$	42.65
Case-2	$0.69 \leftarrow$ Top_Web $\rightarrow 0.69$ $0.69 \leftarrow$ Bottom_Web $\rightarrow 0.69$	38.99
Case-3	$0.69 \leftarrow$ Top_Web $\rightarrow 0.69$ $3.45 \leftarrow$ Bottom_Web $\rightarrow 3.45$	-61.16
Case-4	$3.45 \leftarrow$ Top_Web $\rightarrow 3.45$ $0.69 \leftarrow$ Bottom_Web $\rightarrow 0.69$	21.01

For the case-1 from Table 5.4, Finite Element simulations were performed for different nip loads. Table 5.5 shows the MD curl radius for the laminated web for

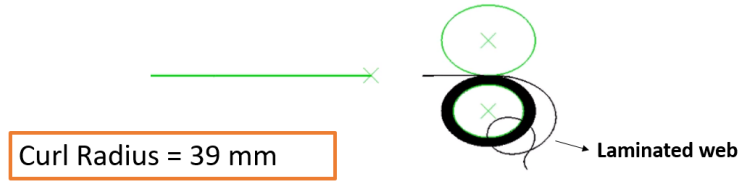


Figure 5.12: MD Curl Radius for Case-2



Figure 5.13: MD Curl Radius for Case-3

Table 5.5: MD Curl radius for different Nip loads

Nip Load (N/mm)	MD Curl Radius (mm)
44.48	48.21
53.38	28.804
66.72	37.516

different nip load conditions. For all the nip loads shown in Table 5.5, curl radius remains almost constant. It shows that the nip load doesn't impact on the MD curl radius greatly. Generally, the lamination machine used in the Industry shows an impact of the nip load on the MD curl radius.

5.2.3 Results for the lamination between a rigid and rubber covered roller with webs entering at wrap angle, θ (Model-III)

In model-III (Figure 5.1(c)), webs enter at different wrap angle, θ to the nip rollers for lamination. For three wrap angles *i.e.* $\theta = 0^0, 45^0$ & 90^0 as shown in Figure 5.14, simulations were conducted with two different tensions (Figure 5.15) in the web. For $T_{diff} = 3.45$ & 0.69 MPa, MD curl radius for the three wrap angles, θ are plotted as shown in the Figure 5.16. In the X-axis of the plot, membrane strain (ϵ_1, ϵ_2) of the

top and bottom web at the entry to nip roller is considered.

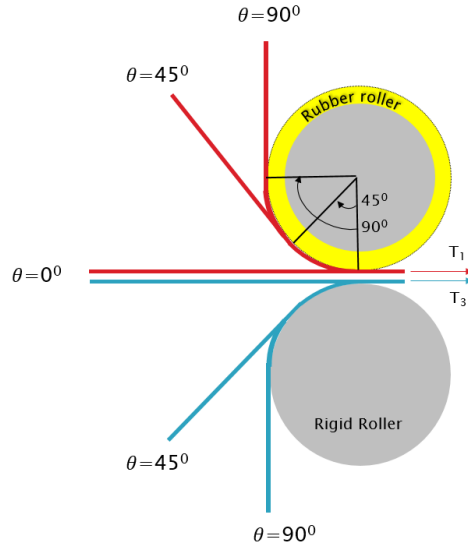


Figure 5.14: Defining wrap angle, θ for model-III



Figure 5.15: Cases with two different web tensions, For (a) $T_{diff} = 3.45 \text{ MPa}$; (b) $T_{diff} = 0.69 \text{ MPa}$

With increase wrap angle, more web gets in contact with the rubber covered roller as shown in Figure 5.14 subjecting the web to additional bending strain. With the increased strains in the webs before lamination, the MD curls are expected to decrease. Therefore, with increase of wrap angle the curls are expected to minimize. For $T_{diff} = 0.69 \text{ MPa}$, the curl radius is reduced as wrap angle increased from 45° to 90° . Whereas for $T_{diff} = 3.45 \text{ MPa}$, the curl radius kept increasing with increase of wrap angle which is opposite to the statement mentioned above.

With the constraint used between the webs i.e. webs getting locked once got into contact, the behavior of webs after releasing web tension does not seem to consider

the effect of adhesive layer for the curl and thus the effect of wrap angle is varied for different web tension inputs.

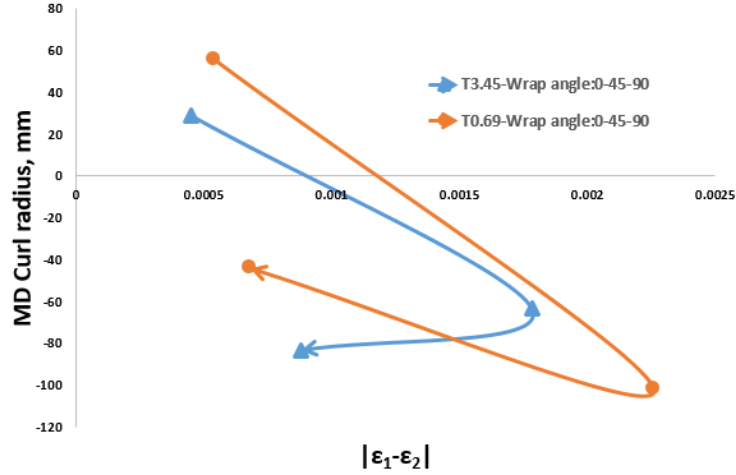


Figure 5.16: Cases with two different web tensions, T_{diff}

Here, Model-II & III shows the impact of tensions in the webs and wrap angle of the web on the final MD curl of laminated web. There are few parameters such as nip load effect for model-II, influence of wrap angle in model-III are not completely captured due to the contact algorithm used at the interaction of the webs. Introducing an adhesive layer in between the webs during lamination would give an approximate MD curl radius considering all the influencing parameters. Next chapter talks about the characterization of adhesive and implementing the adhesive layer in Finite Element Simulations.

CHAPTER VI

MODEL OF LAMINATION WITH ADHESIVES

In Chapter V, FE models for the lamination of the webs without considering adhesive layer in between the laminated web were seen. To mimic the actual lamination process, it is necessary to characterize the adhesives. In this Chapter, experimental study on the characterization of lamination adhesives is conducted and Finite Element simulations are performed using material properties of Adhesives obtained from experiments.

6.1 Viscoelastic characterization of laminate adhesives

For characterization of laminate adhesives, experiments were performed to characterize the viscoelastic properties. Generally, creep and stress relaxation test are the two standard test methods to characterize the viscoelasticity of a material. For the present study, a stress relaxation test was performed. In stress relaxation tests, a constant uniaxial strain (ϵ) is applied quasi-statically to avoid any dynamic effects on a specimen for a particular duration as shown in Figure 6.1. Equation (6.1) shows the calculation of strain, ϵ . The resulting stress as a function of time is measured. The stress needed to maintain the strain constant decreases gradually and reaches a constant value as shown in Figure 6.2. Relaxation modulus, $E(t)$ and instantaneous modulus, E_0 can be calculated using Equation (6.2).

$$\epsilon = \frac{\Delta L}{L} \quad (6.1)$$

Here, L is the length of specimen and ΔL is the change in length due to applied load.

$$E(t) = \frac{\sigma(t)}{\epsilon_0} \quad (6.2)$$

$$E_0 = \frac{\sigma(t=0)}{\epsilon_0}$$

Here, $\sigma(t)$ is the stress as a function of time; ϵ_0 is the constant strain that is maintained during test; $\sigma(t=0)$ is the initial stress at the start of stress i.e. at $t=0$

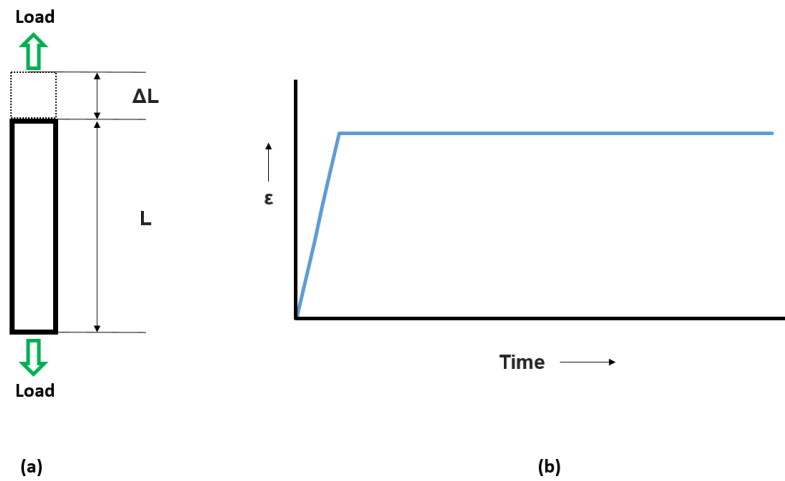


Figure 6.1: (a) Specimen subjected to loading; (b) Applied strain Vs. time

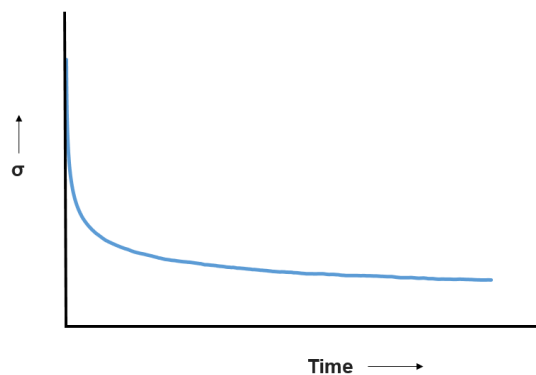


Figure 6.2: Effect of Stress relaxation test i.e. resulting stress Vs. time

The stress relaxation test is conducted for the double lap adhesive joint specimen on a RSA-G2 DMA machine (TA instruments) as shown in Figure 6.3. Uni-axial tensile displacement is applied on the specimen i.e. on the web part as shown in Figure 6.4 for a constant displacement, ΔL . Since adhesive is the area of interest for obtaining viscoelastic properties, shear stresses, τ acting on the adhesive as shown in Figure 6.5 are considered for the calculation of the shear relaxation modulus, $G(t)$. Load acting on the adhesive, $P(t)$ for the applied displacement, ΔL are recorded during the experiment to calculate shear stress, τ and shear strain, γ respectively using Equation (6.3). Relaxation shear modulus, $G(t)$ and instantaneous shear modulus, G_0 are calculated by Equation (6.4).

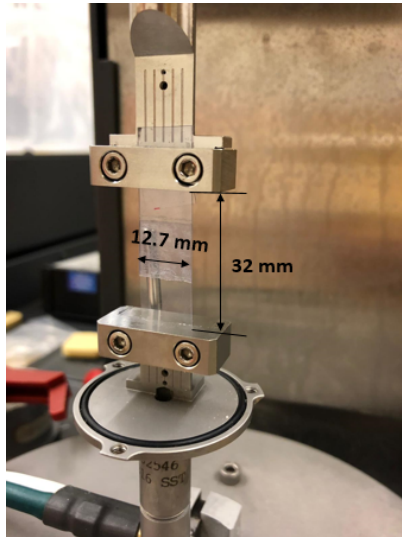


Figure 6.3: Stress Relaxation Test on RSA-G2 machine

$$\tau(t) = \frac{P(t)}{A} = \frac{P(t)}{2WL_J} \quad (6.3)$$

$$\gamma = \frac{\Delta L}{t_a}$$

Here, A is the cross-sectional area of adhesive on which τ acts; W is the width of specimen = 11.94 mm; L_J is the length of joint/Adhesive = 12.7 mm; t_a is the thickness of the adhesive = 0.051 mm and ΔL is the constant input displacement = 0.152 mm. The material used for the specimen are: 3M987 transfer tape (3M Company, St.

Paul, MN) for the adhesive part and a polyester web of 0.043 mm and the modulus is approximates 4136.85 MPa.

$$G(t) = \frac{\tau(t)}{\gamma}$$

$$G_0 = \frac{\tau(t=0)}{\gamma} \tag{6.4}$$

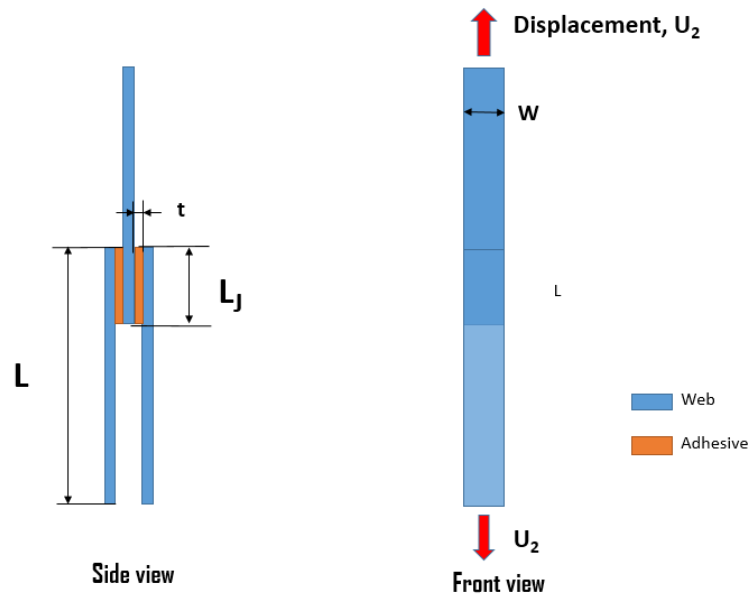


Figure 6.4: Geometry of the Double lap Adhesive joint

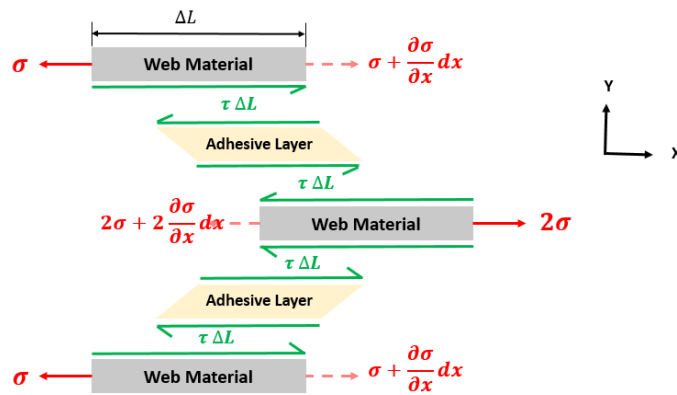


Figure 6.5: Force balance for the specimen used in Stress relaxation test

The test is performed for the duration of 10 minutes at room temperature. The

calculated shear modulus as a function of time, $G(t)$ is shown in the Figure 6.6. Here, two web materials are used for the specimen *i.e.* polyester web (web-1) and light weight coated web (web-2). The test is repeated four times (two tests with web-1 and other two tests with web-2) and the repeatability of the test is good. Therefore, the test values are considered to be valid. From Figure 6.6, the Shear modulus is decreased exponentially with time and maintained almost constant after 6 minutes.

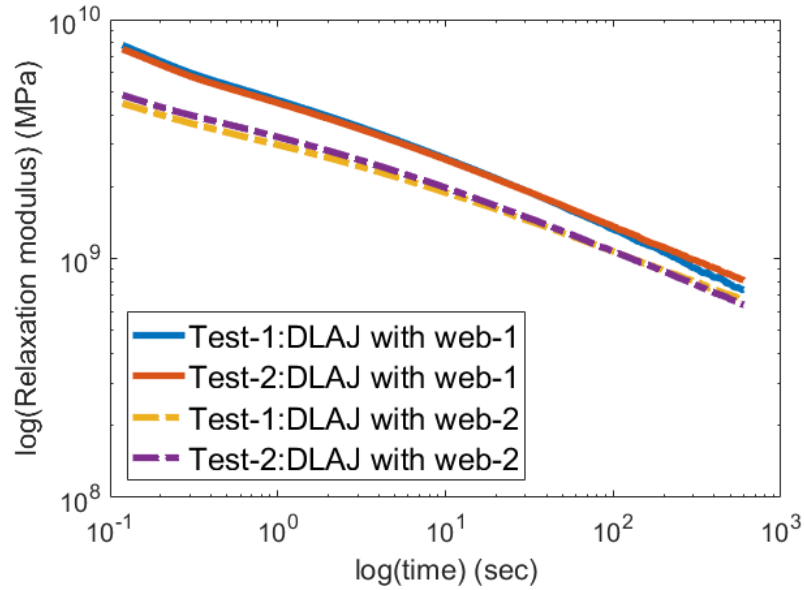


Figure 6.6: Relaxation Modulus as a function of time

To make sure that the obtained results in Figure 6.6 belong to the adhesive, a stress relaxation test is conducted on the web alone of same length L for two web materials and compared with the double-lap adhesive joints for the corresponding web materials as shown in Figure 6.7. For the double-lap adhesive joints, the modulus values initially showed a slight difference and then slowly converged to same values by the end of the test. For the webs alone, the modulus values are shown to be entirely different. From this, it can be concluded that the modulus values belong to the adhesive alone.

The data from the experiment can be used to define a model which can be used

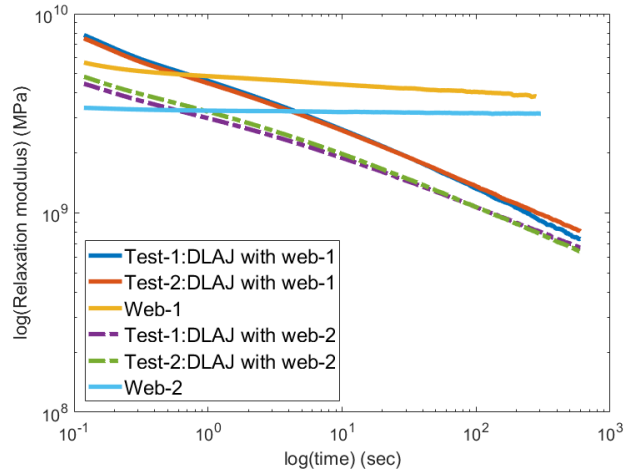


Figure 6.7: Relaxation modulus as a function of time

to represent material property of Adhesive in Finite Element analysis. Wiechert's model, also known as Generalized Maxwell Model can be used to represent the viscoelastic response of the adhesive material. In this model, several Maxwell elements are assembled in parallel as shown in Figure 6.8.

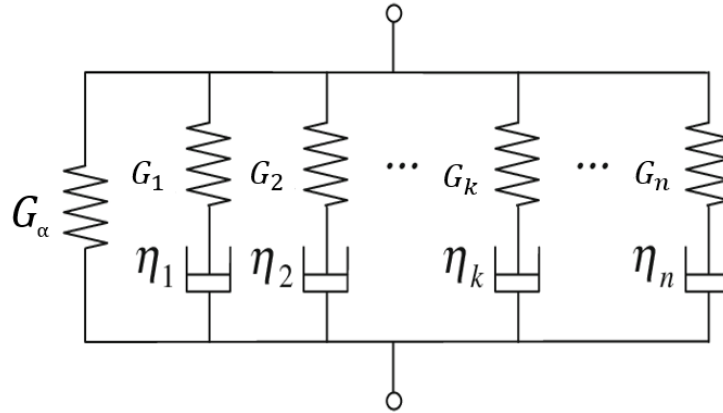


Figure 6.8: Generalized Maxwell Model

Where E_∞ is the equilibrium modulus. For this model, The stress, σ and strain, ϵ can be written as shown in Equation (6.5) & (6.6).

$$\epsilon = \epsilon_\infty = \epsilon_k \tag{6.5}$$

$$\sigma = \sigma_{\infty} + \sum_{k=1}^n \sigma_K \quad (6.6)$$

The relaxation time constant of element k can be defined as $\tau_k = \frac{\eta_k}{E_k}$. Therefore, the Maxwell constitutive law for one element k can be written as:

$$G_k \dot{\epsilon}_k = \dot{\sigma}_k + \frac{\sigma_k}{\tau_k} \quad (6.7)$$

Using an integration factor, e^{t/τ_k} in Equation (6.7), stress for an element k can be written as:

$$\sigma_k = \int_{-\infty}^t G_k e^{-(t-s)/\tau_k} \frac{d\epsilon}{ds} ds \quad (6.8)$$

For the Generalized Maxwell model, $\sigma(t)$ can be defined by substituting Equation (6.8) into Equation (6.6).

$$\begin{aligned} \sigma(t) &= \int_{-\infty}^t \left(G_{\infty} + \sum_{k=1}^N G_k e^{-(t-s)/\tau_k} \right) \frac{d\epsilon}{ds} ds \\ &= \int_{-\infty}^t \left(G_0 - \sum_{k=1}^N G_k [1 - e^{-(t-s)/\tau_k}] \right) \frac{d\epsilon}{ds} ds \\ &= \int_{-\infty}^t G(t-s) \frac{d\epsilon}{ds} ds \end{aligned} \quad (6.9)$$

where $G(t-s)$ is shear relaxation modulus. Therefore, relaxation modulus for the model can be rewritten as:

$$G(t) = G_0 - \sum_{k=1}^N G_k (1 - e^{-t/\tau_k}) \quad (6.10)$$

Here, G_0 is instantaneous shear modulus which can be calculated from Equation (6.2).

The input parameters required to define viscoelastic property of the Adhesive in Abaqus are: Instantaneous Modulus, E_0 which is calculated by Equation (6.11);

Poisson's ratio, ν ; prony series, g_k and τ_k . Here, g_k is the ratio of corresponding element modulus to the instantaneous modulus i.e. $\frac{G_k}{G_0}$.

$$E_0 = 2G_0(1 + \nu) \tag{6.11}$$

By curve fitting the Experiment values of $G(t)$ from Figure 6.6, prony series can be obtained. Here, three Maxwell elements are used for curve fitting and Table 6.1 shows the values of the obtained prony series. Figure 6.9 shows the $G(t)$ values from the experiment and Generalized Maxwell Model.

Table 6.1: Prony Series for the Model

g_k	$\tau_k, \text{seconds}$
0.4158	0.412
0.2788	5.279
0.1961	80.063

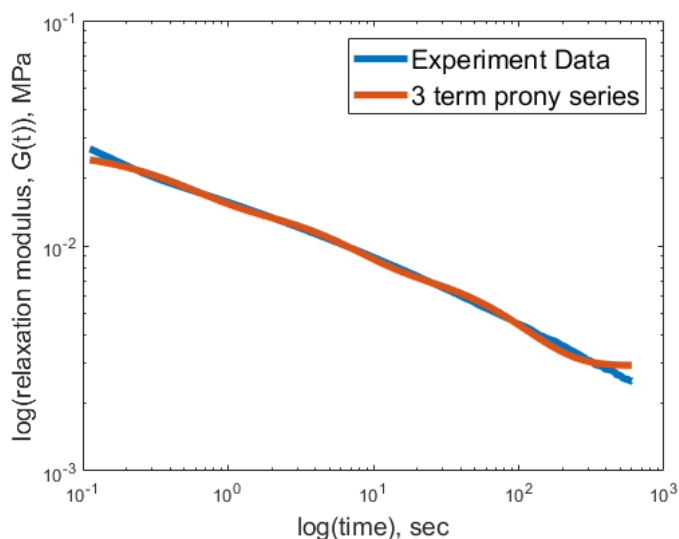


Figure 6.9: Curve fitting for Relaxation Shear modulus, $G(t)$

For Abaqus viscoelastic material property, additional term bulk modulus ratio, " k_k " for the corresponding prony series is required. Here, k_k is the ratio of instantaneous

bulk modulus to corresponding element bulk modulus i.e. $\frac{K_k}{K_0}$. The bulk Modulus can be calculated from Equation (6.12).

$$K = \frac{3G(1 + \nu)}{2(1 - 2\nu)} \quad (6.12)$$

The bulk modulus ratio, k_k ;

$$k_k = \frac{K_k}{K_0} = \frac{\frac{3G_k(1+\nu)}{2(1-2\nu)}}{\frac{3G_0(1+\nu)}{2(1-2\nu)}} = \frac{G_k}{G_0} \quad (6.13)$$

$$\Rightarrow k_k = g_k$$

Therefore, the obtained input parameters of the Adhesive materials properties for Abaqus are shown in Table 6.2.

Table 6.2: Material properties of Adhesive as input for Abaqus

Elastic	$E_0=0.7$ MPa and $\nu = 0.3$		
Viscoelastic	g_k prony	k_k prony	τ_k prony
	0.4158	0.4158	0.412 s
	0.2788	0.2788	5.279 s
	0.1961	0.1961	80.063 s

6.2 Numerical Model of Lamination with Adhesive layer

Lamination of webs with an adhesive layer of 0.04318 mm thickness in between is modelled in this section. This lamination model is labelled "Model-IV" as shown in Figure 6.10. The boundary conditions and amplitudes of loading conditions are similar to the previous models (Refer to Figures 5.3 & 5.4). In this model, the adhesive layer is attached to the top web initially and laminates with the bottom web at nip

contact zone. The material properties of the adhesive layer are defined in the previous section (Table 6.2).

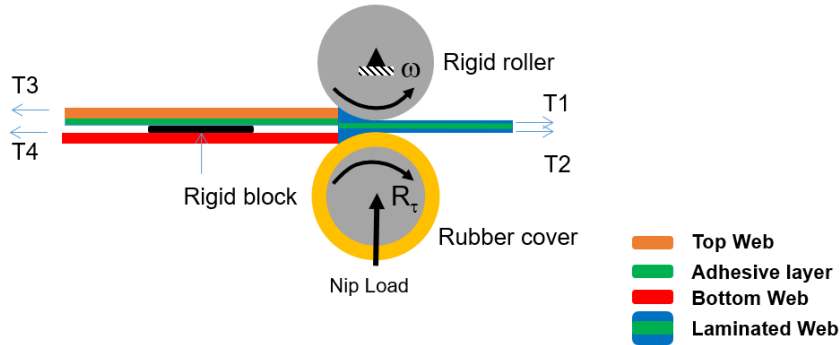


Figure 6.10: Model setup in Abaqus for Model-IV

In Figure 6.10, ω represents the angular velocity of the rigid roller; R_τ represents the torque applied to the rubber covered roller; T_1, T_2, T_3 and T_4 represent the tensions applied on the webs. Initially, simulations were conducted for zero torque applied on the rubber covered roller to study the effect of the adhesive's viscoelasticity. For the present analysis, the loads applied for the model-IV are shown in Table 6.3.

Table 6.3: Loading conditions for Model-IV

S. No.	Input Loads	Values
1	Web Tensions	
2	Nip Load, N	44.48 N/mm
3	Angular Velocity, ω	6.28 rad/sec
4	Torque input, R_τ	0 N-mm

6.3 Results for the lamination process with a laminate adhesive

Shear strain, γ of the adhesive layer in nip contact zone is plotted in Figure 6.12 during lamination process. From the graph, the shear strain of adhesive layer causes webs to

shear even after lamination which impacts on the MD curl at the end of lamination. Whereas in models- II & III, webs are stuck together once laminated i.e. no shear at the interaction of the webs in the laminated web. Thus, different MD curls are witnessed for the lamination model without an adhesive layer (Model-II) & with an adhesive layer (Model-IV) as shown in Figure 6.11.

Model-II: Without an adhesive layer

Model-IV: With an adhesive layer



Figure 6.11: MD curl in the laminated web for (a) Model-II; (b) Model-IV

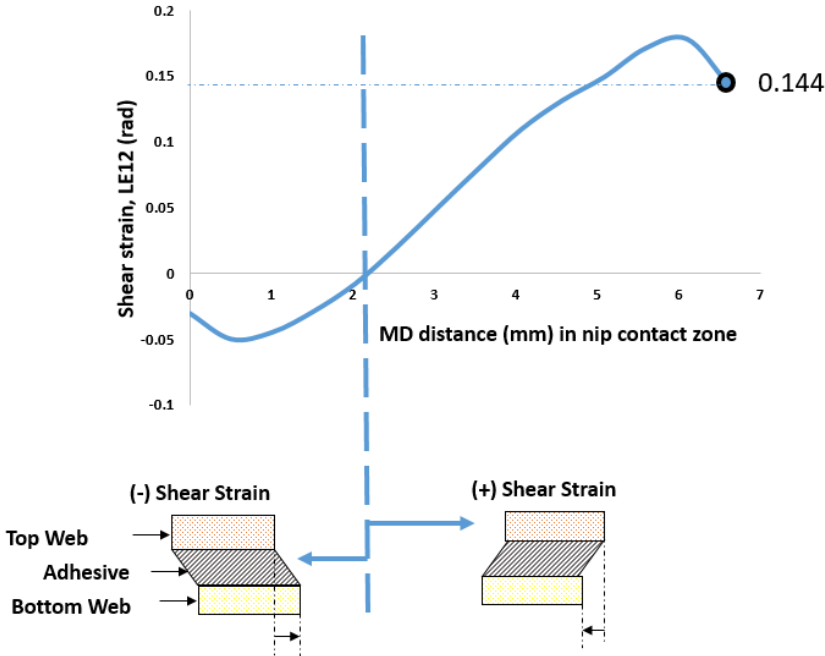


Figure 6.12: Shear Strain in the Adhesive Layer at Nip Contact Zone

Slip and stick status of the laminated web in nip contact zone can be estimated by

using Coulomb's Friction Model (explained in section 5.2). According to Coulomb's model, slip happens when $\tau_{crit} = \mu P(x)$ and stick happens when $\tau_{crit} < \mu P(x)$. Figure 6.13 shows the contact status for bottom and top web in nip contact zone. From the figure, a small portion of slip is observed for top web at the end of nip contact zone and the bottom web is sticking to the rubber covered roller in nip contact zone.

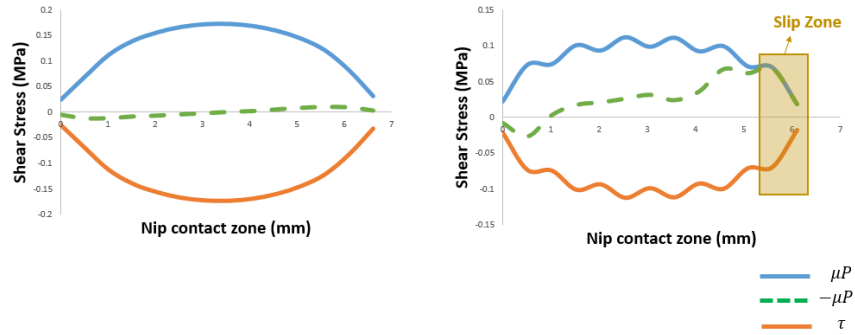


Figure 6.13: Contact Status at Nip Contact Zone for (a) Bottom Web; (b) Top Web

6.3. 1 Effect of viscoelastic properties of laminate adhesive on MD curl radius

From Table 6.2, the meaning for the first prony series (g_1, τ_1) is that the laminate adhesive takes longer than 0.412 seconds to relax 41.58 % of the modulus. The relaxation time constant, τ_1 is the most important term which decides if the impact of viscoelasticity on MD curl is present or not. From the simulation results, it is seen that the time spent by the webs in the nip contact zone, t_{web} is 0.01 seconds. The viscoelastic part of adhesive effects the final MD curl of laminated web if τ_1 is less than t_{web} . Here, the effect of viscoelasticity of adhesive layer on MD curl of laminated web can studied by conducting computations for either different Relaxation times, τ_1 , or angular velocities ω that gives $t_{web} > \tau_1$.

6.3. 1.1 Study of viscoelastic effect for different relaxation times, τ_1

Table 6.4 shows the cases with different τ_1 and their final MD curl radius values for the loading conditions shown in Table 6.3. For the case-iii, τ_1 value is chosen that is $1/10^{th}$ of the t_{web} such that the laminate adhesive relaxes in the nip contact zone.

Table 6.4: MD Curl radius for different τ_1 values

Case#	τ_1 values (sec)	MD Curl Radius (mm)
Case-i	0.412	228.85
case-ii	No viscoelastic part i.e. only Elastic	255.52
case-iii	0.001	123.03

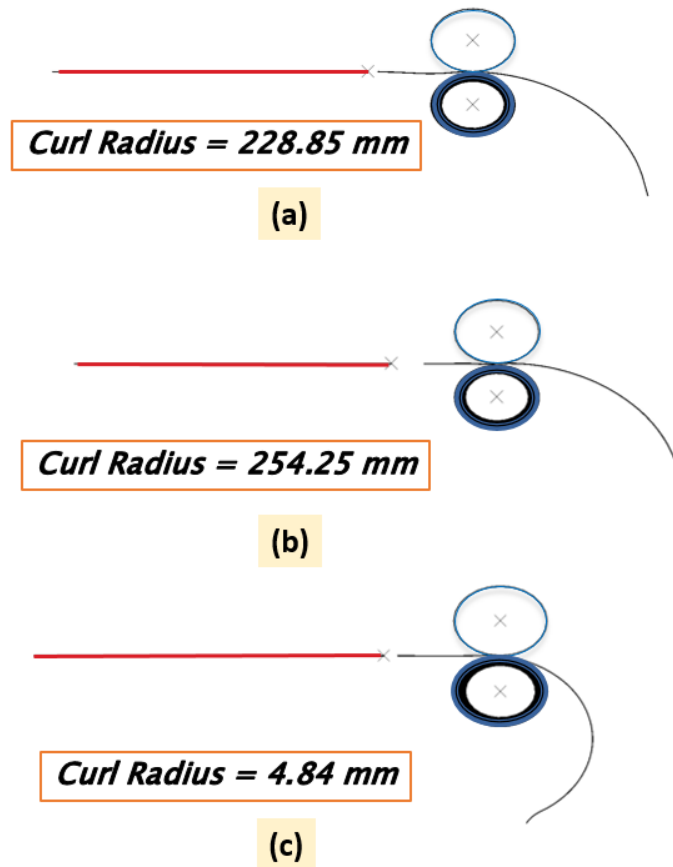


Figure 6.14: Final MD curl Radius of laminated web for (a) Case-i; (b) Case-ii; (c) Case-iii

From Table 6.4, the MD curl radius of the laminated web is almost constant

for case-i and ii. These are the cases where their relaxation time constant is greater than t_{web} i.e. $\tau_1 > 0.01$ sec and the laminate adhesives did not have enough time to relax during the lamination. For case-iii, the MD curl radius of the laminated web is reduced compared to other cases because it had enough time to relax in the nip contact zone i.e. $\tau_1 < 0.01$ sec. The viscoelastic properties of the laminate adhesive were active during lamination which effected the shear deformation during and after lamination resulting in the decrease of MD curl radius for case-iii. Figure 6.14 shows the images of laminated web with curl at the end of simulation for the corresponding cases. From Figure 6.14 (a)&(b), it can be seen that the adhesive can be considered elastic if first time constant was large compared to the time spent by the webs in the nip contact zone.

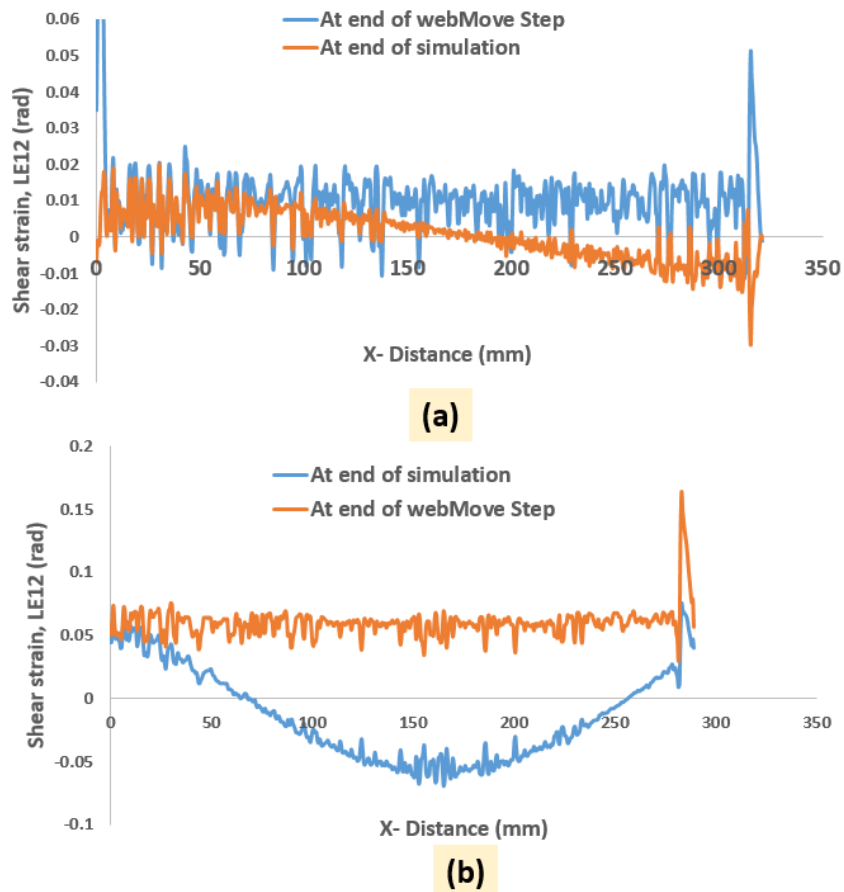


Figure 6.15: Shear strain of the adhesive layer for (a) Case-i;(b) Case-iii

It should be noted that the relaxation times affect shear deformations during laminating as well as the final step of the simulation where the web tension is removed to assess the MD Curl radius. The shear strain of the adhesive layer at the end of simulation is varied for the cases-i & iii which caused to result in different MD curls as shown in Figure 6.14. Figure 6.15 shows the shear strain of the adhesive layer at the end of web move step and last step. It is interesting to observe the shape of shear strain at the end of simulation is similar to the shape of final MD curl.

6.3. 1.2 Study of viscoelastic effect for different angular velocities, ω

By lowering the angular velocity of rigid/backup roller, the time spent by the web in nip contact zone, t_{web} can be increased. Table 6.6 shows the cases with two different angular velocities, ω and their final MD curl radius values. The load conditions for the case-I & II are shown in Table 6.5 where rubber covered roller is subjected to torque input, R_τ (torque input is explained in the later section 6.3.2). In case-I, the impact of viscoelasticity is not present because $t_{web} < \tau_1$. For the angular velocity 0.0628 rad/sec (case II), the web spent almost 2 seconds in the nip contact zone whose value is greater than τ_1 and so the MD curl is affected by the viscoelasticity of adhesive as shown in Figure 6.16.

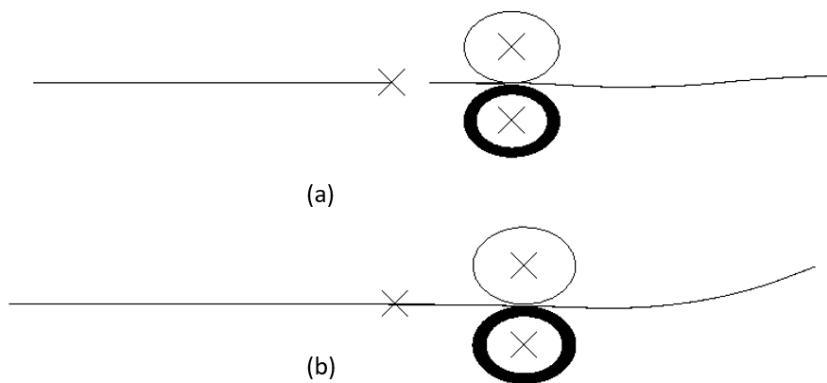


Figure 6.16: MD curl in the laminated web for (a)case-I; (b)case-II

Table 6.5: Loading conditions

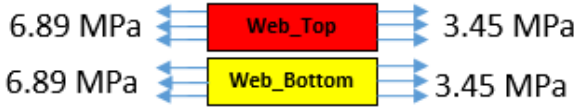
S. No.	Input Loads	Values
1	Web Tensions	
2	Nip Load, N	44.48 N/mm
3	Torque input, R_τ	169.48 N-mm

Table 6.6: MD Curl Radius for different angular velocities

case	Angular velocity, ω	t_{web} (sec)	τ_1 (sec)	MD curl radius (mm)
I	6.28	0.01	0.412	Flat web
II	0.0628	2	0.412	-541.78

From this section, it is clear that the impact of Adhesive's viscoelasticity on the final MD curl is present only if the time spent by the web in nip contact zone is greater than the first relaxation time constant (τ_1).

6.3. 2 Effect of torque input, R_τ on MD curl radius

Results discussed thus far (excluding section-6.3.1.2) do not have torque input to the Rubber Covered Roller. In those simulations, this roller is allowed to rotate freely. New simulations were conducted with torque input to study the impact on the MD curl of the laminated web. A limiting value based on friction for the torque can be obtained by satisfying the equilibrium Equation (6.14). Pictorial representation for this equilibrium equation is shown in the Figure 6.17.

$$R_\tau + (T \times A \times R) < \mu \times N \times R \quad (6.14)$$

Here, R_τ is the torque input, N-mm; T is web tension, MPa i.e. $|T_1 - T_2|$; A is the area on which web tension applied, mm^2 ; R is the radius of Rubber Covered Roller,

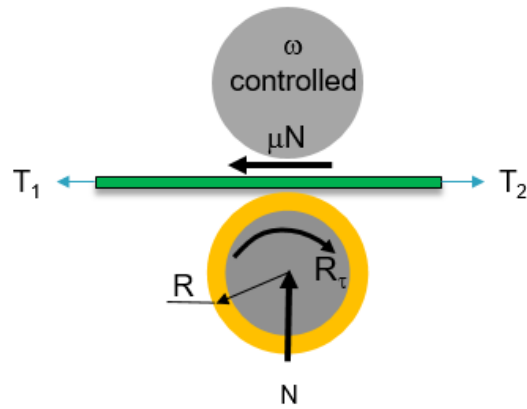


Figure 6.17: Pictorial representation representing notations for equilibrium equation mm; μ is the coefficient of friction between Rubber covered roller and web and N is the normal force i.e. Nip load, N/mm. For the present loading conditions from Table 6.3, the torque input is limited to 1016.86 N-mm. Simulations were conducted to explore the torque level that would cause the MD curl to vanish. From Figure 6.18, it is seen that curl free laminated web can be achieved for the torque input 112.98 and 141.23 N-mm.

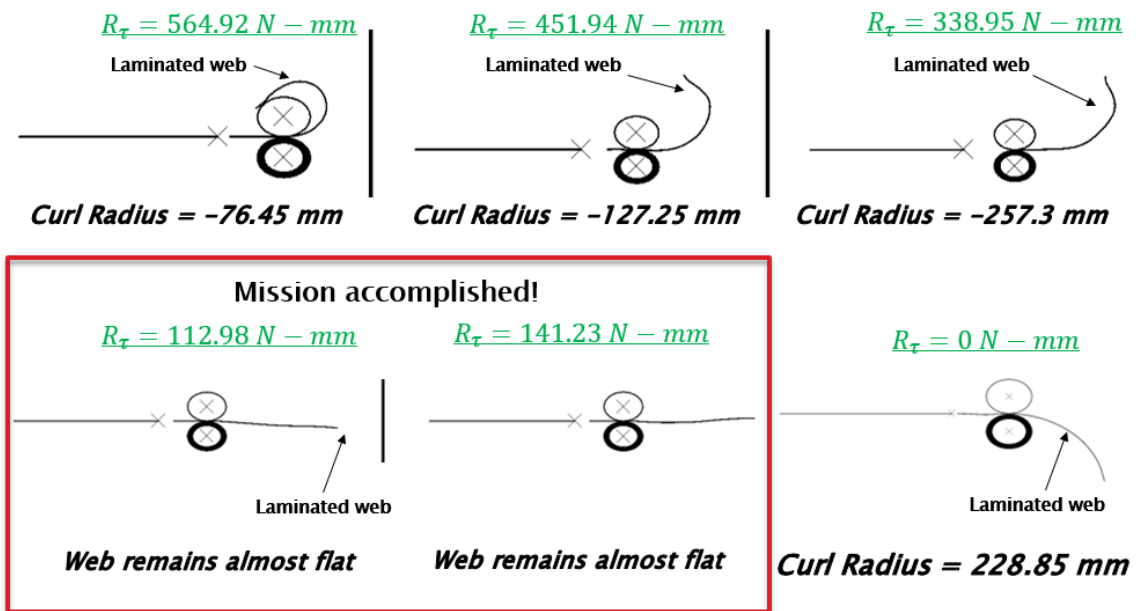


Figure 6.18: Final MD curl Radius of laminated web for different Torque inputs

Figure 6.19 shows the plot of the MD curls that resulted from simulation in

Swanson’s Kappa units. It shows the quasi linearity of the curl with respect to the torque applied. With increase of torque input, the curl radius is observed to be decreasing. It should be noted that this linear relationship would be affected by changes in web and adhesive properties, tensions, laminator roller diameters, cover properties and coefficients of friction.

For different web tensions applied, simulations were conducted to explore the torque level that would cause the MD curl to vanish. Also, the relationship of torque level with MD curl kappa is plotted to check if it differs from the relation shown in Figure 6.19. Table 6.7 shows the different web tensions cases and their corresponding torque levels at which MD curl is vanished. In Table 6.7, “+” sign torque represents an accelerating torque i.e. clockwise direction and “-” sign torque represents retarding torque i.e. counter-clockwise direction.

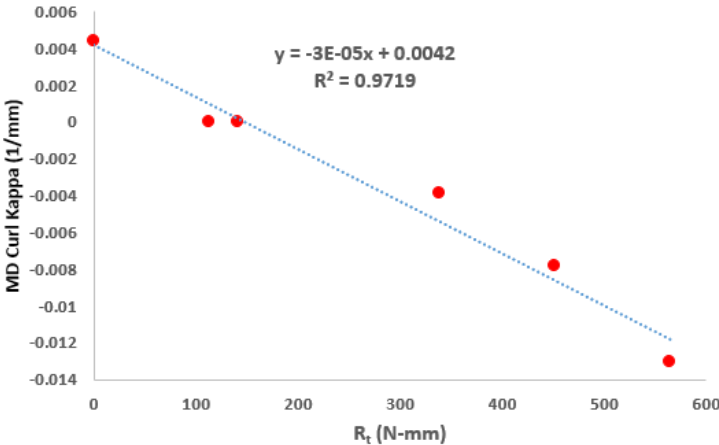


Figure 6.19: MD Curl Radius Vs. Torque input

Tension in the top web is more compare to the bottom web in Case-2 & 5 from Table 6.7 and so the retarding torque is required for the MD curl radius to vanish. Figure 6.20 shows the plot of the MD curls that resulted from simulation in Swanson’s Kappa units for Case-1 & 3. Both cases show quasi linearity of the curl with respect to the torque applied but with different set of equations. From plot in Figure 6.19, the curl radius is observed to be increasing with increase of torque input. From Figure

Table 6.7: Torque levels at which MD curl vanished for different web tension inputs

S. No.	Web Tensions, MPa	Torque limit, N-mm	Torque level at which $R_{curl}=0$
Case-1	<div style="display: flex; align-items: center; gap: 10px;"> <div style="text-align: center;">4.14 ←</div> <div style="border: 1px solid black; background-color: #d3d3d3; padding: 2px 10px; text-align: center;">Top_Web</div> <div style="text-align: center;">→ 3.45</div> </div> <div style="display: flex; align-items: center; gap: 10px;"> <div style="text-align: center;">4.83 ←</div> <div style="border: 1px solid black; background-color: #d3d3d3; padding: 2px 10px; text-align: center;">Bottom_Web</div> <div style="text-align: center;">→ 3.45</div> </div>	1084.65	56.49
Case-2	<div style="display: flex; align-items: center; gap: 10px;"> <div style="text-align: center;">4.83 ←</div> <div style="border: 1px solid black; background-color: #d3d3d3; padding: 2px 10px; text-align: center;">Top_Web</div> <div style="text-align: center;">→ 3.45</div> </div> <div style="display: flex; align-items: center; gap: 10px;"> <div style="text-align: center;">4.14 ←</div> <div style="border: 1px solid black; background-color: #d3d3d3; padding: 2px 10px; text-align: center;">Bottom_Web</div> <div style="text-align: center;">→ 3.45</div> </div>	1084.65	-45.19, -39.54
Case-3	<div style="display: flex; align-items: center; gap: 10px;"> <div style="text-align: center;">4.83 ←</div> <div style="border: 1px solid black; background-color: #d3d3d3; padding: 2px 10px; text-align: center;">Top_Web</div> <div style="text-align: center;">→ 3.45</div> </div> <div style="display: flex; align-items: center; gap: 10px;"> <div style="text-align: center;">4.83 ←</div> <div style="border: 1px solid black; background-color: #d3d3d3; padding: 2px 10px; text-align: center;">Bottom_Web</div> <div style="text-align: center;">→ 3.45</div> </div>	1084.65	39.54
Case-4	<div style="display: flex; align-items: center; gap: 10px;"> <div style="text-align: center;">4.14 ←</div> <div style="border: 1px solid black; background-color: #d3d3d3; padding: 2px 10px; text-align: center;">Top_Web</div> <div style="text-align: center;">→ 3.45</div> </div> <div style="display: flex; align-items: center; gap: 10px;"> <div style="text-align: center;">5.52 ←</div> <div style="border: 1px solid black; background-color: #d3d3d3; padding: 2px 10px; text-align: center;">Bottom_Web</div> <div style="text-align: center;">→ 3.45</div> </div>	1084.65	135.58
Case-5	<div style="display: flex; align-items: center; gap: 10px;"> <div style="text-align: center;">5.52 ←</div> <div style="border: 1px solid black; background-color: #d3d3d3; padding: 2px 10px; text-align: center;">Top_Web</div> <div style="text-align: center;">→ 3.45</div> </div> <div style="display: flex; align-items: center; gap: 10px;"> <div style="text-align: center;">4.14 ←</div> <div style="border: 1px solid black; background-color: #d3d3d3; padding: 2px 10px; text-align: center;">Bottom_Web</div> <div style="text-align: center;">→ 3.45</div> </div>	1084.65	-192.07

6.19 & 6.20, it is clear that the linear relationship is affected by changing the tensions applied on the web.

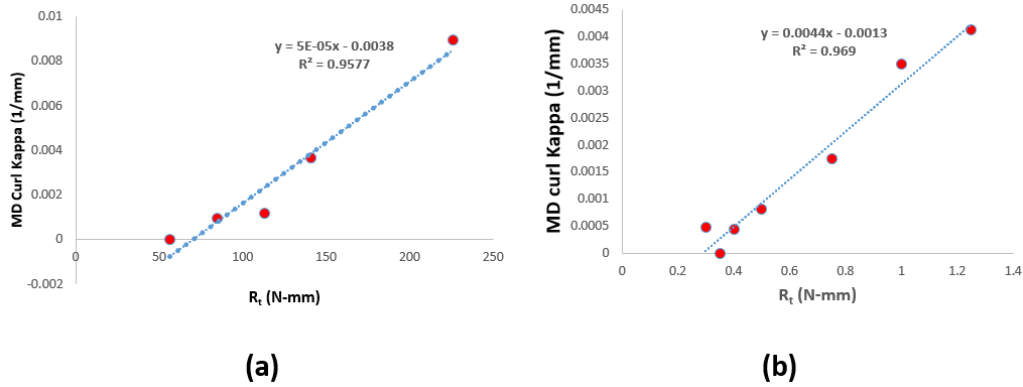


Figure 6.20: MD Curl Radius vs. Torque input for (a) Case-1; (b) Case-3

For Torque input 338.95 N-mm, shear strain of the adhesive layer in nip contact zone is shown in Figure 6.21 where MD curl radius is -261.87 mm For zero torque input the adhesive exited the nip contact zone with a shear strain of 0.144 rad (refer to Figure 6.12) where MD curl radius is 228.85 mm Now from Figure 6.21, it is seen that the adhesive is leaving the nip contact zone with a shear strain of -0.025 rad. This change in shear strain would affect the membrane tensions in the two webs as they exit and the level of MD curl.

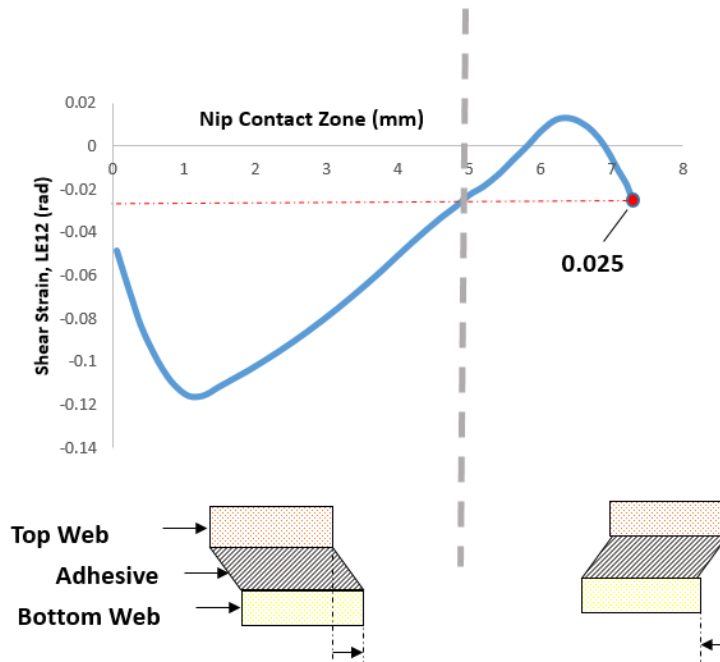


Figure 6.21: Shear Strain of Adhesive layer in Nip contact zone for $R_{\tau}=3$ lb.-in

Figure 6.22 shows the shear strain of adhesive layer in nip contact zone for different torque inputs. This chart demonstrates how the shear strain in the adhesive layer for model-IV is effected by torque input to the rubber covered roller. It is noted that the shear strain levels at the entry to the nip contact are very similar compared to the decrease with torque witnessed at the exit. The location at which shear strain values change from negative to positive are moved right in the graph with increase of torque input. For torque inputs of 451.94 and 564.92 N-mm, negative shear strain values are witnessed at the exit. For different torque levels, the shear strain at which webs leave the nip contact zone is varied resulting in different MD curls.

Contact status for the bottom web are plotted for all the torque input levels as shown in Figure 6.23. For the bottom web that is in contact with rubber cover roller, slip is observed at the exit of the nip contact zone. With increase of torque input, slip zone is observed to be increased. This slippage can be responsible for changes in the laminae tension that could also affect the MD curl at the exit.

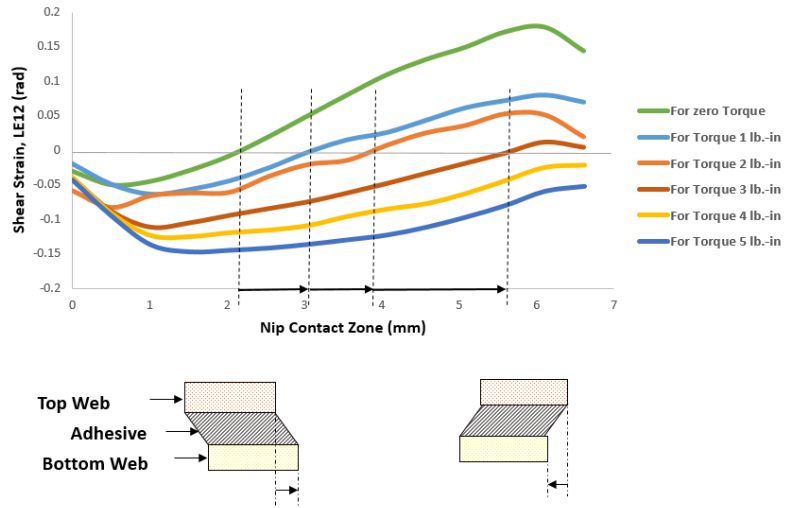


Figure 6.22: Shear Strain of Adhesive layer in Nip contact zone for different R_τ levels

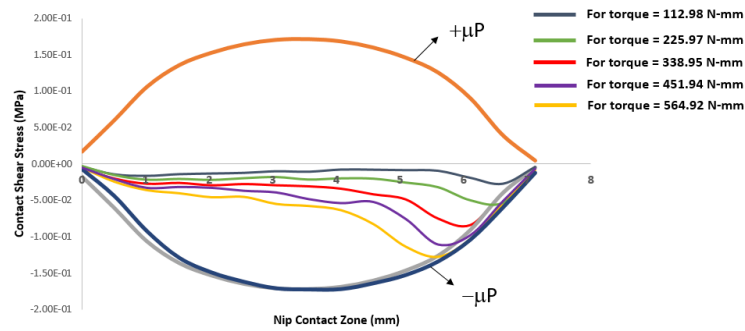


Figure 6.23: Contact status of the bottom web for different R_τ levels

Whereas for the top web that is in contact with the rigid roller, a small amount of slip zone is observed as shown in Figure 6.24 for 564.92 N-mm torque at the exit of nip contact zone. With increase of torque input, Shear stress values are observed to be reducing. For the zero torque case (refer to Figure 6.13(b)), some slip was observed opposite in direction to that which is observed here at 564.92 N-mm.

For given web (section 5.1), rubber cover (section 5.1) & adhesive layer (Table 6.2) materials and loading conditions (table 6.3) excluding R_τ , curl free laminated web can be obtained for the torque inputs as shown in Table 6.7.

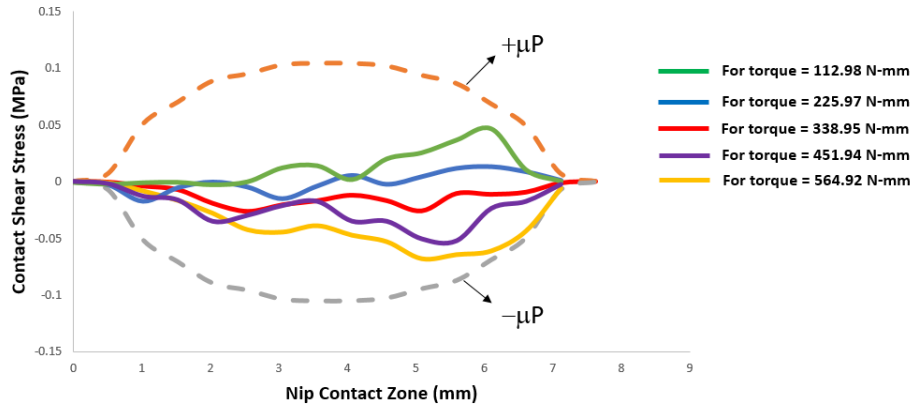


Figure 6.24: Contact status of the top web for different R_τ levels

6.4 Introducing Adhesive layer in the lamination Model-III

In the model-III, webs enter the nip rollers at a wrap angle, θ in the lamination process as shown in figure 5.1(c). For wrap angle 45° and 90° , the lamination model is developed with an adhesive layer in between the laminae as shown in Figure 6.25 and it is named “Model-V”. The boundary conditions and amplitudes of loading conditions are similar to the previous models (Refer to Figure 5.3 & 5.4). In this model, the adhesive layer is attached to the top web initially and laminates with the bottom web at nip contact zone. The material properties of the adhesive layer used for Finite Element Analysis are defined in the previous section (Table 6.2).

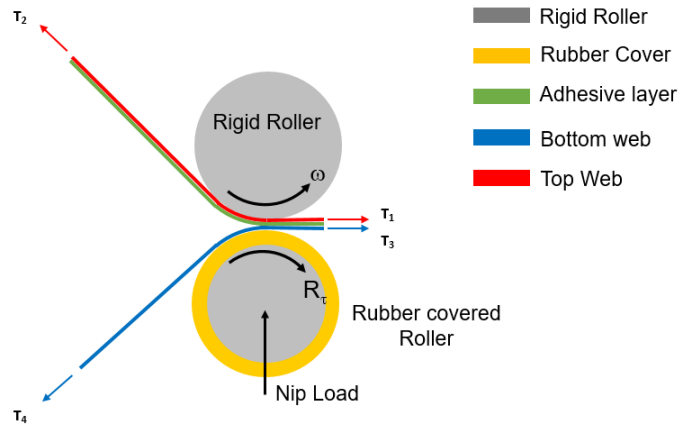
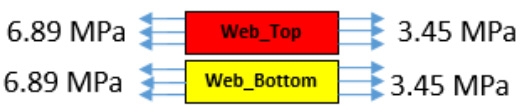


Figure 6.25: Model setup in Abaqus for model-V

For the present analysis, the loads applied for the model-IV are shown in Table 6.8. For Torque input 338.95 N-mm, shear strain of the adhesive layer in nip contact zone is shown in Figure 6.26 for the model-IV (i.e. straight webs) and model V (i.e. webs entering at wrap angle 45^0 and 90^0). Web leaves the nip contact zone at different shear strain values for all three cases and so it resulted in different MD curls.

Table 6.8: Loading conditions

S. No.	Input Loads	Values
1	Web Tensions	
2	Nip Load, N	44.48 N/mm
3	Angular velocity, ω	6.28 rad/sec

For 90^0 wrap angle, loading condition that gives almost curl free laminated web is obtained as shown in Figure 6.27(a). The corresponding loading conditions are: Web Tensions – “3.45 MPa” on the right side of webs and “6.89 MPa” on the left side of webs; Nip load – “22.24 N/mm”; Angular Velocity – “6.28 rad/sec” and applied torque – “-135.58 N-mm”.

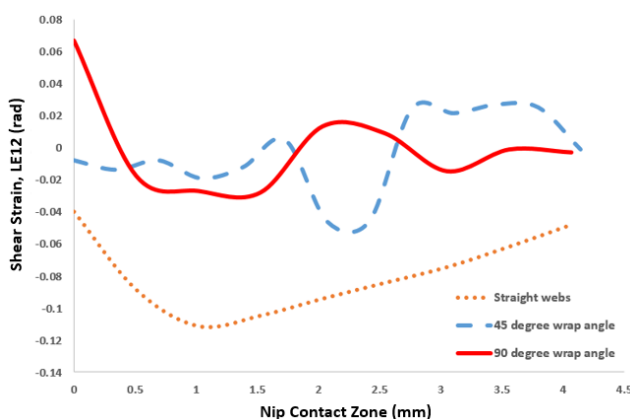


Figure 6.26: Shear Strain of Adhesive layer in Nip Contact Zone

For 45^0 wrap angle, loading condition that gives almost curl free laminated web

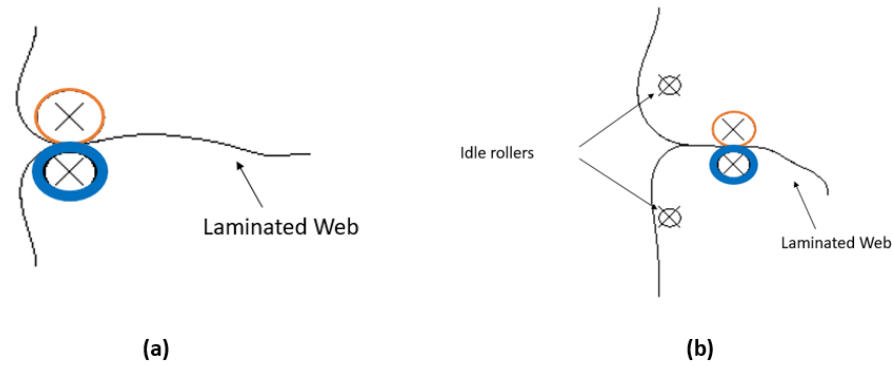


Figure 6.27: Curl free laminated web for (a) Wrap angle 90° ; (b) wrap angle 45° is obtained as shown in Figure 6.27(b). The corresponding loading conditions are: Web Tensions – “3.45 MPa” on the right side of webs and “6.89 MPa” on the left side of webs; Nip load – “44.48 N/mm”; Angular Velocity – “6.28 rad/sec” and applied torque – “677.91 N-mm”. Due to the dynamic instabilities in the simulations, the perfect straight laminated web is not seen in the above Figure 6.27. But the web region that passed through nip contact zone under steady load condition has infinite curl radius i.e. flat web.

From the results for Model-IV & V, it is clear that the shear strain of the adhesive layer and contact status in nip contact zone influences the MD curl radius of the laminated web.

CHAPTER VII

FINDINGS AND CONCLUSIONS FOR THE LAMINATION MODEL RESEARCH

This research has demonstrated that the Dynamic Implicit solution method offered in Abaqus Standard has the precision needed to explore the modelling of lamination process to study the parameters resulting in the MD curl.

- For model-I lamination i.e. lamination of webs between two rigid rollers, the MD curl only depends on the strain in the laminae i.e. tensions applied on the webs.
- For model-II model-III lamination i.e. lamination of webs between a rigid roller and rubber covered roller, additional parameters i.e. nip load, angular velocity and wrap angle are observed to affect the MD curl by introducing rubber cover to one of the rigid rollers.
- Due to the contact algorithm defined for the web interaction, webs were struck together once they are laminated resulting in no shear. In reality, there will be shear between the webs due to the adhesive. Therefore, an adhesive layer is introduced between the webs in the model-IV.
- The viscoelastic behavior of the adhesive layer is defined using a Generalized Maxwell Model fitted on experimental data. The viscoelastic behavior of the adhesive is observed only if the relaxation time is less or comparable to the time

spent by the web in the contact zone.

- The torque input to the rubber-covered roller is studied for the model-IV.
- For the defined web, adhesive, and rubber cover materials, a curl free laminated webs can be produced for the following loading conditions:
 - ⇒ Angular velocity : 6.28 rad/sec
 - ⇒ Nip Load : 44.48 N/mm
 - ⇒ Web tensions and corresponding torque inputs, R_τ :

Web Tensions, MPa	Torque level at which $R_{curl}=0$ (N-mm)
4.14 ← Top_Web → 3.45 4.83 ← Bottom_Web → 3.45	56.49
4.83 ← Top_Web → 3.45 4.14 ← Bottom_Web → 3.45	-45.19, -39.54
4.83 ← Top_Web → 3.45 4.83 ← Bottom_Web → 3.45	39.54
4.14 ← Top_Web → 3.45 5.52 ← Bottom_Web → 3.45	135.58
5.52 ← Top_Web → 3.45 4.14 ← Bottom_Web → 3.45	-192.07

- A general laminator operating chart used by the operators in industry representing curl as a function of incoming strain ratio torque magnitude and direction supplied to the rubber roller is shown in Figure 11.8(a). The models we developed exhibit a similar behavior, shown on Figure 11.8(b). For strain matched conditions, different laminated web curls are observed for different torque levels (Figure 6.18) and curl-free laminated webs are obtained for strain mismatch conditions for a particular given torque (Table 6.7). This explains clearly the torque applied to the rubber-covered roller, and the strain match and mismatch conditions are primary controls for the curl in a lamination process.

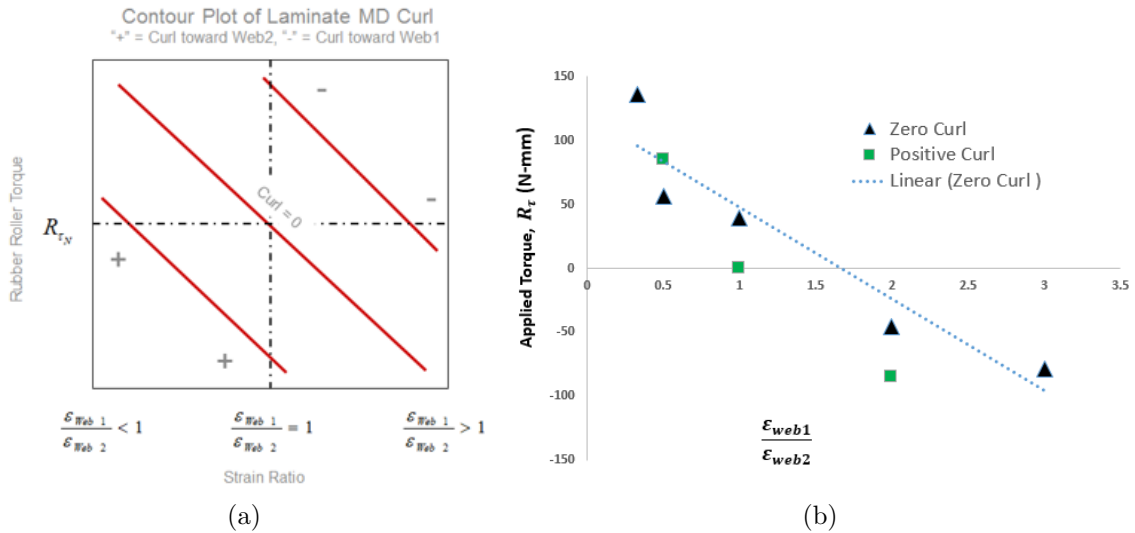


Figure 7.1: (a) Laminator operating chart, (b) Laminator operating chart for the developed model

Conclusions

Therefore, the Primary controls of curl are:

- o Strain match or mismatch (which is controlled by the tension applied on incoming webs)
- o Torque applied to rubber-covered roller
- o Viscoelastic properties of the adhesive, which can be important if the residence time at the nip contact is greater than the lowest viscoelastic relaxation time. This makes the velocity of lamination important.

o Entry wrap angle.

The secondary controls of curl are:

- o Nip load

The remaining Unknown controls of curl are:

- o Nip diameter
- o Rubber cover thickness
- o Rubber hardness

CASE STUDY 2: WINDING OF ULTRAVIOLET NANOIMPRESSION
LITHOGRAPHY'S NANO-IMPRINTED WEBS

CHAPTER VIII

INTRODUCTION TO UV-NIL PROCESS

Over the past decade, the nanopatterning technology has been greatly developed by taking the advantage of its high performance, small size and energy saving which can be widely used in the fields of optical communication, photovoltaics, biology and energy. Nanoimprint lithography (NIL) process is widely used in the nanopatterning technology. NIL is a method of fabricating nanometer scale patterns by deforming the imprint resist. The imprint resist is typically a monomer or polymer formulation that is cured by heat or UV light during the imprinting as shown in the Figure 8.1. The release of mold from pattern is controlled by the adhesion between the resist and the template. There are many types of NIL processes but the important process which is mostly used are: Thermal nanoimprint lithography (T-NIL) and ultraviolet nanoimprint lithography (UV-NIL).

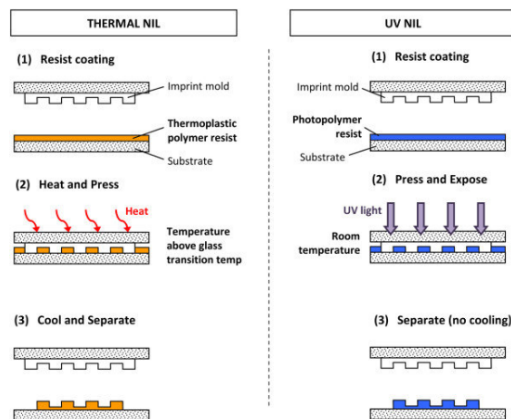


Figure 8.1: Schematic diagram of Thermal-NIL and UV-NIL Process

The Thermal-NIL process, also known as hot embossing involves the imprinting the pattern onto a thermally softened thermoplastic polymer resist [61]. Thermal-NIL process is as follows: A mold is first heated up to an elevated temperature higher than the glass transition temperature (T_g) of the thermoplastic polymer resist. As the heated mold comes in contact with the resist, the resist will be heated up and soften into a molten stage, where it will fill in the mold cavities with sufficient imprinting pressure and time. Once the polymer resist is imprinted, the temperature is lowered below the T_g to solidify the resist before the mold is lifted. Therefore, the patterns from the mold are transferred to the resist.

In contrary to the thermal NIL process, the UV NIL process involves imprinting onto a layer of liquid photopolymer resist and then it is cured using UV radiation. Exposing UV light to the polymer resist, it undergoes cross-linking which results in hardening of the polymer [62]. Rest of the imprinting mechanism is similar to thermal NIL process as shown in the Figure 8.1. However, UV-NIL process has several advantages compared to thermal NIL process such as ability to perform UV-NIL at room temperature which requires no temperature cycle (eliminates thermal expansion variation between the mold, substrate and resist issues), low imprint pressure and high speed in production.

The production of nanoimprints using UV-NIL is generally done in discrete stamping which is slow and restricted to small production volumes. Scaling UV-NIL to Roll-to-Roll (R2R) manufacturing process can overcome the above-mentioned obstructions and result in high production. This manufacturing method enables imprinting on flexible substrates with increased production of nanostructures. At the beginning of developing R2R NIL process [21], the processing speed was restricted to 1 m/min due to the limited knowledge about continuous manufacturing process and UV curable resist material. With the development of UV curable resist, UV light

source, mold fabrication and web processing, high speed continuous R2R UV-NIL manufacturing is achieved with high production rate and reduced cost.

In the present research, imprint of nanosize patterns on the flexible strip i.e. web using continuous R2R UV-NIL is focused and in particular, the winding part of the process is studied. The continuous R2R UV-NIL process consists of prefabricated mold with inverse of the desired pattern which is attached on the surface of imprint roller, backup roller (to apply pressure on the resist filling), peel roller to release resist from the mold and UV light source for curing as shown in the Figure 8.2. The bottom layer of the web is coated with UV curable resist continuously at the beginning of the process (left side to the nip set). Once the resist coated web reaches the nip set, the mold on the imprinted roller comes in contact with the resist. Here nip set is referenced to imprinting roller and backup roller. The cavities of mold is filled with the resist completely by applying pressure on the top layer of the web with backup roller. Simultaneously, the resist undergoes curing using the UV light resource where resist is exposed to UV light through web. Once web reaches the imprint roller, the peel roller is used to release the resist from the mold without break in the nanoimprint patterns.

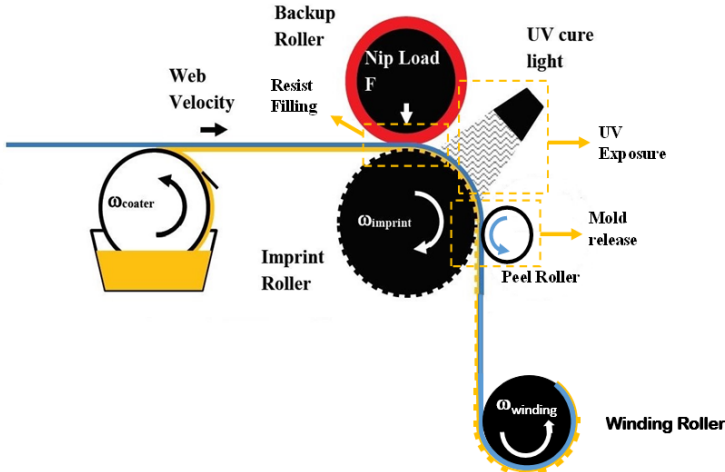


Figure 8.2: Schematic diagram of R2R UV-NIL Process

Once the webs with UV curable resist nanoimprints are manufactured, they are stored in wound roll form by winding the webs on the winding roller until they are needed in a subsequent R2R, where they are unwound and further processed. The imprinting of UV curable resist in UV-NIL processes is very precise. The period, height, and duty cycle of the nano-features are dictated by the needs of a product, which is often an optical filter with unique capabilities. Anything that would deform these features either permanently or temporarily would affect the performance of the product. The polymeric cured UV resists are expected to be viscoelastic on some time scale. The goal of the present research is to predict the pressures in the wound roll and how the nano-imprinted features will be distorted through time while subject to those pressures. This will help in establishing how the imprinted materials should be wound and how long they can be subjected to pressure in the wound roll before they should be unwound to limit the deformation of the nano-imprinted features. In the current study, the PET web is imprinted with masterbond UV-15 resin (UV curable resin) at the nanosize of 240 nanometers using R2R UV-NIL process. Here, the resist is also known as resin.

CHAPTER IX

LITERATURE REVIEW

9.1 Review on Roll-to-Roll UV-NIL Process

With an urge for developing low-cost technology for mass production of nano structures, Chou [17, 63, 64] was the first researcher to introduce nanoimprint lithography in 1995. Thermal nanoimprint lithography was demonstrated where Chou imprinted 25 nm Ti/Au diameter dots with a 120 nm period on 55 nm thick PMMA films with SiO_2 mold as shown in Figure 9.1.

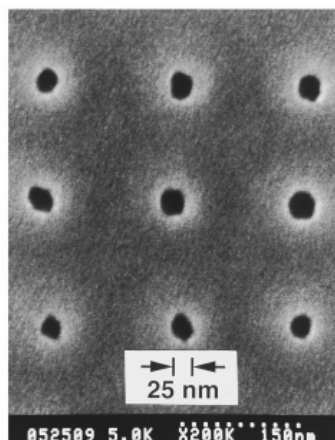


Figure 9.1: Scanning electron microscope image of dot patterns imprinted on PMMA [17]

The mold and PMMA film were first heated to a temperature of 200°C which is higher than the glass transition temperature, T_g of PMMA film (i.e. 105°C) during the imprinting stage. Once the mold and PMMA film reached the required

temperature, the mold was compressed on the PMMA film and held there until the temperature drops to below T_g of PMMA. Tests were performed for various imprint pressure and found that the 1900 psi was the optimum pressure. At this pressure, it was shown that the pattern from the mold was successfully transferred to the PMMA film. A schematic diagram for this process is shown in Figure 9.2.

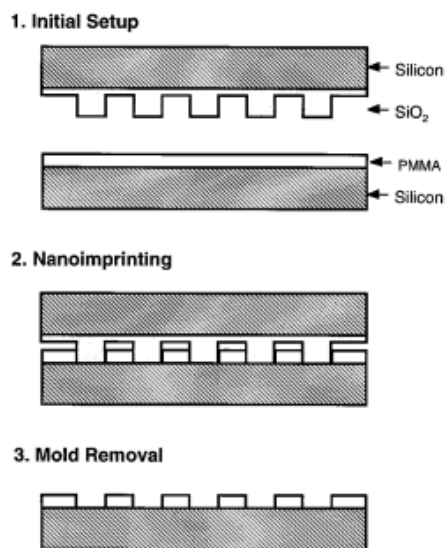


Figure 9.2: Schematic of thermal nanoimprint lithography process [17]

Later, Ultraviolet Nanoimprint lithography was first introduced by Haisma [18] in 1996. A resin with high curing rate, low viscosity and good adhesion to the substrate after curing is considered for this study i.e. 1,6-hexanediol-diacrylate (HDDA) and bis(hydroxyethyl) bisphenol-A dimethacrylate (HEBDM) as photopolymerizable monomers with dimethoxy-phenyl-acetophenone (DMPA) as a photoinitiator. The UV NIL process with a schematic diagram is shown in Figure 9.3. In the first step, the surfaces of the mold and the substrate were cleaned and provided with release layer and a primer respectively. A thin layer of UV curable resin i.e. HDDA is applied on the substrate using spin coating. Then, the mold is pressed on the substrate after they are aligned. HDDA is exposed to the UV light for the solidification and then mold is removed from the HDDA leaving imprints on the substrate. Contrary

to the T-NIL process, the mold is imprinting on a liquid layer of the resist in the UV-NIL process. The solidification of resin is a cross-linking reaction in a polymer instead of controlling phase change of a thermoplastic with temperature [65].

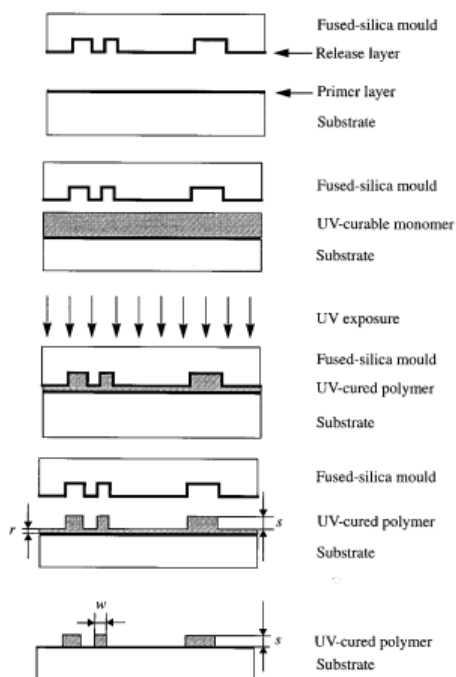


Figure 9.3: Schematic of UV nanoimprint lithography process [18]

Imprinting on a UV curable resin with low viscosity requires low imprint pressure compare to thermal NIL process [66, 67, 68, 69, 70, 71] and also it requires less time to fill the cavities of the mold. Elimination of temperature cycles decreases the production time [67]. However, there are defects in this process such as air bubble trap [72], residual stress due to polymerization [73] etc,. However this process is most attracted in the IC semiconductor industry due to its ability to perform the process at room temperature [74]. The results discussed thus far are performed on the plate to plate contact. The process can be further increased in productivity with lowering the cost with an alternative method called roller nanoimprint lithography by Chou group [19] in 1998. Two methods for the roller nanoimprint lithography (RNIL) was demonstrated. One method was cycle mold method. In this paper, the cycle mold was

made by bending a thin metal film mold around a smooth roller with $100\ \mu\text{m}$ thick and $700\ \mu\text{m}$ wide and Ni material was used for the mold. Si wafer of $0.5\ \text{mm}$ thick was used as substrate with $200\ \text{nm}$ PMMA cast on the top. During the RNIL with cycle mold method, the mold was pressed into the PMMA resist and the roller was rotated to push the sample forward as shown in Figure 9.4(a). The second method was the flat mold method where a smooth roller is rotated over the mold (which is on the top of the PMMA resist). The slight pressure of the roller deformed the imprint patterns in the resist as shown in Figure 9.4(b).

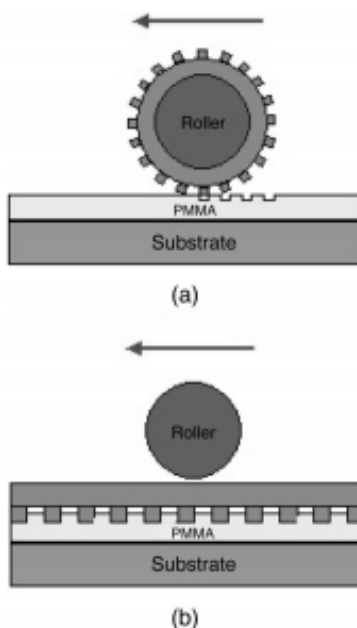


Figure 9.4: Roller nanoimprint lithography (a) cycle mold method; (b) flat mold method [19]

In both methods, the roller temperature was set well above the glass transition temperature, T_g , of the resist, while the temperature of the platform was set below the T_g . Therefore, only the area in contact with the roller had a temperature higher than T_g , making the resist in that area flow and being imprinted with patterns. This is different from thermal NIL with plate to plate (P2P) contact, where the entire resist was heated above T_g and the imprinting was performed simultaneously with

holding the applied pressure until the resist is cooled down, hardened. Due to this temperature cycling, RNIL required a long period of time to transfer the pattern from mold to the PMMA resist. As the rotating roller has limited time contacting PMMA, the accuracy of the replication was not as good as flat mold method (i.e. P2P thermal NIL). Although the results obtained by Chou's team showed limited accuracy, this roller nanoimprinting method does provide a possibility of continuous manufacturing process and has an inspiration for the next generation of roll-to-roll nanoimprint lithography (R2R NIL).

With an increase in demand for nanopattern imprints with low cost mass production, the continuous UV-NIL process using a pattern roll stamper for the replication of large scale nanoimprint patterns was first introduced by Ahn [20] in 2006. The continuous UV roll nanoimprinting system was developed for both flexible and rigid substrates as shown in Figure 9.5. In this study, urethane acrylate photopolymer with a viscosity of 300 cP at 25 °C was used as the imprinting material on polyethylene terephthalate film. The components of UV roll nanoimprinting system are: **The dispensing unit** which was used for coating the UV-curable resin onto the substrate using dispenser needle, the pair of flattening rollers which enables the uniform coating of the resin onto the substrate; **UV illumination unit** illuminates UV light on the curing region where the roll stamper comes in contact with the UV-curable resin and the cavity of stamper is filled with the UV-curable resin. The condensing lens was used for the replication on rigid substrates as shown in Figure 9.5(a). For flexible substrates, releasing roller was used to peel the UV-curable resin from the mold without tearing the mold pattern as shown in Figure 9.5(b).

The imprint results on the flexible substrate was demonstrated for two different nanopatterns as shown in Figure 9.6. Figure 9.6(a) shows the Scanning electron microscope (SEM) and focused ion beam (FIB) section images of line structures

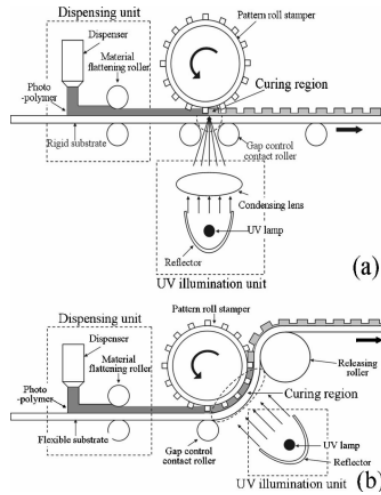


Figure 9.5: Schematic diagram of continuous UV-NIL process (a) for a rigid substrate; (b) for a flexible substrate [20]

with width of 500 nm, pitch of 1000 nm, height of 900 nm on stamper and imprinted pattern. Figure 9.6(b) shows SEM images and atomic force microscope (AFM) profiles of imprinted nanopillars with a diameter of 50 nm, a pitch of 150 nm, and a height of 35 nm. As shown in AFM image, the profile of the roll stampers and the 50 nm pillar patterns were compared and the deviation was shown to be less than 3 nm. With these results, Anh concluded that the continuous nanoimprinting process can be used in the large-area replication of nano- and micropatterns in the mass production of large flexible displays, optical elements, ultrahigh density storage, and so on. This continuous NIL process can be addressed as Roll-to-Roll (R2R) NIL process.

R2R NIL can enable imprinting nanostructures on a flexible film with drastically increased output, leading the nanoimprint lithography to a brand new level. In 2007, Guo and Ahn [21] reported a high speed R2R NIL process on a flexible substrate. R2R NIL process was demonstrated for both thermal based and UV based curing in this paper. Mold used for the process should be flexible enough to wrap onto a roller surface and also strong enough to imprint the resist. A flexible fluoropolymer, ethylene-tetrafluoroethylene (ETFE) was used as mold material for UVNIL process and Si mold is used for the thermal NIL process. For choosing resist material, they

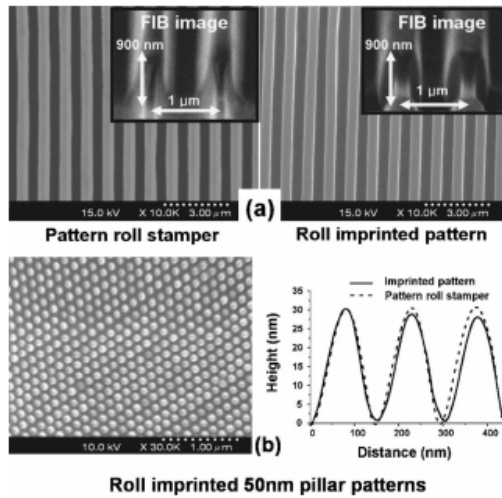


Figure 9.6: Replication results (a) SEM and FIB images; (b) SEM and AFM images [20]

were looking for a liquid resist with good coating properties, low viscosity before curing. For thermal R2RNIL process, liquid resist based on PDMS was used. Whereas, liquid epoxysilicone was used as imprint resist material for UV R2RNIL process. For both the processes, PET web was used as substrate. The schematic diagram for R2RNIL process is shown in Figure 9.7.

In this experiments, two types of coating methods i.e. reverse and forward web coating were used. As shown in Figure 9.7(b), web direction is opposite to the rolling direction for reverse coating and vice versa for forward coating. For thinner film layers, forward coating was used and thicker film layer were produced with reverse coating. Liquid resist is transferred from resist-container to the flexible PET substrate by the coating roller and its final thickness is controlled by doctor blade as shown in Figure 9.7(b). Once the resist is coated PET substrate, it enters the imprinting process unit which is very important as this involves the imprint pattern quality. It consists of a imprint roller, two backup rollers, a release roller and a curing section as shown in Figure 9.7(c). Under the web tension and the pressure from backup roller, the liquid resist quickly fills the mold cavity. In the next step, the resist precursor is cured either by UV exposure or convection heat based on its process method. For UV

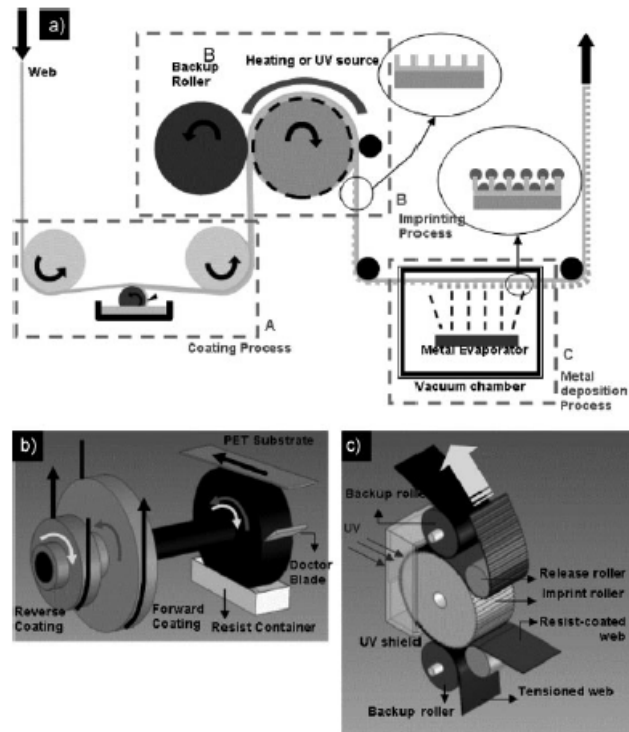


Figure 9.7: (a)Schematic of R2RNIL Process; (b)The coating unit; (c)Imprint unit [21]

R2RNIL process, the vacuum chamber is not required because the resist is cured via cathodic curing mechanism and therefore it frees the oxygen sensitivity issue when exposed to air. 9.7.

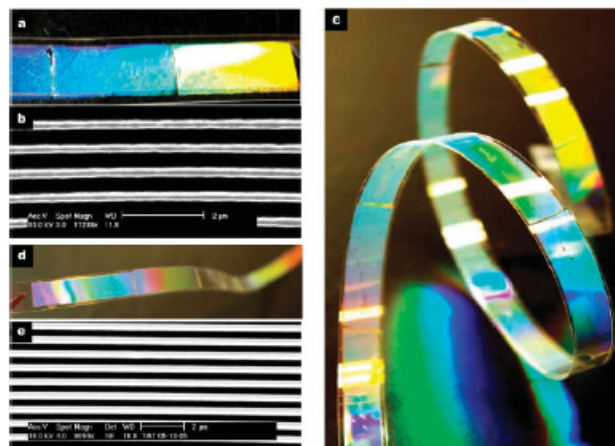


Figure 9.8: (a)Photograph of imprinted PET web with thermal R2RNIL process; (b,e)SEM micrograph of the replicated grating structure; (c,d)Photograph of imprinted PET web with UV R2RNIL process [21]

Using thermal R2RNIL process, 200 mm long, 300 nm line width and 700 nm period grating imprinted on thermally cured PDMS on a PET substrate as shown in Figure 9.8(a)&(b). Using UV R2RNIL process, 570 mm long (10 mm width), 700 nm period grating structure on PET substrate as shown in Figure 9.8(c)-(e). This process was performed at a speed of 1.3 - 23.5 mm/s. With the promising results, it was concluded that the R2RNIL process showed the drastic increase in the process throughput, which addressed one of the bottlenecks in the nanopatterning for many practical applications. Later many researchers have worked on R2RNIL process development. Maury et al. [22] manufactured a flexible electronic by R2R UV NIL at manufacturing speed is at 0.1 m/min (1.6 mm/s). Apparently, the manufacturing speed is relatively low, which limits the output of process. Later, H. Yoshikawa and his team [75] successfully increased the speed to 18 m/min.

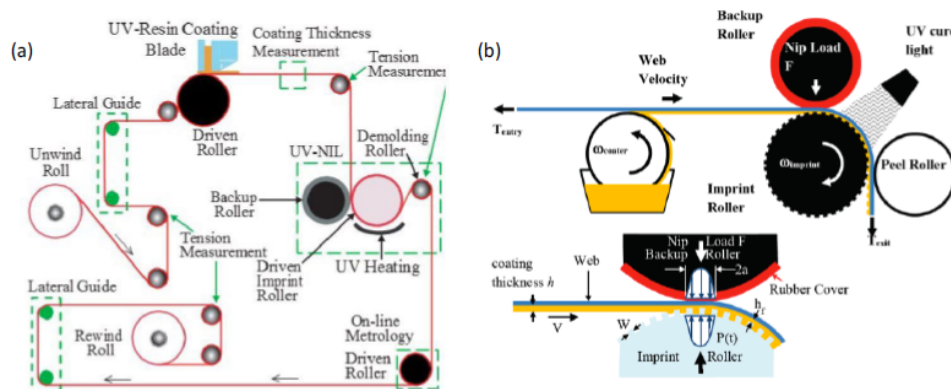


Figure 9.9: (a) Schematic of nanopattern fabrication producing line for R2R UV NIL (b) Schematic of R2R UV NIL and nip mechanics in nip contact zone [22]

Test bed for UV R2RNIL process was developed by Good [76]. The main components of apparatus for R2R UV NIL process involved dispensing unit (also called coating unit), imprint unit (imprint mold, flexible substrate (usually using web), backup roller, and peel roller), UV illumination unit, as well as storage unit (winding roller). As shown in Figure 9.9, the mechanics in the nip contact zone and flexible substrate will affect the quality of final nanopatterns transferring. The imprinted web

produced from this test bed at Web handling Research center are considered for the current research. The optimum results were shown for the web speed of 5 m/min.

From this section, it is clear that the UV R2RNIL process manufactures an accurate replicated nanoimprints on a flexible substrate with low cost and high production. Once the webs are imprinted with nanopatterns, they are stored in the wound rolls by winding process until they are used later for the required processing. The current research is focused on the winding part of the nanoimprinted webs and so the literature for the winding models are reviewed in the next section.

9.2 Review on Winding Models

9.2. 1 Elastic Winding Models

Winding models tell us about the stresses inside the wound roll which are key to understanding certain wound roll defects. If the stresses are too low the roll may not withstand handling loads without deforming. Conversely if stresses are too high the material may be damaged. Telescoping, flat tire are some of the examples for low pressure defects. Defects like blocking of layers on sticky products and bulk reduction on tender products like nonwovens are related to high stress defects.

In one dimensional winding models, the stresses varies with respect to radial location in the roll, but not across the width. Even though two stresses i.e. radial (σ_r) and tangential (σ_θ) stresses can be computed, the model is still one dimensional. Up to 1990, research work was done only for one dimensional winding models. The first linear isotropic winding model was developed by Gutterman [77] in late 1950s on magnetic tape winding. Shortly thereafter, similar work was performed by Catlow and Walls [78] for the textile industry in 1962 where 1D linear winding model for

isotropic material is developed. Later, many other researchers used the similar model i.e. simple isotropic modeling to report their work results on winding [79,80,81,82].

In reality, the webs used in the industry are far from isotropic. For some materials, the ratio of tangential to radial moduli can be equal to 1,000. Also, the radial modulus is not constant and is shown to depend on the pressure. So, the assumption of isotropy in the earlier works later found to be inaccurate. Nonetheless these models did capture the accretive behavior of winding and showed the approximated stress conditions inside the rolls.

The first widely used description of stack compression was by Pfeiffer [83, 84]. He noted a logarithmic behavior between pressure and strain in a stack of web material in compression. Based on that relation Pfeiffer concluded that the radial modulus was state dependent and linearly related to the stack pressure (Equation (9.1)):

$$\begin{aligned} P &= K_1(e^{K_2\epsilon_r} - 1) \\ E_r &= \frac{P}{\epsilon_r} = K_2(P + K_1) \end{aligned} \tag{9.1}$$

Where E_r is the radial Young's modulus, P is the pressure applied on the stack and ϵ_r is the strain that resulted in the stack. K_1 and K_2 are parameters that are fitted to the pressure versus strain data recorded from a compression test on the stack.

The work of Hakiel [85, 86] showed that the data from stack compression tests showed better correlation to a higher order polynomial than a logarithmic expression. The expression for the radial modulus as a function of pressure (Equation (9.2)):

$$E_r = C_1 + C_2P + C_3P^2 \tag{9.2}$$

C_1 , C_2 , and C_3 coefficients are fitted to pressure vs strain data in a stack com-

pression test. However, these relations are empirical and have no first principle basis. Thus, other relationships were also developed later as shown below. Hakiel developed another relationship as shown in Equation (9.3) which asymptotically reaches a constant C_0 at high pressure. The constant C_1 depends on the surface roughness of the film.

$$E_r = C_1(1 - e^{\frac{\sigma_r}{C_1}}) \quad (9.3)$$

Another expression is developed by Ducotey as shown in the Equation (9.4).

$$E_r = (C_0 + C_1\sigma_p)_2^C \quad (9.4)$$

It is more convenient to use Equation (9.1) as K_1 is typically quite small and the dimensionless value of K_2 is used to compare the state dependent radial modulus of various web materials.

Winding models depends on several types of equations whose roots come from basic principles of physics. The first type of equation is called equilibrium equation as shown in Equation (9.5). Second type of equation is called a constitutive equations as shown in Equation (9.6) and the final equation is called strain compatibility equation given by Equation (9.7)

$$\textit{Equilibrium equation} : r \frac{\partial \sigma_r}{\partial r} + \sigma_r - \sigma_\theta = 0 \quad (9.5)$$

$$\begin{aligned} \textit{Constitutive equation} : \epsilon_r &= \frac{\sigma_r}{E_r} - \nu_{r\theta} \frac{\sigma_\theta}{E_\theta} \\ \epsilon_\theta &= \frac{\sigma_\theta}{E_\theta} - \nu_{\theta r} \frac{\sigma_r}{E_r} \end{aligned} \quad (9.6)$$

$$\textit{Strain compatibility} : r \frac{\partial \epsilon_\theta}{\partial r} - \epsilon_r + \epsilon_\theta = 0 \quad (9.7)$$

The above three equations were combined by Hakiel [86] to form a winding equation as shown in Equation (9.8) that adequately generate numerical values for the stresses in the wound roll. This is known as one dimensional winding model as the stresses were only dependent on the radial direction, but not the circumference nor, more importantly axial direction. The first model to account for accretion (adding layers), orthotropic properties, a radial modulus (that depends on the pressure) and the impact of core.

$$r^2 \frac{d^2 \sigma_r}{dr^2} + 3r \frac{d\sigma_r}{dr} - \left(\frac{E_\theta}{E_r} - 1 \right) \sigma_r = 0 \quad (9.8)$$

Where, σ_r is the radial stress, E_θ and E_r are the tangential and radial modulus, respectively. The expression is written in terms of incremental radial stresses (σ_r), each increment representing the addition of the most recent layer. Radial stresses and incremental radial stresses vary with radius. After solving Equation (9.8), the σ_r stress increments in each layer are added to the total σ_r stress that was already sustained by that layer. The radial modulus is then updated as a function of the total radial stress in each layer.

Since the winding equation is second order differential equation, two boundary conditions are required to solve the equation. The first boundary condition is called core modulus, E_c , also known as inner boundary condition as shown in Equation (9.9). The core modulus is not a material property. It is a stiffness relationship between the applied pressure at the core and its inward strain.

$$E_c = \frac{\sigma_r}{w/r} \Big|_{r=r_0} \quad (9.9)$$

Here, E_c is the core stiffness used for input to winding model, w is radial displacement (positive outward), r is radius and r_o is core outer radius. The second boundary condition is called wound-in-tension (WIT) also called the outer boundary

condition as shown in Equation (9.10). It is the total tightness of the current outer web wrap as it is added to the winding roll.

$$\sigma_r|_{r=s} = -\frac{T_w|_{r=s}}{s}h \quad (9.10)$$

Here, r is the radial position in roll, s is the current outer radius, h is the web thickness and T_w is web tension in outer wrap. Rewriting the Equation (9.9) for incremental radial stress (σ_r),

$$\frac{u}{r_c} = u|_{r=r_c} = \frac{\delta\epsilon_r|_{r=s}}{E_c} \quad (9.11)$$

The strain / equivalently the normalized deformation in the first layer of web can be written as:

$$\epsilon_\theta = \frac{u}{r_c} = u|_{r=1^{st}layer} = \frac{\delta\sigma_\theta}{E_\theta} - \nu_{\theta r} \frac{\delta\sigma_r}{E_r} = \frac{1}{E_\theta}(\delta\sigma_\theta - \nu_{r\theta}\delta\sigma_r)|_{r=r_c} \quad (9.12)$$

Equating Equation (9.11) and (9.12) and employing the equilibrium expression Equation (9.5) allows the first boundary condition to be written as:

$$\left. \frac{d\delta\sigma_r}{dr} \right|_{r=r_c} = \left(\frac{E_\theta}{E_c} - 1 + \nu_{r\theta} \right) \left. \frac{\delta\sigma_r}{r} \right|_{r=r_c} \quad (9.13)$$

Now, Equation (9.8) is solved using the boundary conditions of Equation (9.13) and Equation (9.10). Hakiel [86] used the finite difference method to numerically approximate the solution of Equation (9.8). The differential equation has non constant coefficients due to the radial modulus being unique within every layer and numerical solution is required. The process of obtaining the solution is similar to the process of adding a new layer. When a layer is added, the incremental stresses are computed in

each layer and then summed with the previous stresses to obtain the current values. The procedure repeats until the final layer is added. The total radial stress in i^{th} lap can be written as:

$$\sigma_{ri} = \sum_{j=i+1}^n \delta\sigma_{rij} \quad (9.14)$$

With obtained radial stresses in each lap and its derivation w.r.to radial location, r , using equilibrium equation from Equation (9.5) tangential stress as a function of radius can be calculated as:

$$\sigma_{\theta} = r \frac{\partial \sigma_r}{\partial r} + \sigma_r \quad (9.15)$$

There are limitations to Hakiel's method. First, the roll is assumed to be a collection of concentric hoops of web and not a spiral which made the problem solvable. Second, the model did not account for the tension loss effect as described in [84]. Both the limitations were overcome by Kandadai et al. [87], Ren et al. [88] and Good et al. [89] respectively. Kandadai et al. [87] and Ren et al. [88] used Abaqus to fully simulate the spiral nature of the web (first limitation of Hakiel's model). By modeling the spiral form, any slippage between layers will be accompanied by changes in the residual winding stresses. Results from Hakiel's model cannot be predicted if the slippage occurs. With further continuous slippage, normal contact forces between layers may increase or decrease. To overcome the second limitation of Hakiel's method i.e. tension loss effect, Good et al. [89] proposed a model especially when dealing with soft materials (low K_2 value). Good's results indicate that the pressures within a wound roll of soft material can be lower than the values predicted by Hakiel's model. Good et al. developed a new outer boundary condition for use with Equation (9.16).

$$\delta\sigma_r|_{r=s} = -\left(T_w + \frac{u}{s}E_{\theta}\right)h/s \quad (9.16)$$

Where u is the displacement in the radial position of the outermost layer. With the addition of a new outer layer, displacement, u will have a negative sign as it is subjected to tension T_w resulting in inward deformation. Displacement, u is assumed to be axisymmetric and effectively decreases the tension in the outer layer which in turn results in lower incremental and total pressures in the wound roll. Hakiel's model did not calculate the layer deformation. To implement the new boundary condition (Equation (9.16)) into Hakiel's model, it is required to estimate the radial deformation, u of the outer layer. Good was successful in incorporating Equation (9.16) into Hakiel's model and validating the improved model through comparison with tested in-roll pressures.

These 1-D winding models provide a valuable understanding of the state of stress within the wound roll, but they all incorporate the assumptions of small linear deformations and strain. These assumptions can be unrealistic for tissue and nonwoven webs. These webs have low in-plane and radial modulus, and it is not valid to assume small deformations. Mollamahmutoulu et al. [90] developed a 1-D winding model based on large deformation theory using the finite element method. The results of this new model agree very well with models that account for tension loss.

Summary

1-D Elastic winding model gives a fundamental understanding of pressure distribution as a function of pressure. The first winding model started with an assumption of linear isotropic material by Gutterman [77]. Later, numerous researches were conducted to develop a robust winding model that can handle anisotropic materials, tension loss effects, slippage between the web layers due to the change in residual winding stresses etc.,. These models have become an effective instrument to improve industry production, mainly through the reduction of winding defects.

9.2. 2 Visco-elastic Winding Models

In the previous section, the material behavior has stresses related to strains through material stiffness which is either constant (i.e. elastic modulus) or depends on the direction (i.e. anisotropic material). The material that is isotropic as a web are anisotropic inside the wound roll i.e. radial direction is softer compared to the tangential direction. Another material behavior comes into play that is time-dependent when the wound roll are stored for a long period called viscoelasticity [91]. It is important to study the viscoelastic behavior of the webs because viscoelastic effects are permanent i.e. the material undergoes permanent change in length, width and thickness.

Viscoelastic behavior of the web was first modelled by Trampusch [23] using Maxwell-Kelvin Constitutive law. The magnetic tape material is assumed to be homogeneous and isotropic, and its viscoelastic behavior is characterized by a four-parameter model as shown in Figure 9.10. Instantaneous elasticity, delayed elasticity and creep can be observed from this model.

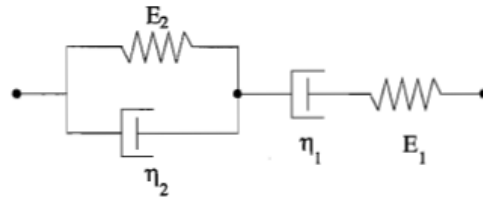


Figure 9.10: Schematic Diagram of four parameter model [23]

The following governing equations were used in polar coordinates:

$$\frac{\partial \sigma_r}{\partial r} + \frac{\sigma_r - \sigma_\theta}{r} = 0 \quad (9.17)$$

$$\epsilon_r = \frac{\partial u}{\partial r}; \epsilon_\theta = \frac{u}{r} \quad (9.18)$$

$$P_1(\phi)S_{ij} = Q_1(\phi)e_{ij} \quad (9.19)$$

$$\sum_{k=1}^3 \sigma_{kk} = 3K \sum_{k=1}^3 \epsilon_{kk} \quad (9.20)$$

$$r = R; \sigma_r = 0 \quad (9.21)$$

$$r = 1; \sigma_r = \frac{u}{g_1 F} \quad (9.22)$$

The equations are written in the order of equilibrium equations, Equation (9.17), strain-deformation equation, Equation (9.18), stress-strain condition, Equation (9.19) & (9.20), and boundary conditions i.e. Outer boundary condition, Equation (9.21) and Inner boundary condition, Equation (9.22). From the inner boundary condition, F is defined as core flexibility. Inner boundary condition provides the continuity of displacement between the innermost layer and core. With the outer boundary condition, the model is confined the value of radial stress to zero which is later proved to be inaccurate in Qualls work [92, 93]. However, the model was able to capture the relaxation of residual stresses in wound roll successfully. The core flexibility was shown to play an important role in controlling the relaxation rate. Given enough time to the wound roll, material was shown to approach stress-free condition. Later, Tramposch extended his viscoelastic model to anisotropic materials [94]. Unequal thermal expansion of core and tape body during environmental temperature changes was analyzed. If deformations are large, errors can become unacceptable which can be a disadvantage in a model based on linear viscoelastic theory.

In 1989, Lin and Westmann [95] developed a viscoelastic winding analysis to model by introducing Generalized Maxwell isotropic viscoelastic model. The histories of winding, winding-pause, and winding-pause-unwinding were considered. The boundary conditions are identical to the ones in Hakiel's 1D model [85]. The expressions for the total stress and displacement fields were given by Equations (9.23)-(9.25).

$$\sigma_r = \sigma_0 \int_{R_i}^{R_0} \frac{\psi(t-\tau)}{(1+\nu)} \left(\frac{1}{R^2} - \frac{1}{R_i^2} \right) dR - \sigma_0 \ln \frac{R_0}{R_i} \quad (9.23)$$

$$\sigma_\theta = \sigma_0 + \sigma_0 \int_r^{R_0} \frac{\psi(t-\tau)}{(1+\nu)} \left(\frac{1}{R^2} - \frac{1}{R_i^2} \right) dR - \sigma_0 \ln \frac{R_0}{R_i} \quad (9.24)$$

$$u = \frac{\sigma_r(1)}{E} + \int_1^r \int_\xi^{R_0} \left[-(1-\nu)J(t-\tau) \frac{\sigma_0}{R} + \int_0^{t-\tau} \left[\frac{(1-\nu)}{(1+\nu)R^2} - \frac{1}{\xi^2} \right] \frac{\psi(\eta)dJ(t-\tau-\eta)}{d(t-\tau-\eta)} d\eta \right] dR d\xi \quad (9.25)$$

Where σ_0 is the initial tension in the tape which is considered a constant value, R_i and R_0 are the inner radius and outer radius, E and ν are the Young's modulus and Poisson's ratio, and $\psi(t - \tau)$ is the solution of the Volterra integral equation of the second kind. The developed relationship between stress and time accounted the analysis of a winding-pause. Different winding speeds can contribute to undesirable creep and relaxation in linear and isotropic materials. However, this model incorporated an assumption that the stress in the outer lap remained constant which would appear inconsistent in a viscoelastic development where the stresses in all layers could be affected by creep.

Qualls and Good [92] developed an orthotropic viscoelastic winding model with a nonlinear radial stiffness that is dependent on interlayer pressure. Generalized Maxwell Model is used to represent the viscoelastic behavior. The wound roll is assumed to be axisymmetric and the process of winding is viewed as the addition of pretensioned hoop concentric hoops of webs on the compliant core. The following governing equations [26-29] were considered in polar coordinates:

$$\text{Equilibrium} : r \frac{\partial \sigma_r}{\partial r} + \sigma_r - \sigma_\theta = 0 \quad (9.26)$$

$$\text{StrainCompatibility} : r \frac{\partial \epsilon_r}{\partial r} + \epsilon_r - \epsilon_\theta = 0 \quad (9.27)$$

$$\text{Strain - Displacement} : \epsilon_r = \frac{\partial u}{\partial r}; \epsilon_\theta = \frac{u}{r} \quad (9.28)$$

$$\begin{aligned} \text{Viscoelastic Constitutive} : \epsilon_r &= \int_0^t \left[J_r(t-t') \frac{\partial \sigma_r}{\partial t'} + J_{r\theta}(t-t') \frac{\partial \sigma_\theta}{\partial t'} \right] dt' \\ \epsilon_\theta &= \int_0^t \left[J_\theta(t-t') \frac{\partial \sigma_\theta}{\partial t'} + J_{\theta r}(t-t') \frac{\partial \sigma_r}{\partial t'} \right] dt' \end{aligned} \quad (9.29)$$

Where $J_r(t)$ is the radial creep function and $J_\theta(t)$ is the circumferential creep function. $J_{r\theta}(t)$ and $J_{\theta r}(t)$ are Poisson creep functions that are analogous to the elastic ratios $-\nu_{r\theta}/E_\theta$ and $-\nu_{\theta r}/E_r$ respectively. Combining the expressions for strains from

Equation (9.29) with equilibrium expression Equation (9.26) and strain compatibility Equation (9.27), the following integral boundary value problem [Equation (9.30)] written as a second order partial differential equation in terms of radial stress, σ_r , radius, r and time, t .

$$\int_0^t \left[J_\theta(t-t') \frac{\partial}{\partial t'} \left(r^2 \frac{\partial^2 \sigma_r}{\partial r^2} \right) + \left(3J_\theta(t-t') + J_\theta(t-t') - J_{r\theta}(t-t') + r \frac{\partial}{\partial r} J_\theta(t-t') \right) \frac{\partial}{\partial t'} \left(r \frac{\partial \sigma_r}{\partial r} \right) + \left(r \frac{\partial}{\partial r} (J_\theta(t-t') + J_\theta(t-t')) + J_\theta(t-t') + J_{\theta r}(t-t') - J_r(t-t') - J_{r\theta}(t-t') \right) \right] \quad (9.30)$$

Central difference approximations is used to simplify the above equation. To solve the problem, generalized Maxwell model from Equation (9.31) is chosen to represent the viscoelastic behavior. It provides instantaneous deformation followed by time-dependent deformation known as creep when subjected to a step change in stress. For orthotropic material, radial and circumferential creep compliance should be defined separately.

$$J(t-t') = J_0 + \sum_{i=1}^N J_i e^{-(t-t')/\tau_i} \quad (9.31)$$

To solve this boundary value problem (Equation (9.30)), two boundary conditions were assigned i.e. inner and outer boundary condition. The inner boundary condition provides continuity of deformation at the core which is given by Equation (9.32). The outer boundary condition is developed by taking strain in the outer layer to be constant and equal to winding stress, T_w , multiplied by the circumferential creep function, J_θ , evaluated at time, $t = 0$. Replacing the circumferential strain with this definition in Equation (9.29), the outer boundary condition can be written as shown

in Equation (9.33).

$$\text{Inner Boundary Condition : } \frac{(\sigma_r)_j}{E_c} = (\epsilon_\theta)_j \quad (9.32)$$

$$\text{Outer Boundary Condition : } T_w J_\theta(0) = \int_0^t \left[J_\theta(t-t') \frac{\partial \sigma_\theta}{\partial t'} + J_{\theta r}(t-t') \frac{\partial \sigma_\theta}{\partial t'} \right] dt' \quad (9.33)$$

Where the j subscript refers to the current time, $t = t_j$. Finite difference approximations of the derivatives were taken in Equation (9.30) and (9.32) resulting in sets of algebraic equations that were solved through time. The model successfully predicted the transient stress profiles of orthotropic viscoelastic materials with nonlinear radial modulus. The only limitation to this model was it did not account for thermal influences. Later in his work [93], Qualls and Good developed thermos-viscoelastic winding models successfully where his work is verified with a low density polyethylene web that is stored at room temperature and elevated temperatures.

In this section, we have seen that winding models for both elastic effect and viscoelastic effect have been successfully developed. Proper selection of boundary conditions, simplification and approximation methods were needed to reach the solution of the equations. The developed viscoelastic winding model is mature and is capable of analyzing the influence of creep in homogeneous webs stored in roll form. For the current research, the viscoelastic winding model developed by Qualls [92] is considered to compute the pressure profile of the imprinted webs in the wound roll through time.

CHAPTER X

RESEARCH OBJECTIVE FOR ROLL-TO-ROLL UV-NIL

The development of Roll-to-Roll(R2R) nanoimprint lithography(NIL) was studied by many authors such as Guo [21], Maury [22], etc. However, there is no research focused on storing the nanoimprinted material once produced in a R2R NIL process. Winding is the only convenient means of storing large quantities of nanoimprinted webs at the end of R2R processes, as they await unwinding for sequential R2R processes with unique transport speeds. Winding imprinted webs will subject the imprinted surfaces to a normal contact pressure. The presented research is concerned with how the contact pressures due to winding affects the imprinted peak heights and potentially the functionality of the UV-NIL surface.

The research objective is to develop a method that predicts the deformation of imprinted surfaces when subjected to contact pressures. The following steps are followed for developing the method:

- Define an experimental method to characterize the viscoelastic UV curable resin considering the phenomenon of dark curing.
- Determine the equivalent material properties of the imprinted web. Webs with resin nano-imprints are simulated to obtain the material properties of the assembly, which are input parameters to a winding model to quantify the contact pressure the imprinted surfaces will be subjected to.

- Quantify the radial contact pressure distribution in the wound roll of nanoimprinted web through time using a viscoelastic winding model.
- Quantify the deformation of the nanofeatures in a wound roll according to time, resulting from the varying radial pressure.
- Validate this method by comparison with experimental data of the creep of an imprinted web under constant pressure.

CHAPTER XI

CHARACTERIZATION OF VISCOELASTIC ULTRAVIOLET CURABLE RESIN

11.1 Viscoelastic rheological model

The viscoelastic behavior of the UV resin is assumed linear and represented by a Generalized Maxwell or Wiechert rheological model (Figure 11.1), where E are the moduli of the springs and η the viscosities of the dampers. In this model, several Maxwell elements, representing the multiple relaxation mechanisms, are connected in parallel to an elastic spring, representing the equilibrium response.

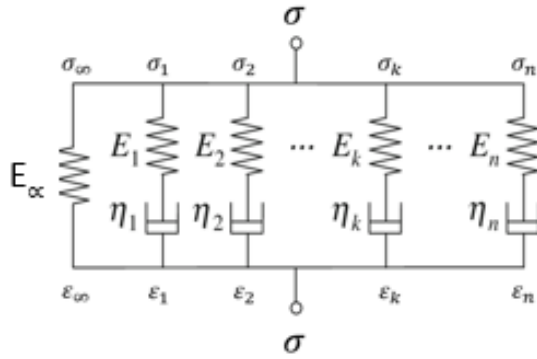


Figure 11.1: Representation of Generalized Maxwell model

The relaxation modulus $E(t)$ is then expressed as a Prony series (Equation (11.1)).

$$E(t) = E_\infty + \sum_{i=1}^n E_i e^{-t/\tau_i} \quad (11.1)$$

Or equivalently,

$$E(t) = E_0 - \sum_{i=1}^n E_i(1 - e^{-t/\tau_i}) \quad (11.2)$$

Where E_∞ , E_0 , and E_i are the relaxation moduli corresponding to the long-term equilibrium modulus, the instantaneous modulus, and the modulus associated to each Maxwell element. By definition, $E_0 = E_\infty + \sum_{i=1}^n E_i$. The relaxation times τ_i indicate a time scale for each relaxation mechanisms in each Maxwell element and are defined by $\tau_i = \eta_i/E_i$. Characterizing the UV curable resin corresponds to experimentally identifying its material parameters, E_0 , E_i , τ_i which are known as Prony series.

11.2 Dark curing

The UV curable resin is, once cured, easily characterized with classical viscoelastic measurements such as Dynamic Mechanical Analysis tests, measuring the storage and loss moduli, which can lead to the identification of the Generalized Maxwell model parameters. For full characterization over large temperature and time scales, a master curve of the viscoelastic behavior can be built, taking advantage of the time-temperature superposition principle verified in linear viscoelastic materials called thermorheologically simple.

Generally, curing of resin with UV radiation is divided into four stages: Induction, vitrification, gelation and post-cured [24]. In UV-NIL process, UV curable resin reaches post-cured stage when it is still in contact with the imprint rollers after the UV exposure. During the post-cured stage, the resin has dark curing effects up to 24 hours (for the UV-15 resin). In other words, the extremely short and high energy UV exposure initiates the crosslinking process but the curing keeps occurring after this exposure and the material properties evolve for a day after curing. This phe-

nomenon, called dark curing, is accentuated by the extremely short time scale of the UV exposure in the nanoimprinting process. Because web handling processes happen at a relatively high speed to increase productivity, the nanoimprinted web will be subject to mechanical loading in a short time after the UV exposure. Consequently, the material properties of the resin need to be quantified as a function of the dark curing time.

This complexifies the characterization process by introducing a second dimension (dark curing time) added to the usual time/temperature dimension in linear viscoelastic materials. In other words, instead of building a master curve, we need to build a master surface. Finally, the viscoelastic time and the dark curing time are conflicting with each other during testing. On the one hand, the time-temperature principle applies to the temperature and the viscoelastic time and is specifically conditioned by the material not undergoing any physical change. On the other hand, the dark curing time evolves on the same time scales as the viscoelastic time and specifically implies a change in the material physical structure, which influences the material properties. Consequently, there is here a need for a characterization experimental method that can decouple those two times.

11.3 Characterization in stress relaxation

As explained in the section 6.1, stress relaxation and creep test are two tests generally used for the characterization of viscoelastic material properties. In the present study, a stress relaxation test was performed. In stress relaxation tests, constant strain (ε) is applied quasi-statically to avoid any dynamic effects on a specimen for a particular duration as shown in Figure 11.2. Equation (11.3) shows the calculation of strain, ε . The resulting stress as a function of time is measured. The stress needed to maintain the strain constant decreases gradually and reaches a constant value as shown in

Figure 11.3. Relaxation modulus as a function of time, $E(t)$ and Equilibrium modulus, E_0 can be calculated using Equation (11.4).

$$\varepsilon = \frac{\Delta L}{L} \quad (11.3)$$

Here, L is the length of specimen and ΔL is the change in length due to applied load.

$$\begin{aligned} E(t) &= \frac{\sigma(t)}{\varepsilon_0} \\ E_0 &= \frac{\sigma(t=0)}{\varepsilon_0} \end{aligned} \quad (11.4)$$

Here, $\sigma(t)$ is the stress as a function of time; ε_0 is the constant strain that is maintained during test; $\sigma(t=0)$ is the initial stress at the start of stress i.e. at $t=0$

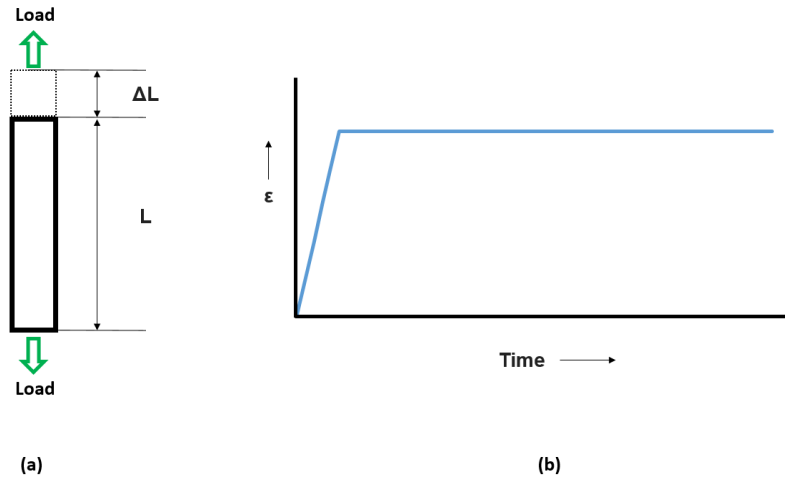


Figure 11.2: (a) Specimen subjected to loading; (b) Cause of Stress relaxation test i.e. applied strain Vs. time

In the present study, a tensile stress relaxation experiment has been performed on a rectangle shaped specimen in an Instron tensile machine (Instron 5965) with a load cell of 5 kN. Since the UV15 material is a liquid resin, the specimen preparation is shown below using a mold.

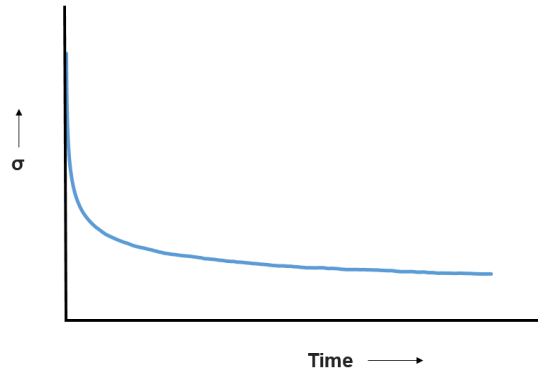


Figure 11.3: Effect of Stress relaxation test i.e. resulting stress Vs. time

SPECIMEN PREPARATION: The Teflon material is chosen for the mold material and the specimen of rectangle shape with a size of 9.6 mm width, 40 mm height and 1.4478 mm thickness is made on the mold with milling operation as shown in the Figure 11.4 (b). The mold is filled with UV15 resin using a pipette filler with rubber bulb and make sure there is no air bubble. Once the mold is filled uniformly with UV15 resin, it is exposed to ultraviolet (UV) light at an intensity of 185 mW/cm^2 for 6 seconds as shown in Figure 11.4(a). This 6 seconds is referred to as curing time. Once the specimen is cured, it becomes rubbery elastic material (figure 11.4) which is used as specimen for performing stress relaxation test.

Once the specimen is prepared, it is immediately taken to the Instron tensile machine where it is subjected to tensile stress relaxation test at a constant strain of 0.02 for 86400 seconds as shown in the Figure 11.5. The stress relaxation in response to this constant strain hold is measured and the relaxation modulus $E(t)$ is computed using Equation (11.4) as the ratio of the measured stress and the imposed strain through time. This test is repeated two times to make sure the relaxation modulus values are repeated. Figure 11.6 shows the relaxation modulus through time for two test and their values are quite close. Therefore, the test values are considered to be valid.

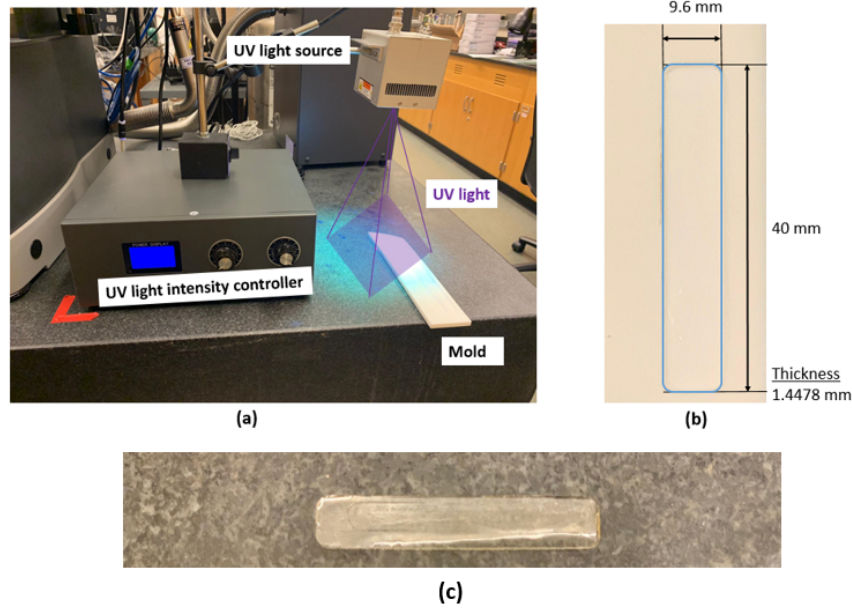


Figure 11.4: (a) UV light setup with mold on which UV light is exposed; (b) Geometry of the mold; (c) The specimen

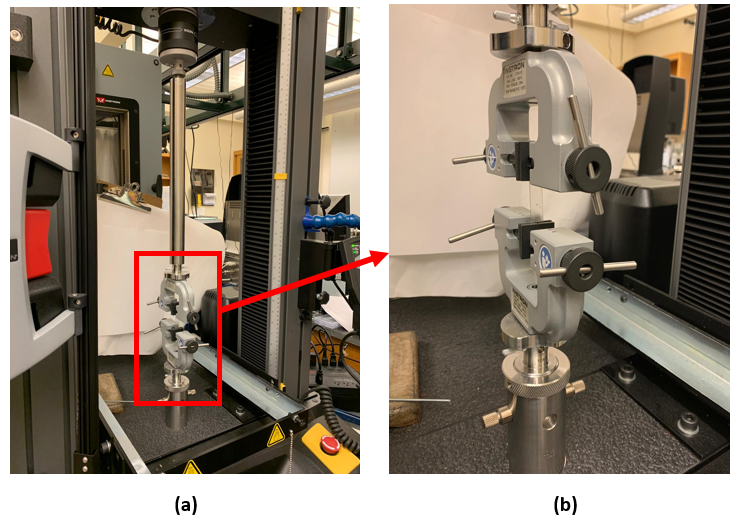


Figure 11.5: (a) Setup of stress relaxation test on Instron tensile machine; (b) Close view of specimen that is subjected to testing

The viscoelastic behavior of the UV resin is assumed linear and represented by a Generalized Maxwell or Wiechert rheological model (Figure 11.1), where E are the moduli of the springs and τ are the viscosities of the dampers. In this model, several Maxwell elements, representing the multiple relaxation mechanisms, are connected in parallel to an elastic spring, representing the equilibrium response.

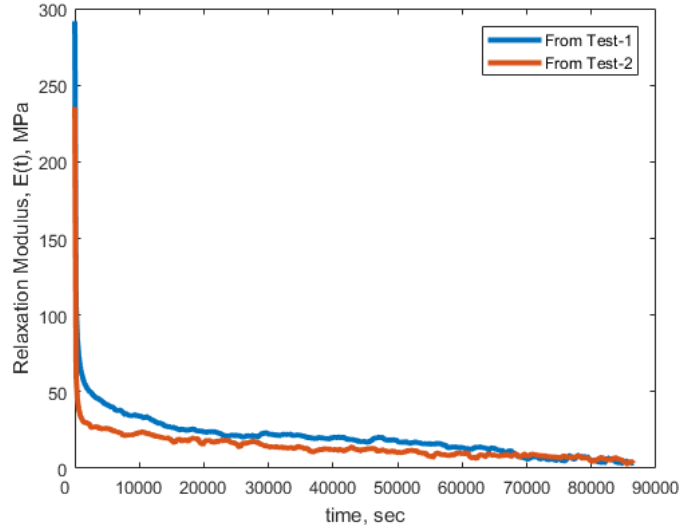


Figure 11.6: Relaxation modulus, $E(t)$ as a function of time

From the experiment results (Figure 11.6), the relaxation modulus, $E(t)$ up to 10,000 seconds was enough to represent the Generalized Maxwell model. Therefore, the coefficients of the Prony series representing the relaxation modulus are fitted on the data (Figure 11.7) and converted to shear moduli through equation (11.5).

$$G(t) = \frac{E(t)}{2(1 + \nu)} \quad (11.5)$$

Where ν is the Poisson's ratio and is assumed constant.

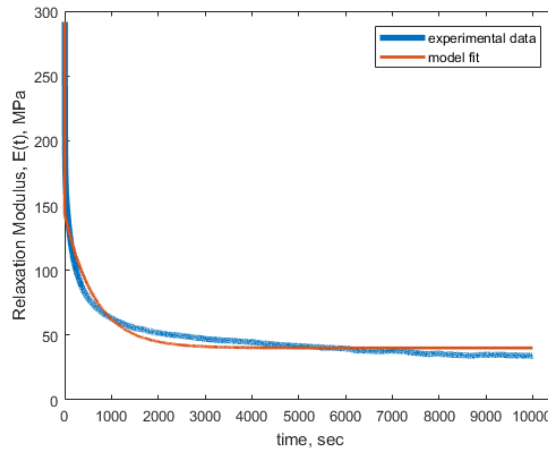


Figure 11.7: Relaxation modulus and Prony series fitted on the data

The Finite element software Abaqus requests the viscoelastic parameters to be entered as a ratio of the instantaneous modulus which is calculated using Equation (11.6) (Table 11.1). Here, instantaneous modulus, E_0 is 291.7 MPa.

Table 11.1: Coefficients of the Prony Series representing the relaxation modulus

g_i	τ_i , seconds
0.4652	12.29
0.305654	288.4
0.122419	3914

$$g_i = \frac{G_i}{G_0} = \frac{\frac{E_i}{2(1+\nu)}}{\frac{E_0}{2(1+\nu)}} = \frac{E_i}{E_0} \quad (11.6)$$

This characterization highly depends on the dark curing amount and speed and hence, cannot be transferred to another curing protocol. Consequently, we developed a more complex experimental procedure allowing for the characterization of the viscoelastic properties of the material at any point during any dark curing.

11.4 Dynamic mechanical analysis characterization considering dark curing period

We designed a method specifically addressing the concerns raised by the presence of substantial dark curing in the UV resin. The experiments are performed using a Dynamic Mechanical Analysis apparatus (TA Instruments RSA-G2). The time decoupling is achieved by using the normal time scale as the dark curing time and the frequency of the imposed strain sinusoidal waves as the viscoelastic time.

A specimen of resin of 30 mm length, 9.6 mm width and 1.4478 mm thickness is placed in the apparatus right after UV exposure (6 seconds). An arbitrary wave $\varepsilon(t)$

combining multiple sinusoidal signals of varying frequency (Equation 11.7) is imposed to the material for a period of 60 minutes.

$$\varepsilon(t) = \sum_{i=1}^N a_i \sin(2\pi f_i t) \quad (11.7)$$

Where f_i and a_i are the chosen frequencies and corresponding signal amplitude constants. The coefficients defining the imposed wave are $a_i = 0.05$ % for all terms and $f_1 = 1$ Hz, $f_2 = 5$ Hz, $f_3 = 10$ Hz, and $f_4 = 15$ Hz. The constants a_i have been chosen to lead to a maximum strain amplitude of the wave of 1%.

During these 60 minutes, dark curing occurs in the resin, influencing its stress response to the arbitrary strain wave. The stress is continuously recorded through time. By definition of linear viscoelasticity, the stress response will be of the form

$$\sigma(t) = \sum_{i=1}^N b_i \sin(2\pi f_i t + \delta_i) \quad (11.8)$$

The stress signal is then processed in MATLAB with a Fast Fourier Transform to isolate the response to each frequency and determine the norm of the complex modulus $\|E_i^*\| = b_i/a_i$, and loss factor $\tan(\delta_i)$.

From the norm of the complex modulus and the loss factor, one can compute the storage modulus E' and the loss modulus E'' , which are material properties fully characterizing the viscoelastic behavior. Finally, the coefficients of the resin relaxation modulus can be identified from the storage and loss moduli using Equation (11.9) and (11.10).

$$E'(\omega) = E_\infty + \sum_{i=1}^n \frac{E_i \omega^2 \tau_i^2}{1 + \omega^2 \tau_i^2} \quad (11.9)$$

$$E''(\omega) = \sum_{i=1}^n \frac{E_i \omega \tau_i}{1 + \omega^2 \tau_i^2} \quad (11.10)$$

where ω is the angular frequency.

Experiments with the above discussed test method were performed on UV15 resin for all frequencies between 1 and 15 Hz at room temperature. Specimen used for these experiments are prepared similarly to the ones in section 11.3. This experiment is repeated at elevated temperatures of 30°C and 40°C. During the test, stress and strain were measured. Due to a relatively low data acquisition frequency necessary to record data during an hour, the frequency was limited to 15 Hz.

After processing the test data in MATLAB, the complex modulus and loss factor for different dark curing times according to frequency are plotted for each temperatures as shown in Figure 11.8. Complex modulus increases with dark cure time and loss factor decreases with dark cure time, represented by the arrow direction on right to each plot in Figure 11.8.

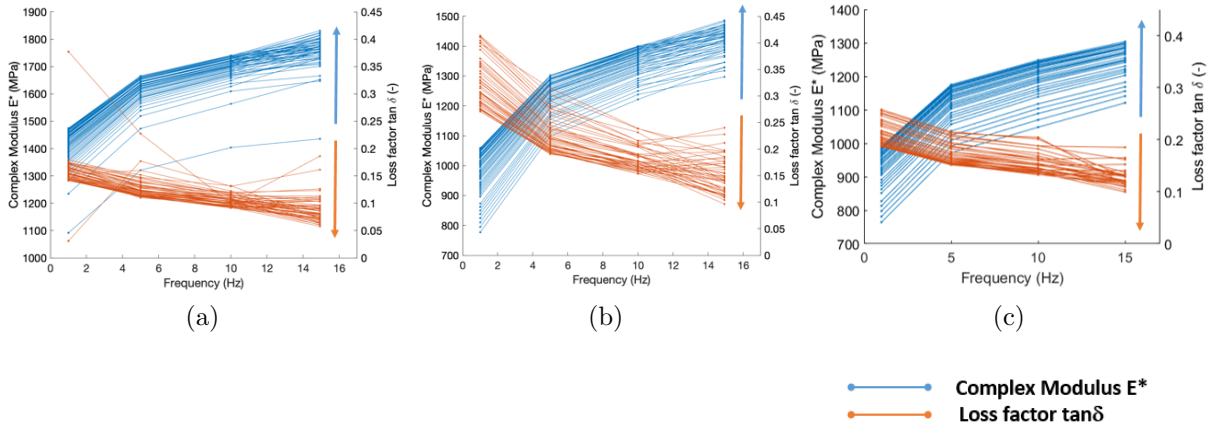


Figure 11.8: Evolution of the norm of the complex modulus and loss factor of the resin during dark curing with frequency as X-axis at temperature (a) 23°C (b) 30°C (c) 40°C

From Figure 11.8, the complex modulus did not increase much for elevated temperatures through dark cure time compared to the room temperature (23°C). Converting the 2D plots from Figure 11.8 to 3D plots with frequency as X-axis, dark cure time as Y-axis and norm of complex modulus as Z-axis, the behavior of the

resin for different frequencies through dark cure time at different temperatures is monitored as shown in Figure 11.9(a). The master curve with 23°C as reference temperature is shown in Figure 11.9(b). With increased temperature, the modulus reached equilibrium at short times meaning dark curing occurs much faster at the higher temperatures (Figure 11.8 (b) & (c)).

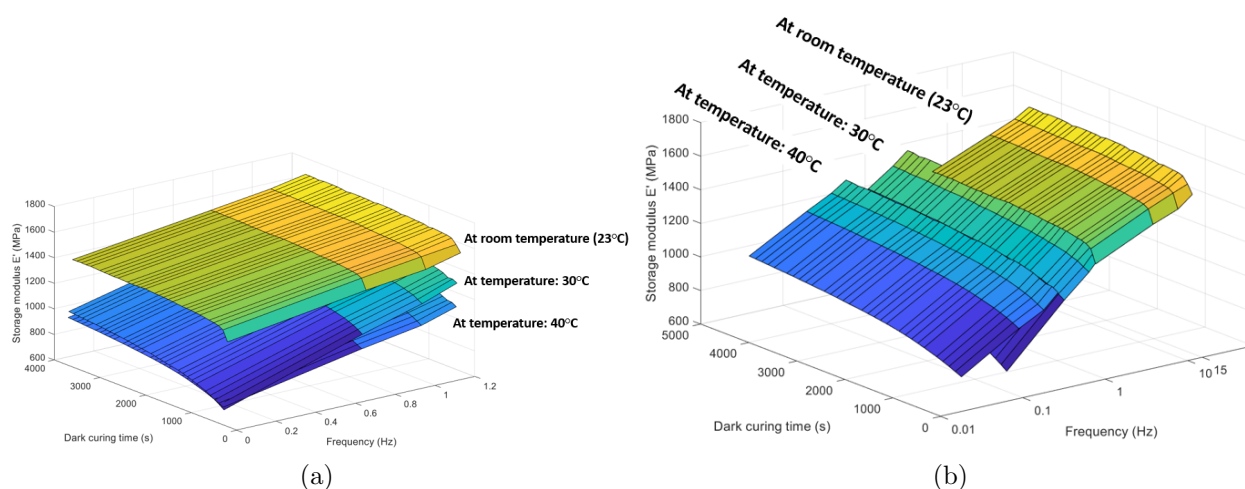


Figure 11.9: (a) Evolution of the norm of the complex modulus of the resin during dark curing for all the temperatures (a) 23°C (b) Master curve

The specimen used for these experiments is cured in the Teflon material mold. From the tests performed by Ron Markum and Xin Chen at Web Handling Research Center [96], it is observed that the resin has a faster curing reaction rate when cured in Teflon mold compared to a rubber mold. The curing kinetics is accelerated at elevated temperatures leading the resin, which already has fast curing rate, to be completely cured in short period. Hence, dark curing is not observed for the elevated temperatures as shown in Figure 11.9. Although this test provides a more exact characterization of viscoelastic properties, it did not provide a better characterization of the material during dark curing due to the use of a Teflon mold and the resulting very short dark curing period. Due to lack of time, this direction is not further pursued in this work and the stress relaxation characterization is used to build the

model.

This testing method will be better for characterizing resin considering dark curing with certain changes such as:

- curing specimen in mold that gives low curing reaction rate like rubber and wax material
- setup test in such a way that specimen can be cured on testing machine to shorten the time between end of curing and start of test.

CHAPTER XII

EQUIVALENT MATERIAL PROPERTIES FOR THE IMPRINTED WEB

In this section, the equivalent material properties that are required input parameters to the winding model are estimated using finite element analysis. Parameters such as radial and circumferential modulus, radial and circumferential relaxation/creep function are required inputs to the viscoelastic winding model. The circumferential parameters are likely to be dominated by the machine direction (MD) properties of the web. Therefore, the MD modulus of the web represents the circumferential modulus of the imprinted web, E_θ . UV-NIL processes are likely to occur on high modulus webs such as PET or PEN, which do not creep or relax readily at room temperature. So, we assume that there is no viscoelastic relaxation or creep in circumferential direction.

The remaining input parameters i.e. radial modulus, E_r and radial relaxation or creep function are estimated in the following sections. The equivalent radial modulus E_r in the winding model is not a material property, it encompasses a combination of material and geometric contact nonlinearity.

12.1 The pressure-dependent radial modulus

The radial modulus, E_r is state-dependent on the normal pressure. Because the surface of uncoated webs is rarely both smooth and flat, the real area of contact

between two layers can be very low under low pressures. However, the area of contact increases with pressure. In Equation (12.1), P is described as the apparent pressure. The real area of contact will be less than the apparent area and the nano-imprints that first contact an adjacent web in a wound roll will be subject to concentrated localized pressures. The relationship between apparent pressure and strain is [83]:

$$P = K_1(e^{K_2\varepsilon} - 1) \quad (12.1)$$

Where P is the radial pressure, ε is the normal strain, and K_1 and K_2 are constants determined experimentally by subjecting a stack of web to an increasing pressure P while measuring ε in the stack. Web materials with low surface roughness would exhibit very high K_2 numbers. With known values of K_1 and K_2 , the radial modulus is estimated using:

$$E_r = \frac{dP}{d\varepsilon} = K_2(P + K_1) \quad (12.2)$$

Although on universal, Equations (12.1) and (12.2) have been demonstrated to represent the behavior of many webs with varying engineered surface roughness.

12.2 Analytical determination of the equivalent radial modulus for nano-imprinted web

The web with nanoimprints is represented by a three-layer model (Figure 12.1). The blue portion represents the UV cured resin imprint and the gray portion represents the web. The resin portion is divided into two parts, the nanoimprints and the base.

The dimension b_f is the width of bottom side of the nano-imprint; b_h is the width

of top side of the nano-imprint; b_v is the distance between the two nano-imprints; h is the thickness of the nano-imprint; h_0 is the thickness of the nano-imprint base; h_1 is the thickness of the web. The resin nanoimprints, the resin base, and the web are modeled with springs of stiffness K_n , K_b , and K_w , respectively. A trapezoidal-shaped nano-imprint is considered as a general case because it corresponds to square- and rectangle-shaped nano-imprints when $b_I = b_h$ and triangle-shaped nano-imprints when $b_h = 0$. The stiffness of each spring is calculated using Equation (12.3).

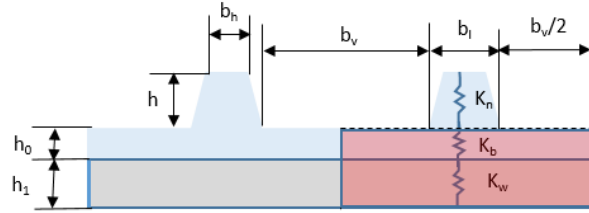


Figure 12.1: Pictorial representation of a nano-imprinted web

$$\begin{aligned}
 K_n &= \frac{E_1 b_I}{h} \quad \text{when } b_h = b_I \\
 &= \frac{E_1 (b_h - b_I) W}{h [\log(b_h E_1 h W) - \log(b_I E_1 h W)]} \quad \text{when } b_h \neq b_I \\
 K_b &= \frac{E_1 (b_I + b_v)}{h_0} \\
 K_w &= \frac{E_2 (b_I + b_v)}{h_1}
 \end{aligned} \tag{12.3}$$

Where E_1 is the Young's modulus of the resin, and E_2 is the Young's modulus of the web. The equivalent stiffness, K_{eq} , is calculated as:

$$\frac{1}{K_{eq}} = \frac{1}{K_n} + \frac{1}{K_b} + \frac{1}{K_w} \tag{12.4}$$

The total stiffness K_{total} can be estimated by multiplying the equivalent stiffness with the number of equivalent springs (Equation (12.5)). The width of the entire model is assumed to be 1 mm. and the depth, i.e. height of the model, is also

assumed to be 1 mm^2 , which leads to a cross-sectional area A of 1 mm^2 . The material properties for the web and resin are shown in Table 12.1.

$$K_{total} = N * K_{eq} \quad (12.5)$$

Where $N = \frac{1}{b_I + b_v}$.

For an applied load P , the displacement U , stress σ and strain ε can be calculated:

$$U = \frac{P}{K_{total}} \quad (12.6)$$

$$\sigma = \frac{P}{A} \quad (12.7)$$

$$\varepsilon = \frac{U}{h + h_0 + h_1} \quad (12.8)$$

The equivalent radial modulus, E_r , can be calculated by:

$$E_r = \frac{\sigma}{\varepsilon} \quad (12.9)$$

This is the radial modulus as a response to a small pressure step. To determine the pressure-dependent radial modulus, we will use finite element simulations.

12.3 Numerical determination of the equivalent radial modulus for a nano-imprinted web

A Finite Element analysis with Abaqus is performed on a similar model for four geometries of nanoimprints. The shapes of the nano imprints are shown in Figure 12.2.



Figure 12.2: Imprint geometry cases 1,2,3, and 4

- Case-1: Trapezoidal shaped nano-imprint $h = 0.0001$ mm; $h_0 = 0.0001$ mm; $h_1 = 0.1016$ mm; $b_h = 0.00008$ mm; $b_l = 0.0001$ mm; $b_v = 0.0001$ mm.
- Case-2: Trapezoidal shaped nano-imprint with $b_v = 0$ $h = 0.0001$ mm; $h_0 = 0.0001$ mm; $h_1 = 0.1016$ mm; $b_h = 0.00008$ mm; $b_l = 0.0001$ mm; $b_v = 0$
- Case-3: Square shaped nano-imprint $h = 0.0001$ mm; $h_0 = 0.0001$ mm; $h_1 = 0.1016$ mm; $b_h = 0.0001$ mm; $b_l = 0.0001$ mm; $b_v = 0.0001$ mm.
- Case-3: Square shaped nano-imprint with $b_v = 0$ $h = 0.0001$ mm; $h_0 = 0.0001$ mm; $h_1 = 0.1016$ mm; $b_h = 0.0001$ mm; $b_l = 0.0001$ mm; $b_v = 0$

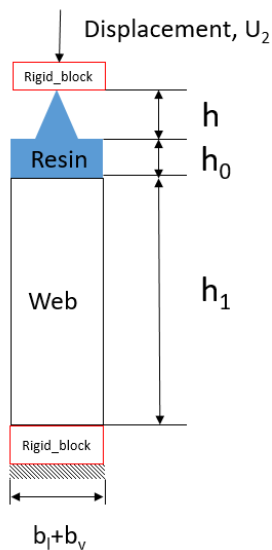


Figure 12.3: Nano-imprinted web model and boundary conditions.

In the numerical analysis model (Figure 12.3), the web with nano-imprinted resin is subjected to a displacement of 30 nm between two rigid blocks. The bottom block is confined in the all directions. The shape and geometry of the resin is changed for corresponding cases as mentioned above. The material properties used for the web (PET material) and resin are detailed in Table 12.1.

Table 12.1: Material Properties

Web Material Properties:	Elastic: $E = 4136.85$ MPa; $\nu = 0.3$
Resin Material Properties:	Elastic: $E = 20.7$ MPa; $\nu = 0.49$

The numerical radial modulus is compared with the analytically calculated value in Table 12.2.

Table 12.2: Radial Modulus for different Cases

	Analytical E_r	Numerical E_r
Case-1	1323.61 MPa	1532.6 MPa
Case-2	1364.81 MPa	1639.5 MPa
Case-3	1243.72 MPa	1561.1 MPa
Case-4	1321.06 MPa	1628.6 MPa

The numerical values are in good agreement with the analytical calculations. Consequently, the numerical model can be used to predict the coefficients of the radial modulus i.e. K_1 and K_2 from Equation (12.2).

To account for the geometric nonlinearity in the contact zone, triangle-shaped nano-imprints are considered. Initially, the triangle-shaped nano-imprints form a line contact with the web. Once the load is applied, the contact becomes a surface contact.

The stress-strain plot (Figure 12.4) representing the response of the model to the

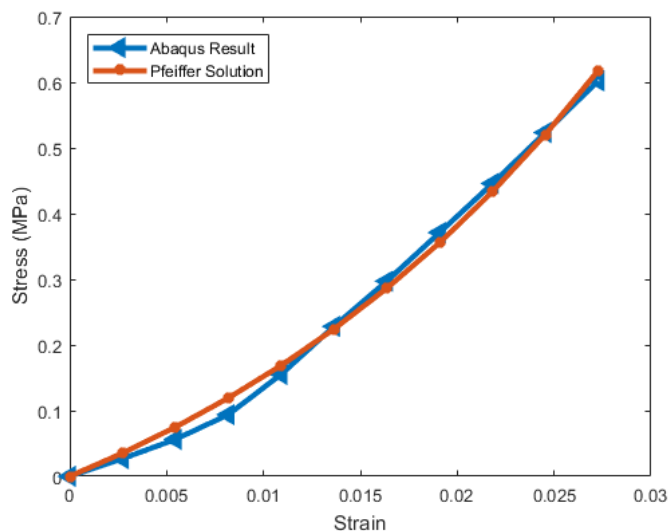


Figure 12.4: Stress-strain curve of the imprinted web in response to a uni-axial pressure.

loading is extracted and the coefficients K_1 and K_2 are fitted. The coefficient K_1 is equal to 0.297 MPa and K_2 to 41.237.

12.4 Equivalent radial viscoelastic functions for a nano imprinted web

Viscoelastic winding models require either the creep function or the relaxation modulus to determine the pressure in the wound roll through time. The anisotropic viscoelastic properties are considered constant through the web thickness. As the web exhibits little viscoelastic behavior, the creep or relaxation will be dominated by radial terms involving the compression of the cured UV resin nanoimprints. Similarly to the previously-discussed effective radial modulus, the effective radial creep function or relaxation modulus depends on a combination of material properties and geometric nonlinearity. The highest imprinted asperities will be subjected to the largest pressures. The imprint geometry will result in the creep or relaxation being larger than would be produced with a uniform layer of cured resin on a web.

In this section, the equivalent creep function of the nano-imprinted web is deter-

mined by simulating a creep test on the numerical model. The viscoelastic material properties of the resin determined in section 11.3 are introduced in the model. The web is considered elastic. A constant uniaxial compressive load is imposed to the model (figure 12.5).

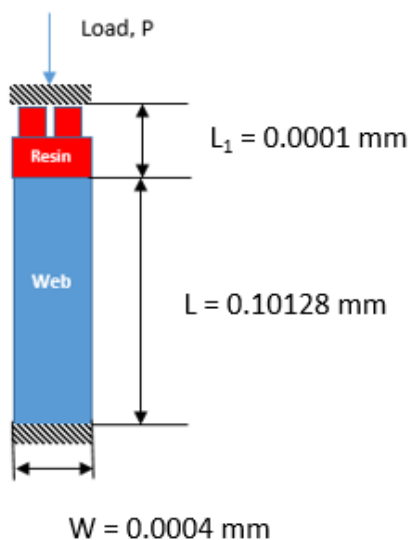


Figure 12.5: Dimensions and boundary conditions of the numerical creep model.

The uniaxial strain $\varepsilon(t)$ and constant stress σ are computed from the time-dependent displacement and the reaction forces (Equation (12.10) & (12.11)).

$$\varepsilon(t) = \frac{\textit{displacement}}{L + L_1} \quad (12.10)$$

$$\sigma = \frac{\textit{Reaction force}}{w} \quad (12.11)$$

The creep compliance, defined by the ratio of the strain and the stress, characterizes the viscoelasticity of the imprinted web (Figure 12.6).

Similarly to the relaxation modulus defined in section 11.1, the creep compliance

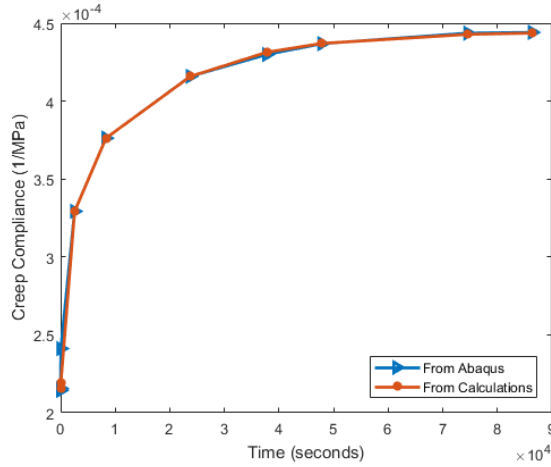


Figure 12.6: Creep compliance of the imprinted web.

can be expressed as a Prony series (Equation (12.12)).

$$J(t) = J_0 + \sum_{i=1}^n J_i(1 - e^{-t/\tau_i}) \quad (12.12)$$

The coefficients of the Prony series are identified by fitting the obtained compliance curve (Table 12.3). In order to use the creep compliance coefficients in the

Table 12.3: Prony Series representing the creep viscoelastic behavior

2-term Prony Series			
Units:	1/MPa		seconds
J_0	2.279E-04		
J_1	1.107E-04	τ_1	994.1
J_2	1.291E-04	τ_2	9977

winding model, Equation (12.12) is modified as follows:

$$\begin{aligned}
 J(t) &= J_0 + \sum_{i=1}^n J_i(1 - e^{-t/\tau_i}) \\
 &= J_0 + \sum_{i=1}^n J_i - \sum_{i=1}^n J_i(e^{-t/\tau_i}) \\
 &= J_0 + \sum_{i=1}^n J_i e^{-t/\tau_i}
 \end{aligned} \quad (12.13)$$

with $JJ_0 = J_0 + \sum_{i=1}^n J_i$ and $JJ_i = -J_i$

JJ_0, JJ_i and τ_i are used as viscoelastic input in the winding model.

CHAPTER XIII

ESTIMATING THE PRESSURE AND DEFORMATION OF THE NANOIMPRINT IN THE WOUND ROLL

13.1 Radial pressure in the wound roll

Winding is a necessary component in scaling UV-NIL processes to production using R2R methods. Winding models have been developed by the Web Handling Research Center to predict in-roll pressure and tangential stresses as a function of roll radius. For the present research, a viscoelastic winding model [92] is used to determine the influence of the viscoelasticity of the resin on the web. The in-roll pressures are expected to be quite high and, when coupled with the viscoelasticity of the imprinted resin, will result in deformation of the imprinted surface.

Using the input parameters from the Table 13.1, pressures resulting from winding are computed at different radial locations (Figure 13.1).

As the curves for the radial stress at different times are superimposed, the radial stress did not decrease with time, indicating the viscoelastic behavior of the nano-imprints did not influence the radial stress in the wound roll.

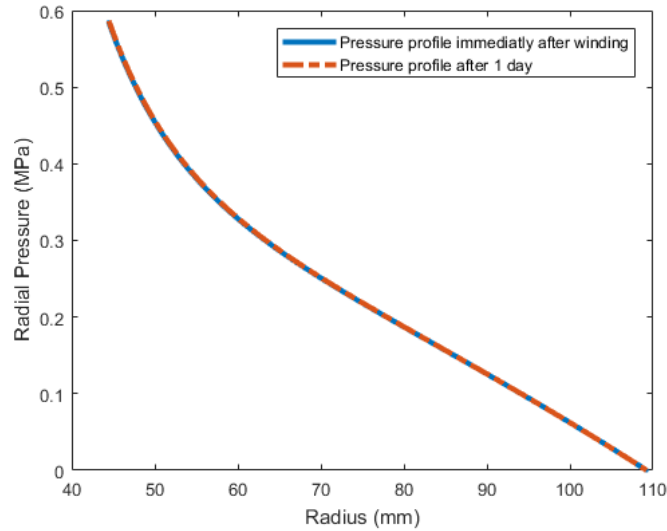


Figure 13.1: Radial stress profile according to time

Table 13.1: Input Parameters for the winding model

Winding Parameters:				
Winding Tension		1.17211 MPa		
Inner Wound Roll (core)	Inner diameter	76.2 mm		
	Outer diameter	88.9 mm		
Outer Wound Roll Diameter		218.44 mm		
Web layer thickness		0.1016 mm		
Material Properties:				
Poisson's ratio		0.37		
CMD Modulus		4826.33 MPa		
Core material modulus		689475.7293 MPa		
Function Coefficients	K_1	0.297 MPa		
	K_2	41.237		
Relaxation Viscoelastic Properties in radial direction	Units:	1/MPa		Seconds
	J_0	4.677E-04		
	J_1	-1.107E-04	τ_1	994.1
	J_2	-1.291E-04	τ_2	9977

13.2 Deformation of the nanoimprints in the wound roll

However, the constant pressure in the wound roll does not mean the nano-imprints exhibit a constant deformation. The deformation at different radial locations through

time is estimated.

$$\varepsilon(t) = \sigma_0 \times J(t) \quad (13.1)$$

Where σ_0 is the radial stress and $J(t)$ is the compliance of the imprinted web. Substituting $J(t)$ from Equation (12.12),

$$\varepsilon(t) = \sigma_0 \times \left[J_0 + \sum_{i=1}^n J_i(1 - e^{-t/\tau_i}) \right] \quad (13.2)$$

Therefore, the displacement of the imprinted web is:

$$u(t) = (L + L_1) \times \sigma_0 \times \left[J_0 + \sum_{i=1}^n J_i(1 - e^{-t/\tau_i}) \right] \quad (13.3)$$

Where L and L_1 are dimensions detailed in Figure 12.5. It is assumed that the deformation of the imprinted web is largely situated in the soft resin nanoimprints. The deformation of nano-imprint at different radial locations vary with time (Figure 13.2). With time, the nano-imprint is deformed from 15 nm to 27 nm at the core location, corresponding to 15 and 27% strain for 100 nm height nano-imprints.

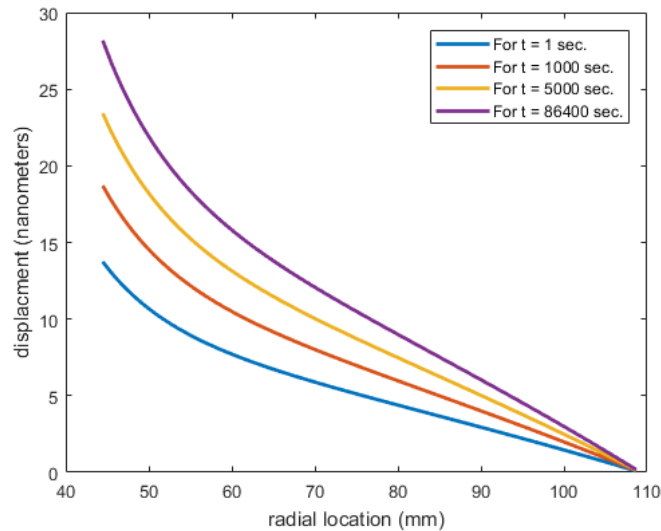


Figure 13.2: Pressure-induced displacement of the nano-imprints

CHAPTER XIV

VALIDATION TEST

14.1 Validation test at the nanometer scale

To validate the numerical method developed for estimating the deformation of nanoimprinted web when subjected to winding, the initial plan is to subject nano-imprinted surfaces to a constant mean pressure and make Atomic Force Microscope (AFM) measurements before, after, and at intermediate times to capture the viscoelastic deformation at various times. Results from these tests would validate the developed method. This experiment plan involved three steps:

1. Measure the average peak height of the nano-imprints through AFM before subjecting it to any loading.
2. Subject the stack of nano-imprinted webs to a constant contact pressure for sufficient time to induce creep.
3. Measure the deformed height of the nano-imprint using AFM at various times after creep, during recovery.

Preliminary experiments showed serious flaws in this procedure. First, it proved harder than expected to place the AFM tip at exactly the same location before and after loading. As the imprinted web is not perfectly regular, this affects the possible comparison of peak heights. Second, it takes 30 minutes to perform an AFM

scan grating on a $5 \mu\text{m} \times 5 \mu\text{m}$ region after calibration. This calibration entails positioning the tip at the relevant height compared to the material surface. As this surface baseline height keeps moving up through recovery of the creep deformation, it prevents a proper AFM measurement. We were expecting height differences of the order of a few nanometers, a resolution that could not be reached with this experimental method. Therefore, the validation test is moved to the millimeter scale as described in the following section.

14.2 Validation test at the millimeter scale

To validate the numerical method, an imprinted surface in the scale of millimeters will be subjected to a constant mean pressure in a tensile machine. The deformation of the imprinted surface is measured and compared with the computational results.

14.2. 1 Theoretical equivalence of conversion degrees

UV15 resin material used in the computation of the nanoimprinted web, to estimate its deformation when subjected to wound roll pressures, has been characterized by performing stress relaxation test. Consider the stress relaxation test as case-S. The creep test performed on imprinted surface to measure the resin deformation is considered to be case-C. The geometry and curing conditions of specimens used for case-S and case-C are shown in Table 14.1. In order to compare the deformation of imprinted resin from case-C and computational results using case-S, the curing conversion of the corresponding specimen should be similar when subjected to testing. Since the specimen used in case-C test has a higher thickness and different curing than the specimen used in case-S test, a literature survey is conducted to understand the effect of UV intensity, exposure time, thickness, and dark curing time on curing kinetics, dark

curing, and final conversion. This will help in estimating the dark cure time *i.e.* time between the cure of specimen and start of test required for case-C specimen to attain the similar cure conversion to the case-S specimen conversion value at the start of the test. It is observed that the rate of curing reaction varies with the mold in which resin is cured from tensile tests performed by Ron Markum and Xin Chen [96] at Web Handling Research Center and so the dark curing kinetics is studied for two mold cases *i.e.* Rubber mold and Teflon mold.

Table 14.1: Geometry and Curing condition of the tests

	<u>Case-S</u>	<u>Case-C</u>
• Specimen:	rectangular strip	Web with resin imprinted surface
• Mold material:	Teflon	Wax
• Thickness:	1.3 mm	4-6 mm
• Temperature:	23°C	23°C
• UV intensity:	185 mW/cm^2	97 mW/cm^2
• Exposure time:	6 seconds	8 seconds
• Dark curing time:	60 seconds	Need to find

Data collected from the literature is broken down into three steps for estimating dark cure time for the case-C test specimen:

- **Step-1:** Compute the degree of conversion of the resin at the end of curing for case-S and case-C.
- **Step-2:** Determine dark curing kinetics from tensile tests for each mold.
- **Step-3:** Estimate the dark curing conversion for case-S and the time to reach equivalent conversion in case-C.

Step-1: Golaz [24] estimated the curing conversion for different specimen thickness which are cured at UV intensity 17 mW/cm^2 and 50 mW/cm^2 with three exposure times, 100 sec, 200 sec and 300 sec using Equation (14.1),

$$\bar{\alpha}|_{\lambda,i} \propto \left(\frac{I_0(1 - e^{-\mu h})}{\mu h} \right)^\beta \quad (14.1)$$

Equation (14.1) predicts $\bar{\alpha}$ for any specimen thickness, if $\bar{\alpha}$ is known for one thickness (figure 14.1). Extrapolating the μ and β values from figure 14.1, the parameters are obtained for the curing condition: UV intensity 97 mW/cm^2 and exposure time 8 seconds; UV intensity 185 mW/cm^2 and exposure time 6 seconds.

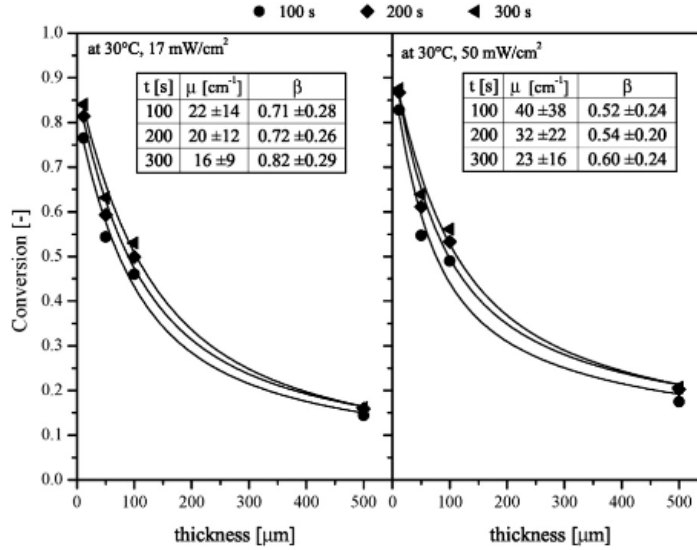


Figure 14.1: Conversion versus thickness for two UV intensities (17 mW/cm^2 , 50 mW/cm^2) and exposure time 100 sec, 200 sec and 300 sec. [24]

From the errors in the coefficients shown in Figure 14.1, μ and β do not necessarily vary with respect to intensity or exposure time. In three papers [97, 24, 98], researchers agree that the conversion is proportional to I^β . Golaz [24] estimated β to be between 0.52 and 0.82 with huge error bars. Two publications [97, 98] mentioned that β is 0.5, although it seems to work better for one resin than the other in [98]. Consequently, we will assume that β is independent on intensity or exposure time and $\beta = 0.5$.

μ is assumed to depend on intensity and exposure time. By extrapolating Golaz's values with respect to time and intensity as shown in Figure 14.2, $\mu = 80.59 \text{ cm}^{-1}$, 142.261 cm^{-1} for intensity 97 mW/cm^2 , exposure time 8 seconds and intensity 185 mW/cm^2 , exposure time 6 seconds, respectively, as shown in Figure 14.2.

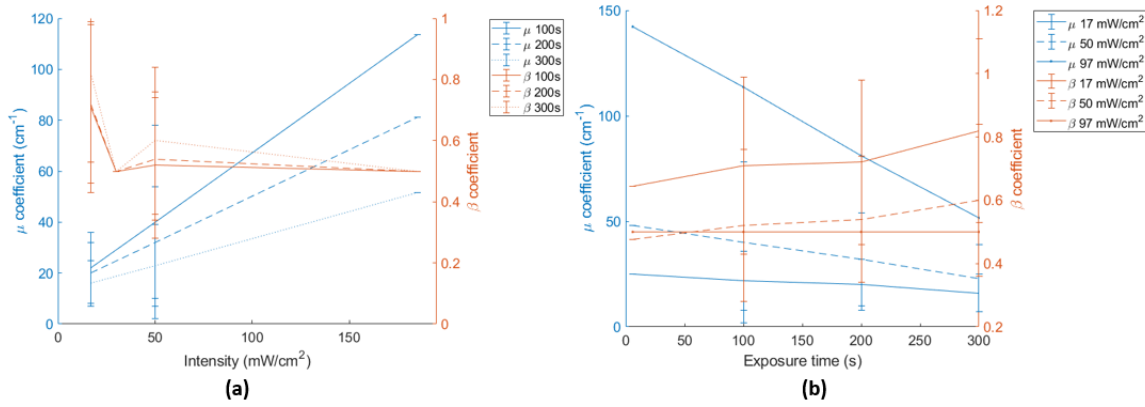


Figure 14.2: μ and β parameters versus (a) intensity; (b) exposure time

To determine the conversion at the end of curing according to thickness, the only thing left needed is the proportionality constant. We will assume that the proportionality constant is independent from the intensity and exposure time. However, there seems to be an issue with the data presented in the paper [24] because we do not get a constant when the formula is applied to get the curves as shown in Figure 14.1. Taking the average slope for the data at 50 mW/cm² and $t = 100$ s gives a proportionality constant of $K = 0.207$.

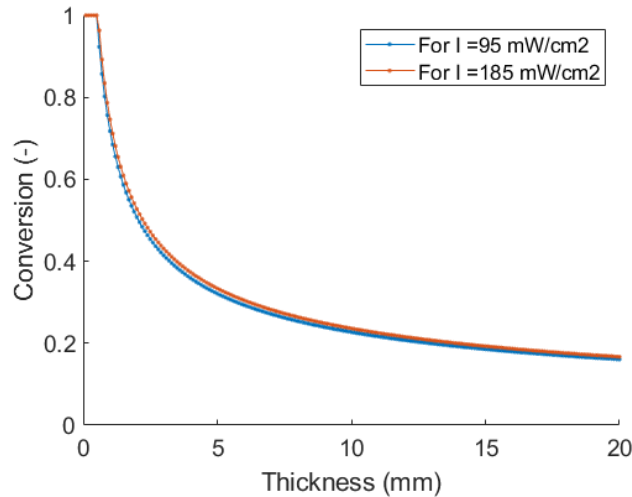


Figure 14.3: Conversion versus thickness for intensity 97 and 185 mW/cm^2

Finally, the thickness dependence of the conversion at 97 mW/cm^2 , 8 seconds and 185 mW/cm^2 , 6 seconds is shown in Figure 14.3 for the corresponding μ parameter

values, $\beta = 0.5$ and proportionality constant, $K = 0.207$. A conversion of 1 is observed for the thickness 1 mm which means the resin of 1 mm thickness is completely cured at the end of curing process.

From Figure 14.3, the conversion, α , of the specimen for case-C at the end of curing for thicknesses of 4, 5 and 6 mm are 0.36, 0.29 and 0.27 respectively. Even though μ is different for intensity 97 mW/cm^2 and 185 mW/cm^2 , the conversion at the end of curing are very close which clearly states that both cases have similar curing effect on conversion. This can be justified with the formula $I \times \sqrt{t}$.

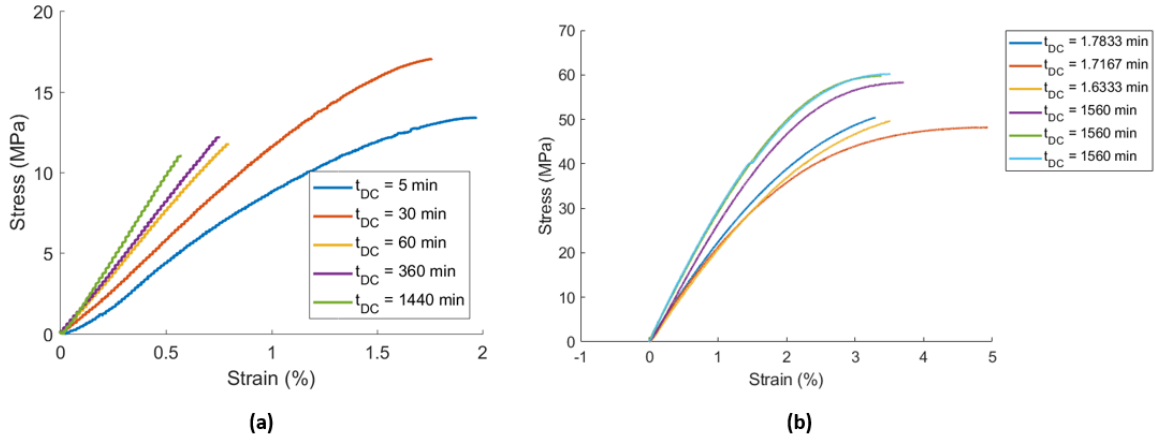


Figure 14.4: Stress versus strain for tensile tests at different dark cure times t_{DC} using (a) Rubber mold; (b) Teflon mold

Step-2: At Web Handling Research Center, Ron Markum and Xin Chen [96] measured the modulus of the resin for different dark cure times which can be used to estimate the increase in conversion during dark curing. Tensile test is performed on UV resin specimen which is cured at intensity 185 mW/cm^2 for 6 seconds using rubber mold and Teflon mold. Figure 14.4 shows the stress-strain plot for different dark cure times. The curing reaction rate is shown to depend on the mold material since different material behavior is observed for Teflon and rubber mold as shown in Figure 14.4. The slope of the curve is calculated to find the Young's modulus at that dark cure time and then is divided by the corresponding fully cured modulus to estimate the conversion. For the resin cured in rubber mold, the fully cured modulus value is

2068 MPa (given by Manufacturer), whereas for the resin cured in Teflon mold, the fully cured modulus is the modulus of the resin measured at 26 hours dark curing *i.e.* 2984 MPa.

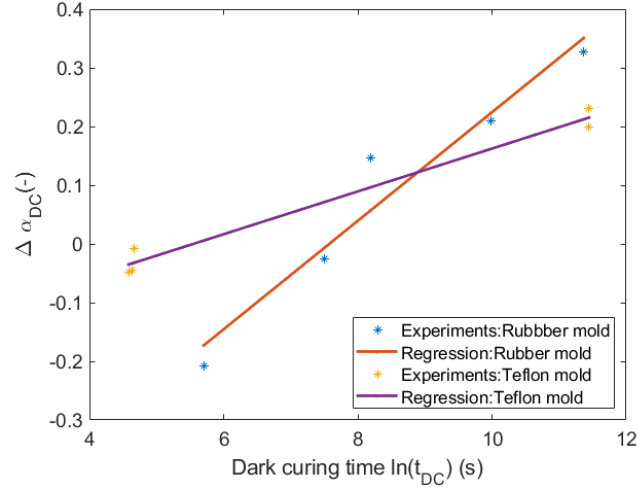


Figure 14.5: Dark curing conversion versus time

Here, $\Delta\alpha_{DC}$ is defined as difference between conversion during dark cure time and initial conversion *i.e.* $\alpha_{DC} - \alpha_i$. Obtaining α_i for the corresponding thicknesses from Figure 14.3 and α_{DC} from Figure 14.4, $\Delta\alpha_{DC}$ can be estimated for different dark cure times, t_{DC} . Arribas [99] found that the conversion reached ($\Delta\alpha_{DC}$) is proportional to $\ln(t_{DC})$. This relationship seems to be verified for our system as well and is plotted for both Teflon and Rubber mold as shown in Figure 14.5.

Step-3: Using the relation between $\Delta\alpha_{DC}$ and $\ln(t_{DC})$ for Teflon mold from Figure 14.5, conversion of specimen at the start of case-S test *i.e.* dark cure time of 60 seconds is estimated to be 0.6. Specimen used for case-C is cured in wax mold and its curing reaction rate is assumed to be similar to the rubber mold. Therefore, relation between $\Delta\alpha_{DC}$ and $\ln(t_{DC})$ for rubber mold is used to obtain t_{DC} for case-C specimen to reach the similar conversion rate as case-S as shown in Table 14.2.

Preliminary testing has indicated that the creep of the resin was higher at 6

Table 14.2: Dark cure time for the creep test (case-C) specimen

Specimen thickness, mm	$\Delta\alpha_{DC}(=0.6-\alpha_i)$	Dark cure time, t_{DC}
4	0.359	7 hours 27 min
5	0.3211	11 hours 13 min
6	0.2931	15 hours 11 min

hours dark curing, indicating a lower conversion degree than the stress relaxation test, and lower at 24 hours, indicating a higher conversion degree. As conversion increases in the resin, the cross linking density increases, leading to lower molecular mobility. Consequently, the elastic modulus increases and the creep compliance decreases, leading to a decrease of creep strain at a given stress level as dark curing increases. Following this reasoning, for the creep test properties to be equivalent to the stress relaxation test properties, we expect the creep specimen to have to be dark cured between 6 and 24 hours. Creep tests are performed for the validation.

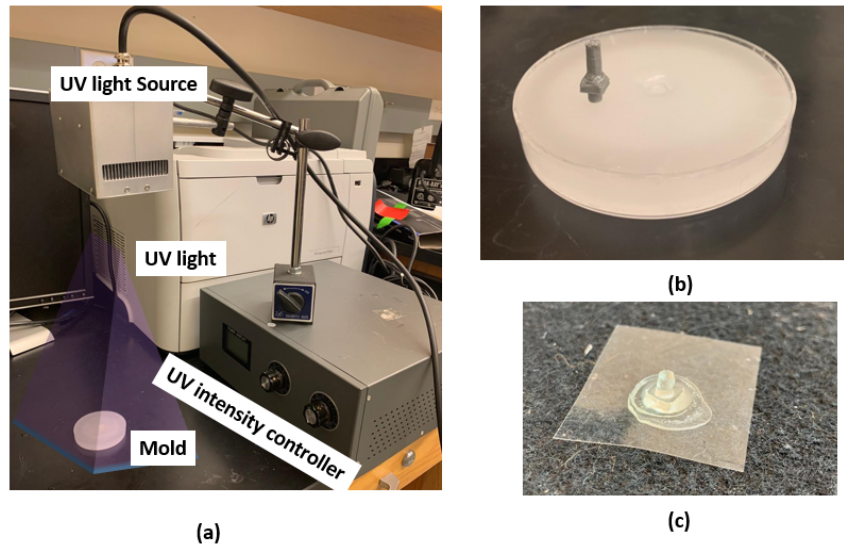


Figure 14.6: (a) UV light setup with mold on which UV light is exposed; (b) Geometry of the mold; (c) The specimen

14.2. 2 Validation test setup

Specimen Preparation: The wax material is chosen for the mold. A cylindrical shape of 3 mm diameter and 3 mm height with a square base of size 4 mm × 4 mm with 3 mm thickness is 3D printed which is pressed on the wax mold to form the shape of imprinted surface. Once the wax mold is prepared, UV-15 resin is poured in the mold using a pipette filler with rubber bulb and we make sure there is no air bubble. PET material is placed on top of the UV-15 resin. This setup is exposed to UV light at an intensity of 97 mW/cm^2 for 8 seconds as shown in Figure 14.6. This 8 seconds is referred to as curing time.

Once the specimen is cured, it is dark cured for certain period typically between 8 to 11 hours depending on its thickness before performing the test. Specimen is loaded to Instron tensile machine (Instron 5965) between the compression platens as shown in Figure 14.7 and is subjected to a constant pressure of 1 MPa for 16 hours. The deformation of resin through time is measured in the test and its strain is calculated by dividing the displacement with the thickness of specimen.



Figure 14.7: Setup of creep test on Instron tensile machine

Specimen of 5.24 mm, 4.85 mm, 6.22 mm thicknesses are subjected to the creep test with dark cure time of 9 hours (case-1), 10 hours 54 minutes (case-2), 24 hours (case-3) respectively and its strain through time is shown in Figure 14.8. With increased dark cure time, the creep strain and the rate of creep strain is shown to decrease. With the increase of dark cure time, the conversion degree during test is increased leading to lower creep strain. For the case-3 creep test, the creep strain increases from 0.01 to 0.018 over 16 hours which is very small compare to case-1 and case-2 creep tests indicating that the viscoelastic behavior in the resin saturates with increased dark curing time.

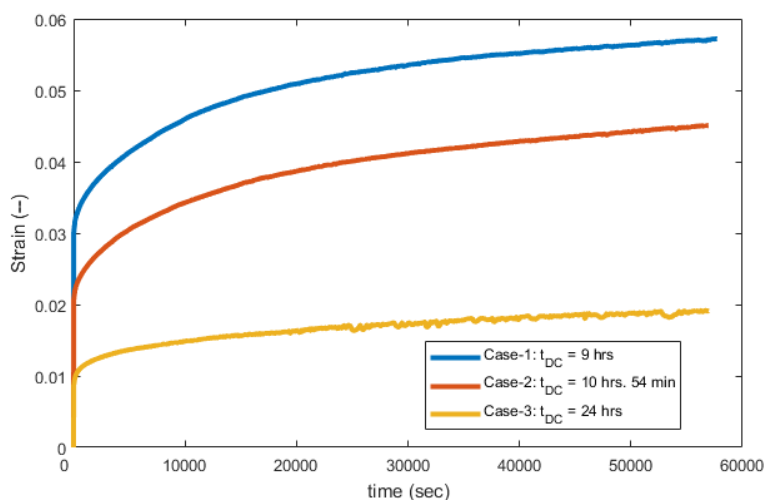


Figure 14.8: Strain of the resin through time for specimens with different dark cure times, t_{DC}

14.2. 3 Comparison with numerical model

A numerical creep model is setup in the ABAQUS as explained in the section 11.4 with imprinted surface in the scale of millimeters as shown in the Figure 14.9. UV15 Resin with viscoelastic properties as shown in Table 11.1 and the PET web with elastic properties as shown in Table 12.1 are introduced in the model. A constant uniaxial compressive load *i.e.* $P \times A$ is imposed on the top of model. Here, P is the

pressure applied in the creep test which is 1 MPa and A is the cross sectional area of resin that is in contact with the load which is $\pi \times \frac{D^2}{4}$. For resin with diameter of 3 mm, a compressive load of 7.068 N is applied on the model. The uniaxial strain $\varepsilon(t)$ of the resin is computed from time-dependent displacement using Equation (14.2). since the dimensions of the specimen are changing for every creep test, simulation are performed for the corresponding test specimen dimensions for comparison.

$$\varepsilon(t) = \frac{\text{displacement}}{L} \quad (14.2)$$

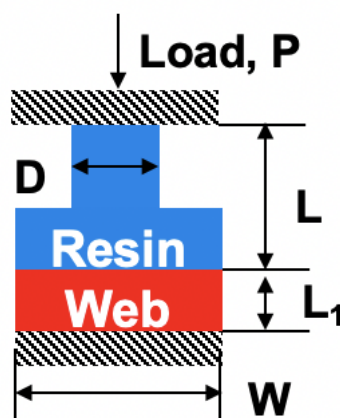


Figure 14.9: Geometry and boundary conditions of the numerical creep model

The creep test is performed on three imprinted specimens, case-i, case-ii and case-iii, with dimensions as shown in Table 14.3. A numerical model is built for each specimen geometry to compute the creep strain. The computed creep strain is compared with the creep test experimental data for validation as shown in Figure 14.10. The creep strain is matching well with the computed results for adjusted dark curing times.

The calculated dark cure time for the case-i specimen with 5.14 mm resin thickness is 11 hours 46 minutes from section 14.2. 1 as shown in Table 14.3. At the dark

Table 14.3: Cases considered for performing creep test for validation

Cases	L, mm	L_1 , mm	D, mm	W, mm	Estimated t_{DC}	t_{DC} at Exp. perf.
Case-i	5.14	0.1	2.3	4.81	11 hrs. 46 min.	9 hrs.
Case-ii	4.17	0.1	2.52	5	8 hrs. 4 min.	5 hrs. 18 min.
Case-iii	5.2	0.1	2.33	4.9	12	9 hrs. 14 min.

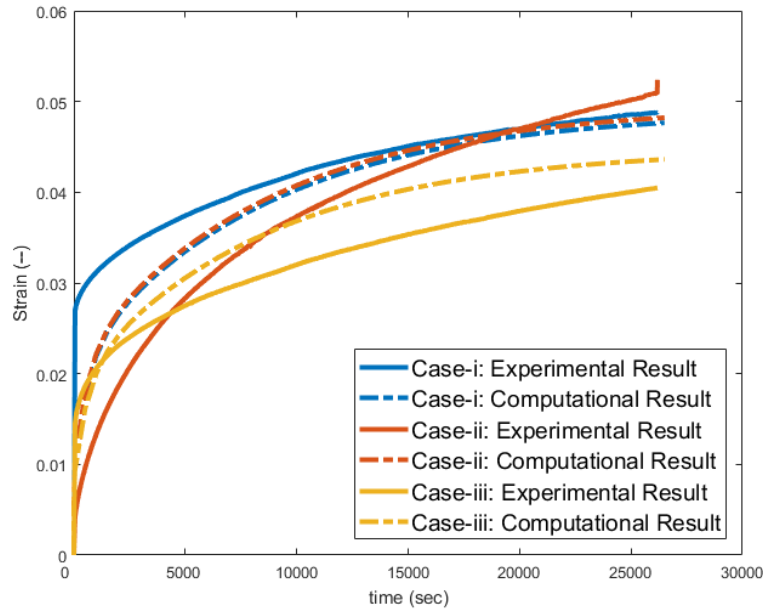


Figure 14.10: Comparison of creep test with computational model with strain of the resin through time

cure time of 11 hours 46 minutes, the resin is supposed to have a similar degree of conversion as that of case-S. However a closer degree of conversion is obtained earlier than the estimated dark cure time, *i.e.* at 9 hours as shown in Figure 14.10. The actual dark cure time is 2 hours 46 minutes shorter than the estimated value. Similar offset of the dark cure time for experimental results compared to estimated times are observed for case-ii & iii where the experiments are performed on the specimen with dark cure times 2 hours 46 minutes earlier than the estimated time. With this systematic offset, the computational model compares well with the experimental results and, hence, provides a good estimation of the behavior of the resin.

The method developed for estimating dark cure time relies on a number of as-

assumptions, such as extrapolating the parameters μ and β to the present curing conditions for estimating degree of conversion at the end of curing, assuming β is a constant, assuming the modulus given by the manufacturer for the resin corresponds to a maximal degree of conversion of 1 when cured in rubber mold, and defining the dark cure kinetics of the Teflon mold specimens with a limited number of data points. Considering the assumptions, the offset is understandable, and considering the fact that the offset seems to be constant, the model is valid but highly dependent on dark curing kinetics. The estimated dark cure time from section 14.2. 1 gives a window of possible values where the validation test can be performed.

In conclusion, a method that will allow the prediction of the impact of storing nano imprinted surface features in wound rolls is developed and is successfully validated by creep test.

CHAPTER XV

FINDINGS AND CONCLUSIONS FOR UV-NIL NANOIMPRINTS SUBJECTED TO WINDING

A method to quantify the creep deformation of the imprinted surfaces when subjected to wound roll pressures is developed. This will help establish how the imprinted materials should be wound and how long they can be subjected to pressure in the wound roll before they should be unwound to limit the deformation of the nano-imprinted features.

- The viscoelastic characterization of UV-15 resin during dark curing is performed and the Prony series representing its behavior is estimated using a Wiechert rheological model.
- The function coefficients i.e. K_1 and K_2 , of the radial modulus are estimated both numerically and analytically for the nano-imprinted web and used as input parameters to the winding model.
- Using the viscoelastic properties of the UV-15 resin, the equivalent radial viscoelastic properties of the nano-imprinted web are computed in Abaqus.
- Using the viscoelastic winding model, the radial pressures at different radial locations are computed through time.
- From the radial pressure profile of the wound roll, the viscoelastic effect of the imprint on the wound roll pressure was negligible, indicating the pressure is

constant through time. This occurred in this example because the thickness of the imprinted resin was small compared to the elastic support web thickness.

- In response to that radial pressure, the imprinted web exhibits a maximum deformation of 27 % when stored in the wound roll form for more than 11 hours. This deformation is assumed entirely located in the imprints that are softer than the web.
- The strain of the nanoimprints on the outer layer is 0 % as they are not submitted to any radial pressure.
- Deformations of 27 % would potentially affect the functionality of the imprinted surface.
- A validation test is successfully performed at the millimeter scale to compare the measured creep deformation of the imprinted surface to the numerical model.
- The influence of curing conditions, of specimen thickness, and of dark curing kinetics on the degree of conversion at the end of curing and dark curing is studied. This study estimated the dark curing time required for the validation creep test to attain similar curing conditions as that of the stress relaxation test used for UV15 resin viscoelastic characterization.

Conclusions

- This work develops a method leading to the direct prediction of strain according to storage time in wound rolls for nano-imprinted webs. The developed model is highly dependent on the curing kinetics of the resin, which need to be precisely characterized and introduced as model material parameters.
- The method can be applied to mitigate imprints deformation by decreasing the

winding tension, decreasing the storage time or by introducing intermediary process steps to relax the viscoelastic strain.

CHAPTER XVI

FUTURE WORK

16.1 Validation of the lamination model

This study revealed that the nip mechanics of the rubber-covered roller and the bending strains due to entry wrap angles of laminae, which induced shear and MD strain in the laminating webs, influenced the resulting curl. Considering all the parameters that affect the laminated web curl, a lamination model is developed, which replaced the trial and error procedure followed by operators at laminator machines in industries to produce a curl-free laminated web. The model was validated for a rigid adhesive by comparing to a closed form expression. For the case of a viscoelastic adhesive, additional model validation should be performed. Although the lamination model is developed for one set of web and adhesive materials, the developed technique can be adapted to other types of laminating and adhesive material and nip rollers. Future work should include a direct comparison of the curl predicted by the model and experimental results from an actual web lamination line modifying for the various process parameters, web, and adhesive materials.

16.2 Characterization of the viscoelastic UV-15 resin considering dark curing period

An experimental method is developed to characterize the viscoelastic properties of UV15 resin considering the dark cure period in the present study. Since the resin was cured in the Teflon mold, it attained a completely cured stage in a very short time leaving no room for studying its behavior during dark cure time. It may add value to the experimental method if the test is repeated on the resin with a slow curing reaction rate. The slow curing reaction rate can be achieved by curing in the rubber mold, as well as shortening the time between the end of curing and start of experiment by setting the test setup such that the specimen can be cured when loaded in the machine. The tests can also be performed on short periods with a wide range of frequencies, to build a master curve to fully characterize the material over long dark curing periods. This entails that a relationship including the influence of temperature on the dark curing kinetics is developed. Such results would allow to complete the initiated study on equivalent conversion degrees according to curing time, intensity, and dark curing by providing more detailed data on dark curing kinetics.

16.3 Validation of the wound nanoimprinted web model at the nanometer scale

Future studies should validate the numerical model at the nanometer scale, using the relevant experimental technique. Validating the developed numerical model at the nanometer scale may be possible with a testing apparatus that can perform in-situ tests and able to record creep deformation of the nano-size patterns when subjected to constant pressure. Microtomographs are capable of performing in-situ tests with a highest resolution of $0.5 \mu\text{m}$, which is much higher than the resolution required here.

Equipment that is capable of performing in-situ testing in the resolution of nanometers, such as atom probe tomography or scanning transmission electron microscopy (STEM) focal sectioning [100], could be one solution for performing validation test.

REFERENCES

- [1] J.K. Good and Z. Wu. The mechanism of nip-induced tension in wound rolls. *Journal of applied mechanics*, 60(4):942–947, 1993.
- [2] B.K Kandadai and J.K. Good. Finite element analysis of winding mechanics. *Proceedings of the Tenth International Conference on Web Handling, Oklahoma State University*, 2009.
- [3] N. Kanth, A.K. Ray, and R. Dang. Effect of design and process parameters on nip width of soft calendering. *International Journal for Computational Methods in Engineering Science and Mechanics*, 17(4):247–252, 2016.
- [4] T. Diehl, K.D. Stack, and R.C. Benson. A study of three-dimensional nonlinear nip mechanics. *Proceedings of the Second International Conference on Web Handling, Oklahoma State University*, 1993.
- [5] R.C. Batra. Quasistatic indentation of a rubber-covered roll by a rigid roll. *International Journal for Numerical Methods in Engineering*, 17(12):1823–1833, 1981.
- [6] M. Hannah. Contact stress and deformation in a thin elastic layer. *The Quarterly Journal of Mechanics and Applied Mathematics*, 4(1):94–105, 1951.
- [7] P.E. Austrell and A.K. Olsson. Two-dimensional elastic contact model for rubber covered rollers. *Plastics, Rubber and Composites*, 42(7):269–275, 2013.

- [8] H.T. Hahn and M. Levinson. Indentation of an elastic layer (s) bonded to a rigid cylinder—i. quasistatic case without friction. *International Journal of Mechanical Sciences*, 16(7):489–502, 1974.
- [9] T.C. Soong and C. Li. The steady rolling contact of two elastic layer bonded cylinders with a sheet in the nip. *International Journal of Mechanical Sciences*, 23(5):263–273, 1981.
- [10] K.D. Stack, J.E. Lafleche, and R.C. Benson. The effects of nip parameters on media transport. *Proceedings of the Third International Conference on Web Handling, Oklahoma State University*, 1995.
- [11] R.H. Bentall and K.L. Johnson. An elastic strip in plane rolling contact. *International Journal of Mechanical Sciences*, 10(8):637–663, 1968.
- [12] P. Werner. Machine direction curl control. *Proceedings of the Fifth International Conference on Web Handling, Oklahoma State University*, pages 279–296, 1999.
- [13] P.R. Pagilla, K.N. Reid, and J. Newton. Modeling of laminated webs. *Proceedings of the Ninth International Conference on Web Handling, Oklahoma State University*, pages 271–288, 2008.
- [14] S. Kidane. Laminate theory based 2D curl model. *Proceedings of the Tenth International Conference on Web Handling, Oklahoma State University*, pages 387–402, 2011.
- [15] R.P. Swanson. Web curl and web curl measurement. *Proceedings of the Fourteenth International Conference on Web Handling, Oklahoma State University*, 2017.
- [16] R.P. Swanson. Measurement of web curl. *Applied Web Handling Conference, Charlotte*, 2006.

- [17] S.Y. Chou, P.R. Krauss, and P.J. Renstrom. Imprint of sub-25 nm vias and trenches in polymers. *Applied physics letters*, 67(21):3114–3116, 1995.
- [18] J. Haisma, M. Verheijen, V.D.K. Heuvel, and V.D.J. Berg. Mold-assisted nanolithography: A process for reliable pattern replication. *Journal of Vacuum Science & Technology B: Microelectronics and Nanometer Structures Processing, Measurement, and Phenomena*, 14(6):4124–4128, 1996.
- [19] H. Tan, A. Gilbertson, and S.Y. Chou. Roller nanoimprint lithography. *Journal of Vacuum Science & Technology B: Microelectronics and Nanometer Structures Processing, Measurement, and Phenomena*, 16(6):3926–3928, 1998.
- [20] S. Ahn, J. Cha, H. Myung, S.M. Kim, and S. Kang. Continuous ultraviolet roll nanoimprinting process for replicating large-scale nano-and micropatterns. *Applied physics letters*, 89(21):213101, 2006.
- [21] S.H. Ahn and L.J. Guo. High-speed roll-to-roll nanoimprint lithography on flexible plastic substrates. *Advanced materials*, 20(11):2044–2049, 2008.
- [22] P. Maury, D. Turkenburg, N. Stroeks, P. Giesen, I. Barbu, E. Meinders, A.V. Bremen, N. Iosad, R.W. Vander, and H. Onvlee. Roll-to-roll UV imprint lithography for flexible electronics. *Microelectronic Engineering*, 88(8):2052–2055, 2011.
- [23] H. Tramposch. Relaxation of internal forces in a wound reel of magnetic tape. *ASME Journal of Applied Mechanics*, 4(32):865–873, 1965.
- [24] B. Golaz, V. Michaud, Y. Leterrier, and J.A.E. Månson. UV intensity, temperature and dark-curing effects in cationic photo-polymerization of a cycloaliphatic epoxy resin. *Polymer*, 53(10):2038–2048, 2012.
- [25] B. Pasquale. Lamination system application and design consideration. *AIMCAL Fall Technical Conference*, 2005.

- [26] H.L. Weiss. Coating and laminating machines. *Converting Technology Company*, 1977.
- [27] Laminating problems and solutions. *Technical bulletin by Mactac*, 2012.
- [28] J.D. Pfeiffer. Mechanics of a rolling nip on paper webs. *TAPPI Journal*, 51:77A–85A, 1968.
- [29] J.D. Pfeiffer. Nip forces and their effect on wound-in-tension. *TAPPI Journal*, 60:115–117, 1977.
- [30] J.K. Good, Z. Wu, and M.W.R. Fikes. The internal stresses in wound rolls with the presence of a nip roller. *Journal of Applied Mechanics*, 61(4):182–182, 1994.
- [31] J.K. Good and M.W.R Fikes. Stresses within rolls wound in the presence of a nip roller. *Proceedings of the First International Conference on Web Handling, Oklahoma State University*, 1991.
- [32] J.K. Good, J. Hartwig, and R. Markum. A comparison of center and surface winding using the wound-in-tension method. *Proceedings of the Fifth International Conference on Web Handling, Oklahoma State University*, 1999.
- [33] J.K. Good. Modelling of nip induced tension in wound rolls. *Proceedings of the Sixth International Conference on Web Handling, Oklahoma State University*, 2001.
- [34] B.K Kandadai and J.K. Good. Measurement of nip induced tension and contact stresses. *Proceedings of the Tenth International Conference on Web Handling, Oklahoma State University*, 2009.
- [35] K.L. Johnson. Contact Mechanics. Cambridge: University Press. 1989.
- [36] P. Meijers. The contact problem of a rigid cylinder on an elastic layer. *Applied Scientific Research*, 18(1):353–383, 1968.

- [37] N.V. Deshpande. Calculation of nip width, penetration and pressure for contact between cylinder with elastomeric covering. *TAPPI Journal*, 61:115–118, 1978.
- [38] V.A. Thomas and H.R. Hoersch. Stresses due to the pressure of one elastic solid upon another with special reference to railroad rails. *Technical Reports, University of Illinois, Engineering Experiment station*, page Bulletin No. 212, 1930.
- [39] G.J. Parish. Measurements of pressure distribution between metal and rubber covered rollers. *British Journal of Applied Physics*, 9(4):158, 1958.
- [40] G.J. Parish. Apparent slip between metal and rubber-covered pressure rollers. *British Journal of Applied Physics*, 9(11):428, 1958.
- [41] G.J. Parish. Calculation of the behaviour of rubber-covered pressure rollers. *British Journal of Applied Physics*, 12(7):333, 1961.
- [42] B. Grashof and A. Delgado. Analysis of influencing parameters in deformable roll coating of counter-rotating rolls. *Journal of Coatings Technology and Research*, 12(1):63–73, 2015.
- [43] B. Willinger and A. Delgado. Analytical prediction of roll coating with counter-rotating deformable rolls. *Journal of Coatings Technology and Research*, 11(1):31–37, 2014.
- [44] J. Sorvari and M. Parola. Feeding in rolling contact of layered printing cylinders. *International Journal of Mechanical Sciences*, 88:82–92, 2014.
- [45] R.D.W. Miller. Variations of line pressure and rolling speed with indentation of covered rollers. *British Journal of Applied Physics*, 15(11):1423, 1964.
- [46] P.E. Austrell. Analytical modelling of hysteresis heating in rolling contact of rubber covered rollers. *Plastics, Rubber and Composites*, 42(7):276–281, 2013.

- [47] P. Meijers. The contact problem of a rigid cylinder on an elastic layer. *Applied Scientific Research*, 18(1):353–383, 1968.
- [48] J.B. Alblas and M. Kuipers. On the two dimensional problem of a cylindrical stamp pressed into a thin elastic layer. *Acta Mechanica*, 9(3-4):292–311, 1970.
- [49] T.C. Soong and C. Li. On the unbonded contact between plates and layered cylinders. *Journal of Applied Mechanics*, 47(4):841–846, 1980.
- [50] T.C. Soong and C. Li. The rolling contact of two elastic-layer-covered cylinders driving a loaded sheet in the nip. *Journal of Applied Mechanics*, 48(4):889–894, 1981.
- [51] T. Diehl. Two and three dimensional analysis of nonlinear nip mechanics with hyperelastic formulations. *Ph. D. Thesis, University of Rochester*, 1995.
- [52] T. Diehl, K.D. Stack, and R.C. Benson. A study of three dimensional nonlinear nip mechanics. *Proceedings of the Second International Conference on Web Handling, Oklahoma State University*, 1993.
- [53] K.D. Stack, J.E. LaFleche, and R.C. Benson. The effects of nip parameters on media transport. *Proceedings of the Third International Conference on Web Handling, Oklahoma State University*, 1995.
- [54] S. Pan. The mechanics of winding laminate webs and the prediction of machine direction curl. *PhD Thesis, Oklahoma State University*, 2019.
- [55] ASTM F415-87 standard test method for curl in carbon paper. 2005.
- [56] ASTM F556-88 standard test method for curl of carbonless copy papers. 2001.
- [57] TAPPI Test Method T 520 cm-96, Curl of gummed flat paper.

- [58] ANSI/ISO 4330 (ANSI/NAPM IT9.10-1996) photographic film and paper-determination of curl. 1994.
- [59] ASTM D3813/D3813M-98 standard test method for curling and twisting on unwinding of pressure-sensitive tapes. 2003.
- [60] ASTM D4825-97 standard test method for measurement of curl in cut-sized office paper. 2002.
- [61] N. Kooy, K. Mohamed, L.T. Pin, and O.S. Guan. A review of roll-to-roll nanoimprint lithography. *Nanoscale Research Letters*, 9(1):320, June, 2014.
- [62] M. Colburn, S.C. Johnson, M.D. Stewart, S. Damle, T.C. Bailey, B. Choi, M. Wedlake, T.B. Michaelson, S.V. Sreenivasan, J.G. Ekerdt, and C.G. Willson. Step and flash imprint lithography: A new approach to high-resolution patterning. *Emerging Lithographic Technologies III*, 9(320):379–389, 1999.
- [63] S.Y. Chou, P.R. Krauss, and P.J. Renstrom. Sub-10 nm imprint lithography and applications. *Journal of Vacuum Science Technology B: Microelectronics and Nanometer Structures Processing, Measurement, and Phenomena*, 15(6):2897–2904, 1997.
- [64] S.Y. Chou, P.R. Krauss, and P.J. Renstrom. Imprint lithography with 25 nanometer resolution. *Science*, 272(5258):85–87, 1996.
- [65] M. Colburn, S.C. Johnson, M.D. Stewart, S. Damle, T.C. Bailey, B. Choi, M. Wedlake, T.B. Michaelson, S.V. Sreenivasan, and J.G. Ekerdt. Step and flash imprint lithography: A new approach to high-resolution patterning. In *Emerging Lithographic Technologies III*, volume 3676, pages 379–389. International Society for Optics and Photonics, 1999.

- [66] U. Plachetka, M. Bender, A. Fuchs, B. Vratzov, T. Glinsner, F. Lindner, and H. Kurz. Wafer scale patterning by soft UV-nanoimprint lithography. *Microelectronic Engineering*, 73:167–171, 2004.
- [67] M. Vogler, S. Wiedenberger, M. Mühlberger, I. Bergmair, T. Glinsner, H. Schmidt, E.B. Kley, and G. Grützner. Development of a novel, low-viscosity UV-curable polymer system for UV-nanoimprint lithography. *Microelectronic engineering*, 84(5-8):984–988, 2007.
- [68] J. Lee, S.Y. Park, K.B. Choi, and G.H. Kim. Nano-scale patterning using the roll typed uv-nanoimprint lithography tool. *Microelectronic Engineering*, 85(5-6):861–865, 2008.
- [69] K. Mohamed. Three-dimensional patterning using ultraviolet curable nanoimprint lithography. In *PhD Thesis, University of Canterbury, Electrical and Computer Engineering*, October, 2009.
- [70] L.J. Guo. Recent progress in nanoimprint technology and its applications. *Journal of Physics D: Applied Physics*, 37(11):R123, 2004.
- [71] X. Cheng, L.J. Guo, and P.F. Fu. Room-temperature, low-pressure nanoimprinting based on cationic photopolymerization of novel epoxysilicone monomers. *Advanced Materials*, 17(11):1419–1424, 2005.
- [72] C. Perret, C. Gourgon, F. Lazzarino, J. Tallal, S. Landis, and R. Pelzer. Characterization of 8-in. wafers printed by nanoimprint lithography. *Microelectronic Engineering*, 73:172–177, 2004.
- [73] P. Yi, H. Wu, C. Zhang, L. Peng, and X. Lai. Roll-to-roll UV imprinting lithography for micro/nanostructures. *Journal of Vacuum Science & Technology B, Nanotechnology and Microelectronics: Materials, Processing, Measurement, and Phenomena*, 33(6):060801, 2015.

- [74] D.J. Resnick, W.J. Dauksher, D. Mancini, K.J. Nordquist, T.C. Bailey, S. Johnson, N. Stacey, J.G. Ekerdt, C.G. Willson, and S.V. Sreenivasan. Imprint lithography for integrated circuit fabrication. *Journal of Vacuum Science & Technology B: Microelectronics and Nanometer Structures Processing, Measurement, and Phenomena*, 21(6):2624–2631, 2003.
- [75] H. Yoshikawa, J. Taniguchi, G. Tazaki, and T. Zento. Fabrication of high-aspect-ratio pattern via high throughput roll-to-roll ultraviolet nanoimprint lithography. *Microelectronic Engineering*, 112:273–277, 2013.
- [76] Y. Ren and J.K. Good. The nip mechanics of nano-impression lithography in roll-to-roll process machines. *Proceedings of the Fourteenth International Conference on Web Handling, Oklahoma State University*, 2017.
- [77] R.P. Gutterman. Theoretical and practical studies of magnetic tape winding tensions and of environmental roll stability. *U.S. Contract No. DA-18-119-SC-42*, 1959.
- [78] M.G. Catlow and G.W. Walls. A study of stress distribution in pirns. *Journal of textile Institute*, 3:410–429, 1962.
- [79] W.G. Harland. Stress distribution and winding faults in reels of plastic film. *Polymer Engineering & Science*, 7(1):58–62, 1967.
- [80] W.G. Harland. Theoretical aspects of winding reels. *Plastic & Polymers*, 42(160):162–165, 1974.
- [81] P.J. Zsombor-Murray. Tangential and radial stress in a roll of wound paper. *Technical Notes, McGill University*, 4:65, June 28, 1965.
- [82] Y. Hari. Tension pattern for film winding. *Unpublished Report of the Department of Mechanical Engineering of the University of North Carolina at Charlotte.*, January 1, 1967.

- [83] J.D. Pfeiffer. Internal pressure in a wound roll of paper. *TAPPI Journal*, 49(8):342–347, August 1966.
- [84] J.D. Pfeiffer. Measurement of K2 factor for paper. *TAPPI Journal*, 64(4):105–106, April 1981.
- [85] Z. Hakiel. Nonlinear model for wound roll stresses. *TAPPI Finishing and Converting Conference*, 1986.
- [86] Z. Hakiel. Nonlinear model for wound roll stresses. *TAPPI Journal*, 70(5):113–117, 1987.
- [87] B.K. Kandadai and J.K. Good. Winding virtual rolls. *TAPPI Journal*, 10:25–31, June 2011.
- [88] Y. Ren, B.K. Kandadai, and J.K. Good. Center winding versus surface winding: The effect of winder type and web material properties on wound roll stresses. *Transactions of the Fifteenth Fundamental Research Symposium, Cambridge, England*, pages 25–31, September, 2013.
- [89] J.K. Good and J.D. Pfeiffer. Tension losses during centerwinding. *Proceedings of the TAPPI Finishing and Converting Conference*, pages 297–306, 1992.
- [90] C. Mollamahmutoglu and J.K. Good. Large deformation winding models. *Proceedings of the Tenth International Web Handling Conference*, pages 55–80, 2009.
- [91] J.K. Good and D. Roisum. Winding: Machines, Mechanics and Measurement. *TAPPI Press*, 2008.
- [92] W.R. Qualls and J.K. Good. An orthotropic viscoelastic winding model including a nonlinear radial stiffness. *Journal of Applied Mechanics*, 64(1):201–208, 1997.

- [93] W.R. Qualls and J.K. Good. Thermal analysis of a round roll. *Journal of Applied Mechanics*, 64(4):871–876, 1997.
- [94] H. Tramposch. Anisotropic relaxation of internal forces in a wound reel of magnetic tape. *ASME Journal of Applied Mechanics*, 34(4):888–894, 1967.
- [95] J.Y. Lin and R.A. Westmann. Viscoelastic winding mechanics. *ASME Journal of Applied Mechanics*, 12(56):821–827, 1989.
- [96] X. Chen. Simulations of nip contact mechanics and extraction of nano-imprints from molds in UV-NIL R2R processes. *PhD Dissertation, Oklahoma State University*, December, 2020.
- [97] G. Odian. *Principles of polymerization*. John Wiley & Sons, 2004.
- [98] R. Suzuki, N. Sakai, A. Sekiguchi, Y. Matsumoto, R. Tanaka, and Y. Hirai. Evaluation of curing characteristics in UV-NIL resist. *Journal of Photopolymer Science and Technology*, 23(1):51–54, 2010.
- [99] C. Arribas, A. González-González, M.G. Prolongo, and S.G. Prolongo. Influence of temperature and bn nanoparticles on UV, thermal and dark curing of a cycloaliphatic epoxy resin. *Journal of Thermal Analysis and Calorimetry*, 142:617–627, 2020.
- [100] G. Möbus and B.J. Inkson. Nanoscale tomography in materials science. *Materials Today*, 10(12):18–25, 2007.

APPENDICES

CALCULATION OF MD CURL RADIUS

The MD curl radius is calculated by using equation of circle (Equation (1.1)). From Figure A.1, circle of radius R with center (h, K) passes through three points (X_1, Y_1) , (X_2, Y_2) and (X_3, Y_3) . The equation for the circle for these three points can be written as shown in Equation (1.2). The set of equations are solved to find (h, K) and R . Here, R is the MD curl radius. In the FE simulation, all the node points of the laminated web which is considered for MD curl radius calculation are taken. Using MATLAB code as shown below, radius, R for every three consecutive node point in the laminated web is calculated. The average value is considered as final radius which is also known MD curl radius.

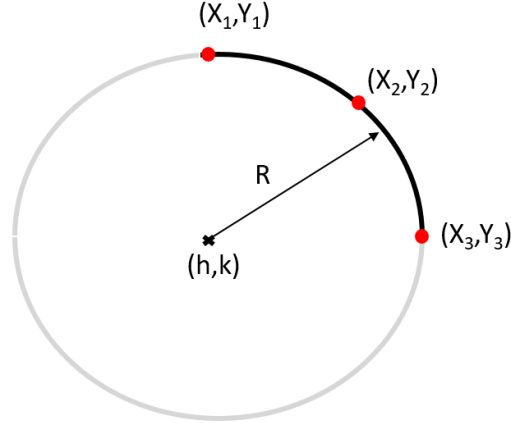


Figure A.1: Circle with three points

$$(X - h)^2 + (Y - k)^2 = R^2 \quad (\text{A.1})$$

$$(X_1 - h)^2 + (Y_1 - k)^2 = R^2$$

$$(X_2 - h)^2 + (Y_2 - k)^2 = R^2$$

$$(X_3 - h)^2 + (Y_3 - k)^2 = R^2 \quad (\text{A.2})$$

MATLAB CODE:

```
1 clc
2 close all
3 data = xlsread('File Location of X and Y coordinates of all node ...
    points');
4 x = data(:,1);
5 y = data(:,2);
6 syms h k r
7 harray = zeros(1); % X-coordinate of Center
8 karray = zeros(1); % Y-coordinate of Center
9 rarray = zeros(1); % Radius of Circle
10 j=1;
11 for i = 1:2:length(x)-2
12     eqns = [(x(i)-h)^2+(y(i)-k)^2-r^2 == 0,
13            (x(i+1)-h)^2+(y(i+1)-k)^2-r^2 == 0,
14            (x(i+2)-h)^2+(y(i+2)-k)^2-r^2 == 0];
15     S = solve(eqns, [h k r]);
16     Center_X = double(S.h);
17     Center_Y = double(S.k);
18     Center_R = double(S.r);
19     harray(j)=Center_X(2,1);
20     karray(j)=Center_Y(2,1);
21     rarray(j)=Center_R(2,1);
22     j=j+1;
23 end
24 avg=0;
25 for i=1:length(rarray)
26     avg=avg+rarray(i);
27 end
28 disp(avg/length(rarray)); % MD Curl Radius
```

VITA

Manogna Jambhapuram

Candidate for the Degree of

Doctor of Philosophy

Dissertation: VISCOELASTIC PHENOMENA IN ROLL-TO-ROLL MANUFACTURING
- *TWO CASE STUDIES OF INDUSTRIAL RELEVANCE*

Major Field: Mechanical and Aerospace Engineering

Biographical:

Education:

Completed the requirements for the Doctor of Philosophy in Mechanical and Aerospace Engineering at Oklahoma State University, Stillwater, Oklahoma in December, 2020.

Completed the requirements for the Master of Design in Mechanical Systems at Indian Institute of Information Technology for Design & Manufacturing, Tamil Nadu, India in 2017.

Completed the requirements for the Bachelor of Technology in Mechanical Engineering at Jawaharlal Nehru Technological University, Andhra Pradesh, India in 2014.

Experience:

Employed by Oklahoma State University, School of Mechanical and Aerospace Engineering as a graduate research assistant from 2017 to 2020.